

**Dissertation**  
**submitted to the**  
**Combined Faculties for the Natural Sciences and for Mathematics**  
**of the Ruperto-Carola University of Heidelberg, Germany**  
**for the degree of**  
**Doctor of Natural Sciences**

**Put forward by**  
**Diplomphysiker Julian Skrotzki**  
**Born in Heidelberg**  
**Oral examination: 19 January 2012**



**High-accuracy multiphase humidity measurements using TDLAS:  
application to the investigation of ice growth in simulated cirrus clouds**

Referees: Prof. Dr. Volker Ebert  
Prof. Dr. Bernd Jähne



All the world's a stage,  
And all the men and women merely players

William Shakespeare  
*As You Like It*, Act II Scene VII

# Kurzzusammenfassung

Wasserdampf spielt für die Wolkenexperimente an der Aerosol- und Wolkenkammer AIDA (Aerosol-Interaktionen und Dynamik in der Atmosphäre) eine entscheidende Rolle. Zur genauen und empfindlichen Messung von Wasserdampf- und Gesamtwasserkonzentrationen sowie dem Flüssigwasser- bzw. Eiswassergehalt ist die AIDA-Kammer mit drei Tunable-diode-laser (TDL) Hygrometern ausgestattet. Die vorliegende Arbeit stellt instrumentelle Verbesserungen, neue Entwicklungen und eine Beurteilung der Leistungsmerkmale dieser Instrumente vor – mit besonderem Augenmerk auf der Messgenauigkeit.

Für die Echtzeit-Auswertung der Messdaten der AIDA-TDL-Hygrometer sind schnelle, genaue und stabile Methoden erforderlich. Eine solche Methode ist im Rahmen dieser Arbeit mit dem hochentwickelten integrativen Kurvenanpassungs-Algorithmus entstanden. Neben seinem Einsatz im Rahmen von AIDA-Messungen könnte dieser Algorithmus weitere Anwendung in atmosphärischen Spurengasmessungen, der Verbrennungsprozessanalyse sowie in eingebetteten Systemen mit begrenzter Rechenleistung finden.

Die Leistungsfähigkeit der TDL-Hygrometer kam in AIDA-Experimenten zur Anwendung, die das Eispartikel-Wachstum in Zirruswolken im Temperaturbereich zwischen 190 K und 235 K untersucht haben. Mit Hilfe dieser Experimente konnte der Akkommodationskoeffizient von Wassermolekülen auf wachsenden Zirrus-Eispartikeln,  $\alpha_{\text{Eis}}$ , bestimmt werden. Dieser Parameter ist für die Anfangsphase des Eiswachstums in Zirruswolken von großer Bedeutung. Das über den Temperaturbereich gemittelte experimentelle Ergebnis  $\alpha_{\text{Eis}} = 0.8^{+0.2}_{-0.5}$  lässt darauf schließen, dass das Wachstum von Zirrus-Eispartikeln nicht maßgeblich verlangsamt ist, wie es für ein niedriges  $\alpha_{\text{Eis}} < 0.1$  der Fall wäre. Daher sollte  $\alpha_{\text{Eis}}$  geringe Auswirkungen auf Zirruswolken und ihre Eigenschaften haben. Zukünftige Zirruswolken-Modellstudien können sich überdies auf einen gut eingeschränkten Wertebereich für  $\alpha_{\text{Eis}}$  stützen.

# Abstract

Water vapor is a crucial quantity in cloud studies at the aerosol and cloud chamber AIDA (Aerosol Interactions and Dynamics in the Atmosphere). The chamber is equipped with three tunable diode laser (TDL) hygrometers for the accurate and precise measurement of water vapor and total water concentration as well as liquid/ice water content down to the low ppb range. This thesis presents instrumental improvements, new developments, and assessment of the performance of these instruments – with special emphasis on measurement accuracy.

For online evaluation of the AIDA TDL hygrometers' measurement data, there is demand for a fast, accurate, and robust method which has been developed with the advanced integrative fitting algorithm. Besides utilization at AIDA, this algorithm could find further application in atmospheric trace gas measurements, combustion process analysis, or could be integrated into embedded systems with limited computing power.

The capabilities of the AIDA TDL hygrometers have been applied to AIDA experiments investigating ice particle growth within cirrus clouds in the temperature range between 190 K and 235 K. These experiments could constrain the accommodation coefficient of water molecules on growing cirrus ice particles,  $\alpha_{ice}$ , which is relevant for the initial stage of ice growth in cirrus clouds. The temperature averaged result  $\alpha_{ice} = 0.8_{-0.5}^{+0.2}$  suggests that cirrus ice particle growth is not significantly suppressed as it would be for a low  $\alpha_{ice} < 0.1$ . Therefore, implications of  $\alpha_{ice}$  for cirrus clouds and their characteristics should be minor and future cirrus cloud model studies can rely on a well constrained  $\alpha_{ice}$ .



# Contents

<b>1</b>	<b>Introduction .....</b>	<b>1</b>
<b>2</b>	<b>Molecular absorption spectroscopy .....</b>	<b>5</b>
2.1	Absorption spectra .....	5
2.1.1	Vibrational excitations.....	6
2.1.2	Rotational excitations .....	8
2.1.3	Rotational-vibrational spectrum of water vapor .....	9
2.2	Absorption line shapes .....	10
2.2.1	Natural line broadening .....	10
2.2.2	Doppler broadening .....	11
2.2.3	Collision broadening.....	11
2.2.4	Voigt profile .....	12
2.3	Direct tunable diode laser absorption spectroscopy.....	13
2.3.1	Diode lasers .....	14
2.3.2	Distributed feedback diode lasers .....	16
2.3.3	Application of the Beer–Lambert law .....	17
<b>3</b>	<b>Aerosol and cloud chamber AIDA .....</b>	<b>21</b>
3.1	Instrumentation .....	21
3.2	AIDA cloud expansion experiments.....	24
<b>4</b>	<b>Integrative fitting of absorption line profiles .....</b>	<b>27</b>
4.1	Principle of integrative evaluation.....	27
4.2	Development of the advanced integrative fitting algorithm.....	29
4.2.1	Functionality.....	29
4.2.2	Comparison with Levenberg–Marquardt fitting algorithm.....	35
4.2.3	Application to experimental data .....	38
4.2.4	Discussion of advantages and disadvantages .....	40
<b>5</b>	<b>Tunable diode laser hygrometers at AIDA.....</b>	<b>43</b>
5.1	Sources of measurement uncertainty .....	44
5.2	Improvements and new developments.....	48
5.2.1	Instrumental overview .....	48
5.2.2	Common instrumental setup and data evaluation .....	50
5.2.3	APicT: long path in situ hygrometer .....	51

5.2.4	SP-APicT: novel short path in situ hygrometer.....	54
5.2.5	APeT: extractive total water hygrometer .....	57
5.2.6	Characterization of residual laser water .....	60
5.3	Performance.....	63
5.3.1	Time resolution and response time .....	63
5.3.2	Signal stability and transmission losses .....	66
5.3.3	Sensitivity and dynamic range .....	69
5.3.4	Reproducibility and self-calibration.....	76
5.3.5	Accuracy and validation by different measurement techniques .....	77
<b>6</b>	<b>Accommodation coefficient of water molecules on growing cirrus ice particles.....</b>	<b>85</b>
6.1	Overview and role for modeling of cirrus clouds .....	86
6.2	Theory of atmospheric ice particle growth.....	89
6.2.1	Kinetic regime .....	90
6.2.2	Continuum regime .....	91
6.2.3	Transition regime.....	92
6.2.4	Latent heat of deposition .....	94
6.2.5	Non-spherical ice particles .....	94
6.3	Development of the ice growth model SIGMA .....	95
6.4	AIDA cirrus cloud experiments .....	97
6.4.1	Overview of experiments.....	98
6.4.2	Application of the ice growth model SIGMA .....	102
6.4.3	Monte Carlo uncertainty analysis .....	105
6.5	Results and discussion .....	106
<b>7</b>	<b>Summary .....</b>	<b>111</b>
<b>8</b>	<b>Outlook.....</b>	<b>115</b>
<b>A</b>	<b>Physical quantities used in SIGMA .....</b>	<b>117</b>
	<b>Bibliography .....</b>	<b>119</b>
	<b>List of principal symbols.....</b>	<b>131</b>
	<b>List of acronyms.....</b>	<b>135</b>
	<b>List of own publications.....</b>	<b>137</b>
	<b>Acknowledgments .....</b>	<b>139</b>

# Chapter 1

## Introduction

As the most important greenhouse gas, water vapor plays an unrivaled role in Earth's atmosphere and climate system. In the upper troposphere and in the stratosphere, water vapor concentration has direct impact on atmospheric radiative forcing and on the rate of global warming (Solomon et al., 2010). In the troposphere, water vapor governs the formation of clouds – from pure liquid droplet clouds via mixed-phase clouds to pure ice clouds (Pruppacher and Klett, 1997). Cirrus clouds, as pure ice clouds are also called, form at altitudes above  $\sim 8$  km and temperatures below the homogeneous freezing limit of supercooled water which is approximately at  $-38$  °C. Radiative forcing of these cirrus clouds can be positive, i.e. warming, or negative, i.e. cooling, depending on ice particle size, shape, and number concentration (Zhang et al., 1999). On a global scale, the magnitude of cirrus cloud radiative forcing has remained unclear up to now due mainly to insufficient global satellite data of cirrus ice particle properties and number concentrations (Waliser et al., 2009).

Ice particle size, shape, and number concentration in cirrus clouds are a direct consequence of ice particle growth rates (Lin et al., 2002). One of the main parameters governing growth of ice particles up to a few micrometers in size, i.e. in the initial stage of ice particle growth in cirrus clouds, is the accommodation coefficient of water molecules on ice,  $\alpha_{ice}$ , for brevity called the ice accommodation coefficient. However, the ice accommodation coefficient is so far badly constrained by experiment. This makes its impact on ice particle properties and number concentrations and therefore cirrus cloud radiative forcing uncertain to a high degree.

A unique facility to study processes in cirrus clouds such as aerosol-cloud interactions or ice particle growth is the aerosol and cloud chamber AIDA (Aerosol Interactions and Dynamics in the Atmosphere) at the Karlsruhe Institute of Technology. Its operation temperature range down to  $-90$  °C and its large volume of  $84$  m<sup>3</sup> are unrivaled features. Water vapor concentration is a crucial parameter in the cirrus cloud studies performed at AIDA which makes it mandatory that the dynamic evolution of water vapor concentration during AIDA experiments is measured both with high accuracy and precision.

Three common in situ measurement techniques exist for the retrieval of water vapor concentrations when atmospheric processes are concerned. One of them is tunable diode laser

absorption spectroscopy (TDLAS), which is used in two variations: direct TDLAS and wavelength modulating TDLAS in combination with second harmonic detection (May, 1998). In addition, chilled-mirror frost point hygrometers (Vömel et al., 2007) and Lyman  $\alpha$  fluorescence spectrometers (Zöger et al., 1999) are widely used. The latter two techniques are restricted to measurements representative of water vapor concentrations within a relatively small volume which makes them not an ideal choice for in situ measurements in a large cloud chamber like AIDA. Moreover, all of the mentioned techniques except direct TDLAS need calibration for accurate measurements, either frequently as for wavelength modulating TDLAS and Lyman  $\alpha$  fluorescence spectroscopy or occasionally as for measurements with frost point hygrometers. However, regular calibrations would not be feasible for in situ measurements in AIDA due to the large volume of the AIDA vessel. For these reasons, the in situ hygrometers at AIDA are based on direct TDLAS with an absorption path covering the entire diameter of AIDA. With these tunable diode laser (TDL) hygrometers, a water vapor measurement representative of the humidity conditions within AIDA can be combined with high accuracy, high sensitivity, and nearly immediate time response.

### **Objectives and outline**

Prior to this work, it was not possible to obtain ice and liquid water content within AIDA with high quality at a high time resolution – a prerequisite for the ice growth studies of cirrus cloud particles presented in this thesis. Further restrictions included that accurate in situ TDL water vapor measurements were limited to concentrations below 2000 ppmv corresponding to temperatures below  $-15$  °C. AIDA experiments at temperatures above  $-15$  °C and therefore higher water vapor concentrations are important for the investigation of ice nucleation ability of biogenic aerosol such as bacteria (Möhler et al., 2008). For reliable online AIDA TDL data evaluation, no accurate method was available that allowed monitoring of humidity conditions in AIDA in real time and that could handle the severe signal transmission variations present during cloud formation phases.

For the scope of this thesis, three main objectives have been defined to advance the AIDA humidity measurements and to apply these measurements to answer a pending scientific question:

1. Achieving accurate multiphase humidity measurements with the AIDA TDL hygrometers and extending the in situ measurement dynamic range to higher water vapor concentrations,
2. developing a fast, accurate, and robust data evaluation algorithm for reliable online evaluation of AIDA TDL hygrometer measurements,
3. applying measurements of the AIDA TDL hygrometers to experiments investigating ice particle growth in cirrus clouds, in order to determine the ice accommodation coefficient  $\alpha_{ice}$ .

Following these main objectives, the outline of this thesis is as follows. In Chapter 2, an introduction to the fundamental principles and methods of molecular absorption spectroscopy and, in particular, direct TDLAS is given. It is followed by an overview of capabilities, instrumentation, and experimental methods of the AIDA chamber in Chapter 3.

Chapter 4 treats in detail the development of the advanced integrative fitting algorithm for online evaluation of absorption line profiles which has been designed to match the criteria of high speed, accuracy, and robustness stated above. Its properties are compared to and its performance is validated by a Levenberg–Marquardt fitting algorithm optimized to the problem of absorption line profile fitting and used as standard data evaluation method for AIDA TDL data so far.

In Chapter 5, the accomplished improvements of the existing in situ TDL hygrometer APicT (AIDA PCI in cloud TDL) are discussed along with the development of its single-path version SP-APicT which extends APicT’s capabilities to a wider measurement dynamic range and to operation in warm, dense clouds. Accompanying the water vapor measurements of both in situ TDL hygrometers, the novel instrument APeT (AIDA PCI extractive TDL) measures total water content by extractive sampling from the AIDA chamber. The now possible parallel measurement of total water and water vapor content allows the deduction of liquid and ice water content respectively, with high accuracy and time resolution. For all AIDA TDL hygrometers, special emphasis has been put on the maximization of measurement accuracy. Accuracy is assessed along with other performance parameters as measurement sensitivity, precision, and dynamic range and validated by comparison with independent measurement techniques.

In Chapter 6, measurements of the AIDA TDL hygrometers are applied to experiments investigating the ice growth in cirrus clouds in the temperature range between 190 K and 235 K. The aim of these experiments is to put reasonable constraints on the ice accommodation coefficient  $\alpha_{ice}$  in cirrus clouds. Evaluation of the experimental data has led to the development of the ice growth model SIGMA (Simple Ice Growth Model for determining Alpha). Results for the retrieval of  $\alpha_{ice}$  are presented along with experimental and modeling methods.

The final Chapters 7 and 8 contain a summary of the main advances and results achieved in this thesis and give an outlook to future prospects regarding the capabilities of the AIDA TDL hygrometers and the further validation of their measurement accuracy.

### **Nota bene**

Frequent cross references between different chapters and sections are aimed to provide the reader with additional information and guidance. However, coherence and consistency will be maximized by continuous reading of the entire thesis.



## Chapter 2

# Molecular absorption spectroscopy

The purpose of molecular absorption spectroscopy is to retrieve properties of the examined absorber, e.g. its concentration as in the case of direct tunable diode laser absorption spectroscopy (TDLAS) which will be introduced in Section 2.3. Implementation of direct TDLAS into a set of dedicated hygrometers at the aerosol and cloud chamber AIDA will be described in Chapter 5 with experimental application of measurements of these hygrometers following in Chapter 6. Further details about AIDA can be found in Chapter 3.

The principle of molecular absorption spectroscopy is based on the process of photons and their energy being absorbed by molecules to excite higher energy levels of molecular states. The magnitude of possible excitations results in absorption spectra with many individual absorption lines (see Section 2.1). For sufficiently high absorber molecule concentrations, the absorption of single photons adds up to a macroscopic attenuation of the electromagnetic (EM) radiation field which can be detected experimentally. Effects which influence the shape of absorption lines (see Section 2.2) can play a significant role in these absorption spectroscopic measurements which will become apparent in Chapter 4.

This chapter about molecular absorption spectroscopy mainly follows the much more comprehensive and detailed treatment of the topic in (Milonni and Eberly, 2010). Further reading on molecular spectroscopy can be found in (Graybeal, 1988) and in particular on laser absorption spectroscopy in (Demtröder, 2008b, a) and (Ebert and Wolfrum, 2001).

## 2.1 Absorption spectra

Molecular absorption spectroscopy relies on the properties of absorption spectra or single absorption lines of the absorber under examination. Different absorption lines represent different transitions among the discrete energy eigenstates of the molecules. These energy eigenstates refer to electronic, vibrational, or rotational excitations with decreasing transition energies in this order. In the following, we will concentrate on absorption spectroscopy in the near infrared (NIR) spectral region at wavelengths between 780 nm and 3  $\mu\text{m}$ . Into this re-

gion typically fall combined rotational-vibrational excitations, e.g. of water vapor. Electronic excitations are of higher energies and typically fall into the ultraviolet region of the EM spectrum. They will therefore not be treated here.

### 2.1.1 Vibrational excitations

For a diatomic molecule, the interatomic binding force can be approximated by a harmonic potential

$$V(x) = \frac{1}{2}k(x - x_0)^2, \quad (2.1)$$

where  $k$  is the interatomic coupling constant,  $x$  the interatomic distance, and  $x_0$  the distance for which the interatomic force

$$F(x) = -\frac{dV}{dx} = -k(x - x_0) \quad (2.2)$$

vanishes. If the separation  $x$  is greater than  $x_0$ , the binding force  $F$  is attractive whereas for  $x$  being less than  $x_0$ , the force is repulsive which results in a periodic vibrational motion of both atoms of the molecule. Treating this problem quantum mechanically, i.e. solving the stationary Schrödinger equation for the potential  $V$ , yields the following allowed vibrational energy levels

$$E_v = \hbar\omega \left( v + \frac{1}{2} \right), \quad v = 0, 1, 2, \dots \quad (2.3)$$

with  $\hbar$  being Planck's constant  $h$  divided by  $2\pi$  and

$$\omega = \sqrt{\frac{k}{m}}, \quad (2.4)$$

where  $m$  denotes the mass of the atoms.  $v$  is the vibrational quantum number and denotes the state of vibrational excitation. Excitations from the ground state  $v = 0$  to  $v = 1$  are called fundamental, whereas transitions  $v = 0 \rightarrow v \geq 2$  are called overtones. Note that the energy levels  $E_v$  are evenly spaced which makes all overtone transitions integer multiples of the fundamental transition in terms of transition energy.

For real diatomic molecular vibration, the harmonic potential (2.1) has to be extended by anharmonic terms

$$V(x) = \frac{1}{2}k(x - x_0)^2 + A(x - x_0)^3 + B(x - x_0)^4 + \dots \quad (2.5)$$

with additional anharmonic coupling constants  $A$  and  $B$ . The vibrational energy levels (2.3) then take the form

$$E_v = hc\omega_e \left[ \left( v + \frac{1}{2} \right) - x_e \left( v + \frac{1}{2} \right)^2 + y_e \left( v + \frac{1}{2} \right)^3 + \dots \right], \quad (2.6)$$

where  $\omega_e = \omega/(2\pi c)$  is for historical reasons given in units of wave numbers ( $\text{cm}^{-1}$ ) and  $c$  is the speed of light in vacuum. The anharmonicity coefficients  $x_e$  and  $y_e$  are dimensionless and independent of  $v$ . Numeric values for  $\omega_e$ ,  $x_e$ , and  $y_e$  are given in spectroscopic literature. For small values of  $v$ , deviations between (2.6) and the harmonic case (2.3) are typically small and (2.3) can be taken as very good approximation for the vibrational energy levels.

So far, we have treated only simple diatomic molecules. For polyatomic molecules, one obtains additional degrees of freedom of vibration. Linear polyatomic molecules with  $N$  atoms have  $3N - 5$  vibrational degrees of freedom, whereas for non-linear polyatomic atoms, there are  $3N - 6$  vibrational degrees of freedom<sup>1</sup>. For the three-atomic non-linear water molecule, one obtains three vibrational degrees of freedom and therefore three vibrational quantum numbers associated with the normal modes of vibration. These normal modes are called the symmetric stretch, bending, and asymmetric stretch mode and are depicted in Figure 2.1. Note that the energy levels and therefore the fundamental and overtone transitions of the symmetric and asymmetric stretch modes are almost degenerate. This results in absorption bands of the rotational-vibrational spectrum of water vapor which are a superposition of several individual vibrational transitions as we will see in Section 2.1.3.

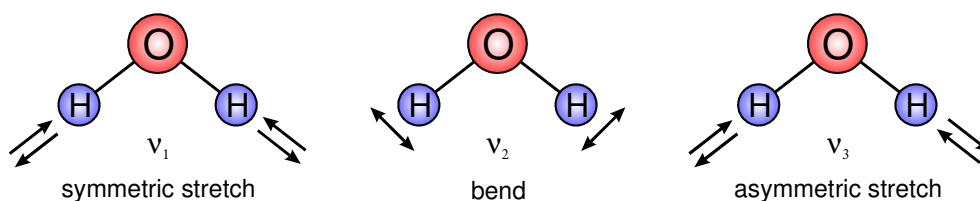


**Figure 2.1** Vibrational normal modes of the water molecule and their fundamental transition energies:  $\nu_1 = 3657 \text{ cm}^{-1}$ ,  $\nu_2 = 1595 \text{ cm}^{-1}$ , and  $\nu_3 = 3756 \text{ cm}^{-1}$  (Kjaergaard, 1994) with  $\nu_j = (E_{v_j=1} - E_{v_j=0})/(hc)$ .

<sup>1</sup>  $3N$  coordinates are necessary to describe the positions of all  $N$  atoms in a polyatomic molecule. The description of center of mass translation requires three coordinates and rotations require two additional coordinates for linear polyatomic molecules as well as three additional coordinates for non-linear polyatomic molecules. This leaves  $3N - 5$  and  $3N - 6$  coordinates for vibrations of linear and non-linear polyatomic molecules, respectively, which corresponds to their vibrational degrees of freedom.

### 2.1.2 Rotational excitations

A quantum mechanical treatment of a rigid diatomic molecule yields the following energy eigenvalues for its rotational excitations

$$E_J = \frac{\hbar^2}{2I} J(J+1), \quad J = 0, 1, 2, \dots \quad (2.7)$$

where  $I$  is the moment of inertia of the molecule and  $J$  the rotational quantum number defining the state of rotational excitation. Real diatomic molecules, however, are not rigid, but with increasing rotation, the centrifugal force tends to enhance the separation between the two atoms and therefore the moment of inertia  $I$ . For this reason, rotational energy is decreased with increasing rotational excitation, i.e. higher values of  $J$ . This can be accounted for by extending (2.7) to

$$E_J = hcBJ(J+1) - hcDJ^2(J+1)^2, \quad (2.8)$$

where the quantities  $B$  and  $D$  are independent of  $J$  and have units of wave numbers.

Vibration of a molecule besides rotation also increases its effective moment of inertia, the more the higher the vibrational quantum number  $\nu$ . This is accounted for by writing

$$B = B_e - \alpha_e \left( \nu + \frac{1}{2} \right), \quad (2.9)$$

where  $B_e$  and  $\alpha_e$  are independent of  $\nu$  and  $J$ . Inserting (2.9) into (2.8) yields for the rotational energy levels

$$E_J(\nu) = hc \left[ B_e - \alpha_e \left( \nu + \frac{1}{2} \right) \right] J(J+1) - hcDJ^2(J+1)^2. \quad (2.10)$$

Constants  $B_e$ ,  $\alpha_e$ , and  $D$  are tabulated for a large variety of molecules in spectroscopic literature.

The absorption spectrum for rotational excitations is defined by the allowed transitions  $\Delta J = \pm 1$ . For more complex non-linear polyatomic molecules like the water molecule, the moments of inertia are different for all three possible axes of rotation and one obtains two additional rotational quantum numbers besides  $J$ . The resulting combined spectra of rotational and vibrational excitations are therefore complex as we will see in the following section.

### 2.1.3 Rotational-vibrational spectrum of water vapor

As specific example for a molecular absorption spectrum including vibrational as well as rotational excitations, the rotational-vibrational spectrum of water vapor in the NIR spectral region is given. It is depicted in Figure 2.2. Each individual absorption line stands for a specific transition among the molecular vibrational and rotational states. Absorption bands form around different vibrational transitions with the rotational transitions determining the small differences in energy or wavelength, respectively, among the individual absorption lines.

In order to differentiate among distinct absorption lines, the following nomenclature is common. An absorption line is denoted by the quantum numbers of the vibrational and rotational states involved in the transition:  $\nu_1\nu_2\nu_3-\nu'_1\nu'_2\nu'_3$ ,  $J_1J_2J_3-J'_1J'_2J'_3$ . The unprimed quantum numbers refer to the initial states, whereas the primed quantum numbers refer to the final states of the transition.

From the fundamental vibrational transition energies of the water molecule,  $\nu_1 = 3657 \text{ cm}^{-1}$ ,  $\nu_2 = 1595 \text{ cm}^{-1}$ , and  $\nu_3 = 3756 \text{ cm}^{-1}$  (Kjaergaard, 1994), one obtains fundamental  $\nu_1$  and  $\nu_3$  absorption bands around  $2.7 \mu\text{m}$  wavelength as well as superimposed overtone and combined transition bands around  $1.9 \mu\text{m}$ ,  $1.4 \mu\text{m}$  and so on. This is a consequence of the nearly degenerate symmetric and asymmetric stretch mode of water vapor which results in almost identical fundamental transition energies  $\nu_1$  and  $\nu_3$ .

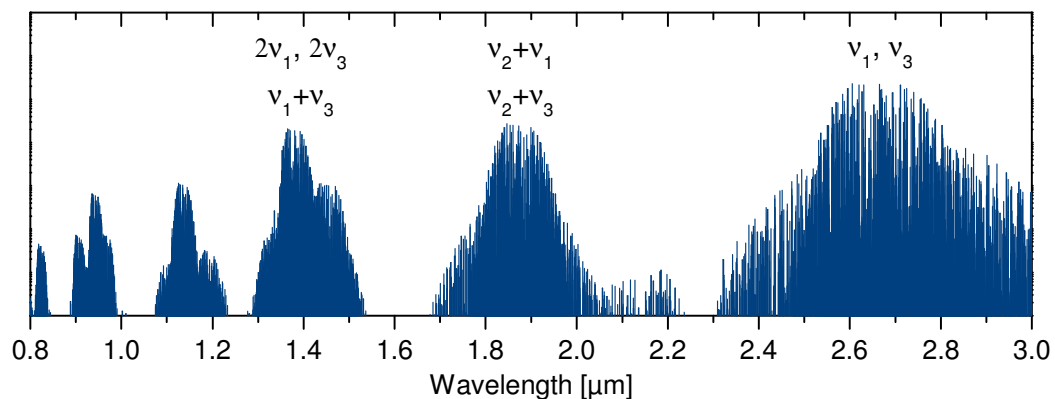


**Figure 2.2** Rotational-vibrational spectrum of water vapor in the near infrared spectral region. Different absorption bands refer to different fundamental, overtone, or combined vibrational transitions (cf. Figure 2.1) as indicated. Spectral data are based on HITRAN 2004 (Rothman et al., 2005).

## 2.2 Absorption line shapes

In the majority of measurement techniques relying on the evaluation of single absorption lines by direct spectroscopy, exact knowledge about the shape of the examined absorption lines is necessary. One example for such a technique is direct TDLAS which will be introduced in the following section. The discussion in this section will also be of relevance for the method of integrative evaluation of absorption line profiles presented in Chapter 4.

In principle, a transition between two molecular states has a sharply defined transition energy which would result in a delta peak shape of the associated absorption line. In reality however, different broadening mechanisms result in an absorption line shape called the Voigt profile. These broadening mechanisms as well as the Voigt profile will be discussed in the following.

### 2.2.1 Natural line broadening

An excited molecular state has a finite lifetime until it decays under spontaneous emission of a photon. The lifetime of the state is not sharply defined, but follows a probability distribution of exponential decay. This leads to a ‘smearing’ of photon energy  $E_\nu$  or equivalently wave number  $\nu$  defined by

$$\nu = \frac{1}{\lambda} = \frac{E_\nu}{hc}, \quad (2.11)$$

where  $\lambda$  denotes the wavelength of the photon or its associated EM radiation field, respectively, in vacuum.  $\nu$  is typically expressed in units of  $\text{cm}^{-1}$ . The smearing in photon energy results in a broadening of the absorption line representing the transition from the excited to a lower molecular state which is called natural line broadening.

The exact shape of the absorption line in wave number domain is given by the Fourier transformation of the exponential decay function of the excited molecular state. This Fourier transformation is represented by a Lorentzian function normalized to unit area

$$\Phi_N(\nu - \nu_0) = \frac{1}{\gamma_N \pi} \frac{\gamma_N^2}{(\nu - \nu_0)^2 + \gamma_N^2}, \quad (2.12)$$

where  $\gamma_N$  denotes the half width at half maximum (HWHM) and  $\nu_0$  the spectral position of the absorption line.

Under typical experimental conditions, the natural line width  $\gamma_N$  is negligible in spectroscopic measurements. At standard pressure and temperature, for example,  $\gamma_N$  is more than nine orders of magnitude smaller than the line widths induced by the broadening mechanisms discussed in the following.

### 2.2.2 Doppler broadening

If a molecule has a velocity component in the direction of propagation of a photon and this photon is then absorbed by the molecule, the photon's energy will slightly be shifted in the absorption process due to the Doppler effect. The shift in photon energy can be positive or negative depending on the direction of the molecular velocity vector and results in Doppler broadening of absorption lines.

The thermal velocity of molecules is given by the Maxwell–Boltzmann distribution which depends on absolute temperature  $T$  and molar mass  $M$  of the absorber. From the Maxwell–Boltzmann distribution, it follows that the absorption line shape function which describes the effect of Doppler broadening is a Gaussian function

$$\Phi_D(\nu - \nu_0) = \frac{1}{\gamma_D} \left( \frac{\ln 2}{\pi} \right)^{1/2} \exp \left[ - \ln 2 \left( \frac{\nu - \nu_0}{\gamma_D} \right)^2 \right] \quad (2.13)$$

with Doppler line width (HWHM)

$$\gamma_D = \frac{\nu_0}{c} \left( \frac{2 \ln(2) RT}{M} \right)^{1/2}, \quad (2.14)$$

where  $R$  is the universal gas constant.

### 2.2.3 Collision broadening

When a molecule in an excited state collides with another molecule this can lead to reduction of the lifetime of the excited state and consequently an increased absorption line width. This broadening process is called collision broadening and as molecular collision rate is proportional to gas pressure it is also known as pressure broadening. For gas pressures  $p \gtrsim 200$  hPa, it typically is the dominant source of line broadening.

As the principle of collision broadening is similar to that of natural line broadening, absorption line shape is given by a Lorentzian function

$$\Phi_C(\nu - \nu_0) = \frac{1}{\gamma_C \pi} \frac{\gamma_C^2}{(\nu - \nu_0)^2 + \gamma_C^2}. \quad (2.15)$$

The line width (HWHM)  $\gamma_C$  depends on absorber partial pressure  $p_{\text{abs}}$ , total gas pressure  $p$ , and absolute temperature  $T$

$$\gamma_C = [\gamma_{C,\text{self}} \cdot p_{\text{abs}} + \gamma_{C,\text{for}}(p - p_{\text{abs}})] \left(\frac{T_0}{T}\right)^{n_c}, \quad (2.16)$$

where  $\gamma_{C,\text{self}}$  is the self broadening coefficient,  $\gamma_{C,\text{for}}$  the foreign broadening coefficient, and  $n_c$  the temperature coefficient of collision broadening. Foreign broadening is typically a result of the absorber being mixed with air, i.e.  $\gamma_{C,\text{for}} = \gamma_{C,\text{air}}$ . For trace gases as absorber, the contribution of self broadening is typically negligible. Values for  $\gamma_{C,\text{air}}$ ,  $\gamma_{C,\text{self}}$ , and  $n_c$  for individual absorption lines can be found in spectroscopic data bases such as HITRAN (high resolution transmission, Rothman et al., 2009).

## 2.2.4 Voigt profile

For gas pressures near atmospheric pressure, neither  $\Phi_D(\nu - \nu_0)$  in (2.13) nor  $\Phi_C(\nu - \nu_0)$  in (2.15) accurately represent absorption line profiles as neither collision nor Doppler broadening is negligible. Therefore, Doppler and collision broadening have to be combined which is achieved in the normalized Voigt absorption line profile  $\Phi_V$  (Armstrong, 1967). It is given by the convolution of  $\Phi_D$  and  $\Phi_C$

$$\Phi_V(\nu - \nu_0) = \int_{-\infty}^{+\infty} \Phi_D(\nu') \Phi_C(\nu - \nu_0 - \nu') d\nu'. \quad (2.17)$$

A comparison of  $\Phi_V$ ,  $\Phi_D$ , and  $\Phi_C$  is given in Figure 2.3 for  $\gamma_D \approx \gamma_C$ .

Unfortunately, (2.17) cannot be solved analytically. However, there exist analytical approximations, e.g. by (Whiting, 1968)

$$\begin{aligned} \frac{\Phi_V}{l_{\Phi_V}} = & \left(1 - \frac{\gamma_C}{\gamma_V}\right) \exp\left[-2.722 \left(\frac{\nu - \nu_0}{2\gamma_V}\right)^2\right] + \frac{\gamma_C \gamma_V}{\gamma_V^2 + (\nu - \nu_0)^2} \\ & + 0.016 \frac{\gamma_C}{\gamma_V} \left(1 - \frac{\gamma_C}{\gamma_V}\right) \left\{ \exp\left[-0.4 \left(\frac{|\nu - \nu_0|}{2\gamma_V}\right)^{2.25}\right] - \frac{10}{10 + (|\nu - \nu_0|/(2\gamma_V))^{2.25}} \right\} \end{aligned} \quad (2.18)$$

with

$$l_{\Phi_V} = \frac{1}{2\gamma_V [1.065 + 0.477 \gamma_C/\gamma_V + 0.058(\gamma_C/\gamma_V)^2]} \quad (2.19)$$

and the Voigt width  $\gamma_V$  (HWHM) approximately given by (Olivero and Longbothum, 1977)

$$\gamma_V = 0.5346\gamma_C + \sqrt{0.2166\gamma_C^2 + \gamma_D^2}. \quad (2.20)$$

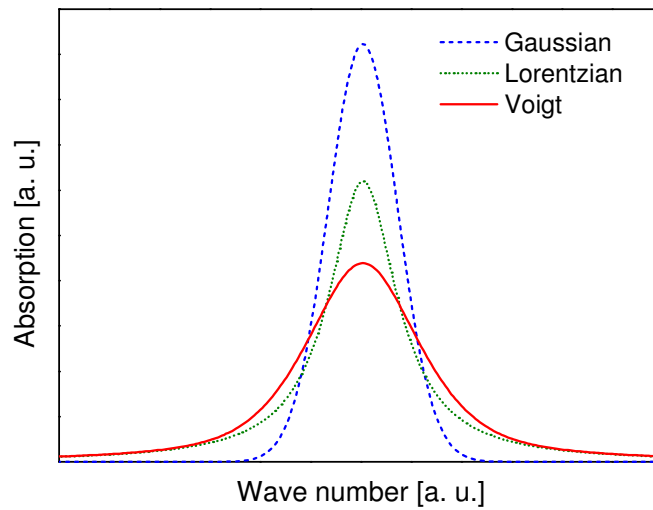


**Figure 2.3** Comparison of Gaussian Doppler broadening, Lorentzian collision broadening, and Voigt absorption line profiles  $\Phi_D$ ,  $\Phi_C$ , and  $\Phi_V$  for Doppler broadening line width  $\gamma_D$  approximately equal to collision broadening line width  $\gamma_C$ . All absorption line profiles are normalized to unit area.

The Voigt profile  $\Phi_V$  can further be extended if interaction between Doppler broadening and collision broadening is taken into account. This leads to the so-called Dicke narrowing (Dicke, 1953) which could be confirmed experimentally (Eng et al., 1972; Lepère et al., 2001). An absorption line profile which incorporates the effect of Dicke-narrowing is the Galatry profile (Galatry, 1961; Ebert and Wolfrum, 2001). It is based on the assumption that collisions between molecules are elastic and lead to changes in the molecular velocity distribution. For our purposes, however, the Voigt profile will be sufficient and extensions of it will not be further pursued.

## 2.3 Direct tunable diode laser absorption spectroscopy

In this thesis, the technique of direct TDLAS is applied, to retrieve absolute concentrations of water vapor (see Chapters 5 and 6). Advantages of direct TDLAS include fast response and time resolution of one second and faster, high sensitivity rivaling that of other TDLAS techniques like wavelength modulation spectroscopy (Reid and Labrie, 1981), wide dynamic range covering concentrations over several orders of magnitude, and high accuracy due to its inherent property of self-calibration. The expression self-calibration is used in the sense that an accuracy for direct TDLAS measurements can be given without any specific and active calibration measures against a calibration standard which is not possible for other common TDLAS techniques (Werle et al., 2002).

For a detailed discussion of all stated aspects of direct TDLAS, it is referred to Chapter 5, whereas the basis for the property self-calibration will be given in Section 2.3.3. As direct TDLAS would not be possible without its main component, a semiconductor diode laser, an introduction to principles and characteristics of these lasers will be given in the following.

### 2.3.1 Diode lasers

‘Laser’ is an acronym standing for ‘light amplification by stimulated emission of radiation’ which marks the fundamental principle that all lasers are based on. The principle of stimulated emission goes back to Albert Einstein who described it in 1916. However, it took over 40 years that the theoretical description of light amplification by stimulated emission could be technically realized. In 1957, C. H. Townes developed the MASER (Microwave Amplification by Stimulated Emission of Radiation). The first laser in the visible spectral region followed in 1960. It was constructed by T. H. Maiman and used a solid-state ruby crystal for production of light. Shortly after, semiconductor diode lasers were developed which marked the beginning of a progress during which lasers have found their way into an extremely wide range of applications defining many aspects of today’s life.

The properties of diode lasers are based on the characteristics of semiconductors which are insulators at absolute zero temperature, but conductors at room temperature. The reason for this behavior is that in a crystalline solid the discrete electronic energy levels of atoms are split into quasi continuous energy bands with many closely spaced levels due to interatomic interaction. Between these energy bands, there are forbidden energy gaps. Just as the outer electrons determine the chemical and optical properties of atoms, the properties of crystalline solids are determined by the electrons in the highest energy bands. If the highest energy band is partially filled, the electrons can take up energy and move in an external electric field resulting in an electric conductor. An insulator is created if the highest occupied energy band is completely filled and the energy gap to the next higher band is large so that electrons cannot overcome it. In a semiconductor, the band gap is small which makes it an insulator at zero temperature at which the highest occupied band called valence band is completely filled and the next higher band called conduction band is empty. At room temperature, however, semiconductors, are – if relatively bad – conductors, since electrons from the valence band can be thermally excited to the conduction band due to band gaps of typically  $\sim 1$  eV for e.g. silicon or germanium.

When an electron moves from the valence band to the conduction band it leaves a ‘hole’ in the valence band which can be treated as positively charged ‘particle’. Both, electrons and holes contribute to an electric current through a semiconductor. However, achievable currents within tetravalent semiconductors as silicon are very low at room temperature, since only few electrons reside in the conduction band. Thus, these semiconductors are doped with atoms of a different element to enhance conductivity by increasing the available number of electrons or

holes. Doping with atoms having an additional electron in the outermost shell such as pentavalent phosphorus or arsenic results in an n-type semiconductor with predominant electron conductivity. Doping with atoms with one electron less in the outermost shell such as trivalent aluminum or gallium on the other hand leads to a p-type semiconductor with predominant hole conductivity.

The usefulness of semiconductors arises from bringing an n-type and a p-type semiconductor together to form a pn junction. This pn junction acts as a diode which lets electric current flow in case of an applied forward voltage, but blocks electric current if a reverse voltage is applied. When electrons from the conduction band recombine with holes in the valence band within the transition zone of the pn junction by emission of photons a light emitting diode is obtained. This process is illustrated in Figure 2.4. Typical energy gaps of semiconductors lead to emission in the NIR spectral region.

A semiconductor diode transforms into a diode laser when the density of electron-hole pairs is high enough that the emitted radiation from electron-hole recombination can stimulate further recombination and the amplification of radiation by stimulated emission exceeds radiative losses. The gain medium of a diode laser consists of a pn junction with an active region in which laser radiation is created. An injection current is applied to this active region to obtain a sufficient number of electron-hole pairs.

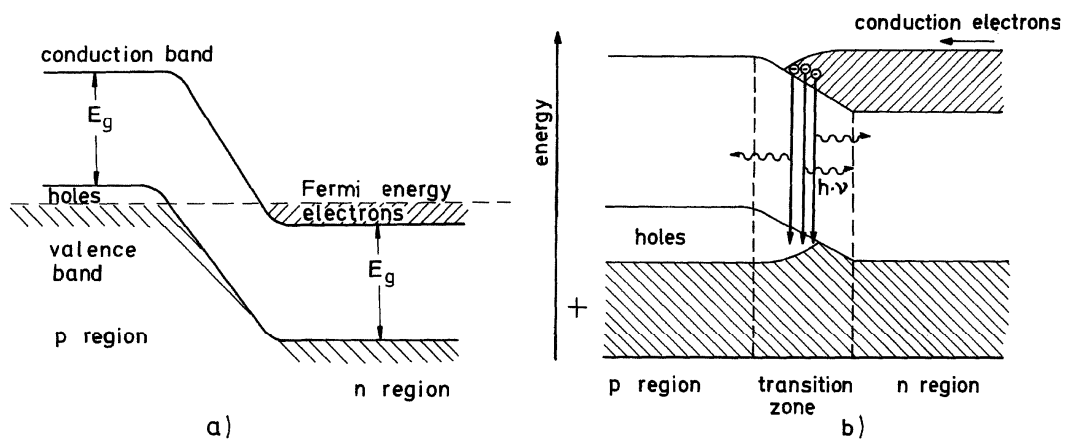


**Figure 2.4** Schematic diagram of a pn junction in a light emitting semiconductor diode. Electronic levels are filled up to the Fermi energy, the energy gap between valence band and conduction band is denoted by  $E_g$ . In an unbiased pn junction (a), electrons in the conduction band of the n region cannot recombine with holes in the valence band of the p region. After applying a forward voltage (b), valence band and conduction band of the n region are shifted to higher energies which makes recombination of electron-hole pairs in the transition zone of the pn junction possible. As consequence, photons with energy  $h \cdot \nu \geq E_g$  are emitted, where  $h$  is Plank's constant and  $\nu$  the frequency of the emitted light. Figure adopted from (Demtröder, 2008b).

Diode lasers do not require mirrors at the end facets of the active region for laser feedback. The reason is that the reflective index of semiconductors is large enough to result in significant Fresnel reflection at the semiconductor-air interface. Further advantages of diode lasers include high efficiency of 40% and more, extremely compact sizes with dimensions of the gain medium of typically less than 1 mm, operation at room temperature, and the ability for wavelength modulation.

### 2.3.2 Distributed feedback diode lasers

In order to obtain single-mode operation with a diode laser, Bragg gratings can be introduced at the ends or sides of the active region. In the so-called distributed Bragg reflector (DBR) design, these gratings are fabricated at both ends of the gain medium and effectively act as wavelength selecting mirrors resulting in feedback in a narrow frequency band. This principle is further advanced in the distributed feedback (DFB) design which was first introduced for dye lasers in 1971 (Kogelnik and Shank, 1971; Shank et al., 1971). DFB diode lasers followed in 1974 (Scifres et al., 1974). In the DFB design, a periodic structure, e.g. consisting of a metal, along the length of the active region acts as Bragg grating. This is illustrated in Figure 2.5. In opposition to the DBR design, feedback in the DFB design occurs continuously throughout the active region rather than at end mirrors. This results in much higher wavelength stability and allows for a wavelength tuning behavior without mode hops.

Temperature-stabilized DFB diode lasers coupled to optical fibers are typically used in the NIR spectral region at wavelengths around 1.5  $\mu\text{m}$  for telecommunication purposes. Commercial single-mode optical fibers with very low optical losses are available for these wavelengths and are employed, e.g., for transatlantic telecommunication. Single mode emission with laser line widths of few megahertz and fiber coupling along with a wavelength tuning behavior free of mode hops also make DFB diode lasers the first choice for TDLAS in the NIR region. For example, the ro-vibrational band of water vapor around 1.4  $\mu\text{m}$  is covered by standard laser and fiber components. For an overview of DFB diode lasers, the spectral range covered by them, and typical applications, see (Zeller et al., 2010).

Newer developments in the DFB design have lead to diode lasers in the wavelength region 2.4-3.0  $\mu\text{m}$  (Hümmer et al., 2006). These lasers make spectroscopy of the water vapor band around 2.7  $\mu\text{m}$  possible which includes fundamental vibrational transitions that are approximately a factor of twenty stronger than in the absorption band around 1.4  $\mu\text{m}$  (Wunderle et al., 2009). However, these products are not aimed at the mass market yet and are therefore rather expensive. Moreover, it is hard to find good single-mode optical fibers in this wavelength region that are suitable for the needs of TDLAS (Klostermann, 2011). Therefore, this thesis focuses on the spectroscopic measurement of water vapor near 1.4  $\mu\text{m}$ .

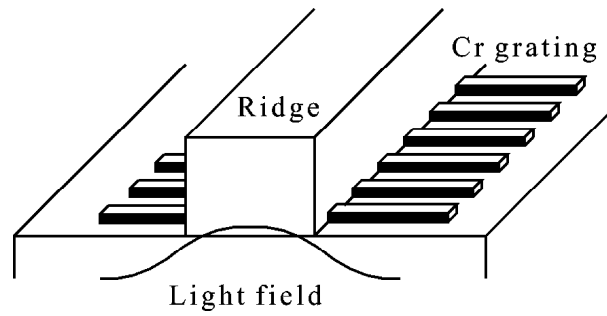


**Figure 2.5** Schematic of a laterally coupled distributed feedback diode laser. The metal Bragg grating – consisting of chromium in this case – which results in single mode operation of the laser is deposited on both sides of a ridge waveguide on top of the active region. Figure adopted from (Kamp et al., 2001).

### 2.3.3 Application of the Beer–Lambert law

Direct TDLAS makes use of the Beer–Lambert law of absorption, in order to determine concentrations of trace gases like water vapor. For this reason, direct TDLAS is often called self-calibrating or calibration-free, since gas concentration can, as we will see, directly be linked to the area of an absorption line obtained by measurement. In its general form, the Beer–Lambert law is expressed by

$$I(\nu) = I_0(\nu) \exp[-a(\nu) \cdot L], \quad (2.21)$$

where  $I(\nu)$  is the transmitted EM radiation intensity,  $I_0(\nu)$  the incident EM radiation intensity,  $a(\nu)$  the (positive) absorption coefficient, and  $L$  the absorption path length. The spectral position in wave number domain  $\nu$  is typically expressed in terms of wave number unit  $\text{cm}^{-1}$ . The absolute value of the exponent in (2.21) is called optical density

$$\text{OD}(\nu) \stackrel{\text{def}}{=} -\ln \left[ \frac{I(\nu)}{I_0(\nu)} \right] = a(\nu) \cdot L. \quad (2.22)$$

If absorption is caused by a single absorption line, the absorption coefficient  $a(\nu)$  is proportional to the molar concentration of the absorber  $n_{\text{abs}}$  and the temperature dependent absorption line strength  $S(T)$ :

$$a(\nu) = S(T) \cdot \Phi(\nu - \nu_0) \cdot n_{\text{abs}}, \quad (2.23)$$

where  $\Phi(\nu - \nu_0)$  is the absorption line profile normalized to unit area and centered at line position  $\nu_0$ .  $\Phi(\nu - \nu_0)$  is expressed by a suitable mathematical formulation such as the Voigt profile  $\Phi_V$  which was introduced in Section 2.2.4. Line strengths for individual absorption lines can be obtained from databases such as HITRAN (Rothman et al., 2009).

The absorber concentration  $n_{\text{abs}}$  can be determined by integration of (2.21) over the spectral domain

$$n_{\text{abs}} = -\frac{1}{S(T) \cdot L} \int_{-\infty}^{+\infty} \ln \left[ \frac{I(\nu)}{I_0(\nu)} \right] d\nu = \frac{A}{S(T) \cdot L}, \quad (2.24)$$

where use of (2.22), (2.23) as well as normalization of  $\Phi$  has been made and for the area of an absorption line  $A$ , the following definition has been used

$$A \stackrel{\text{def}}{=} \int_{-\infty}^{+\infty} \text{OD}(\nu) d\nu = S(T) \cdot L \cdot n_{\text{abs}}. \quad (2.25)$$

Equation (2.24) is the basis for the property of self-calibration of direct TDLAS – the direct proportionality between  $n_{\text{abs}}$  and  $A$ . Note that if  $n_{\text{abs}}$  is not uniform along the absorption path  $L$ , (2.24) yields an  $n_{\text{abs}}$  value which represents the average absorber concentration along  $L$ .

Absorber concentration can also be formulated in terms of volume mixing ratio (VMR). In order to do so, we have to introduce the ideal gas law

$$n_{\text{abs}} = \frac{p_{\text{abs}}}{k_B \cdot T}, \quad (2.26)$$

where  $p_{\text{abs}}$  is the partial pressure of the absorber,  $T$  the temperature, and  $k_B$  the Boltzmann constant. Absorber concentration  $c_{\text{abs}}$  in VMR can then be expressed by

$$c_{\text{abs}} = \frac{p_{\text{abs}}}{p} = \frac{n_{\text{abs}} \cdot k_B \cdot T}{p} \quad (2.27)$$

with the total gas pressure  $p$ .  $c_{\text{abs}}$  is typically given in units of ppmv (parts per million by volume) or ppbv (parts per billion by volume) for trace gas concentrations. Inserting (2.27) into (2.24) yields

$$c_{\text{abs}} = -\frac{k_B \cdot T}{S(T) \cdot L \cdot p} \int_{-\infty}^{+\infty} \ln \left[ \frac{I(\nu)}{I_0(\nu)} \right] d\nu. \quad (2.28)$$

In direct TDLAS, wavelength variation is obtained by time-dependent modulation of the diode laser current. This results in a dynamic spectral tuning behavior of the laser  $d\nu/dt$  which can be used to transform (2.28) into an integration over time

$$c_{\text{abs}} = -\frac{k_B \cdot T}{S(T) \cdot L \cdot p} \int_{-\infty}^{+\infty} \ln \left[ \frac{I(\nu(t))}{I_0(\nu(t))} \right] \frac{d\nu}{dt} dt. \quad (2.29)$$

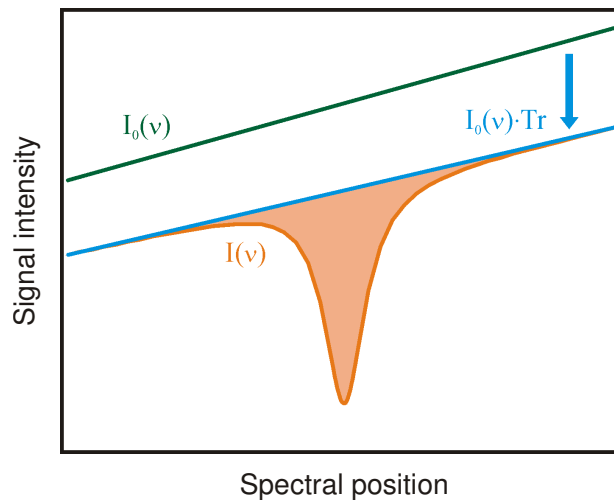


**Figure 2.6** Illustration of the Beer–Lambert law in direct tunable diode laser absorption spectroscopy including transmission signal perturbations  $\text{Tr}$ .  $I_0(\nu)$  denotes the unperturbed incident signal intensity,  $I(\nu)$  the absorption signal intensity with perturbations, and  $\nu$  the spectral position.

The dynamic tuning behavior  $d\nu/dt$  of the diode has to be characterized for given laser operating conditions (laser temperature and modulation of laser current), in order to obtain an accurate result for  $c_{\text{abs}}$  without any calibration measures, see e.g. (Hunsmann, 2009). For DFB diode lasers, this procedure has to be carried out only once in a few years, as these lasers are very long-term stable in terms of emitted wavelength. Average variations in  $d\nu/dt$  over several years are typically below 1% (Hunsmann, 2009).

Another advantageous feature of direct TDLAS is the insensitivity to broad band perturbations of the measured signal intensity  $I(\nu)$ . This applies, e.g., for transmission losses caused by light scattering off particles in the absorption path. These transmission losses are denoted by  $\text{Tr}$  and enter the Beer–Lambert law (2.21) as follows

$$I(\nu) = I_0(\nu) \cdot \text{Tr} \cdot \exp[-\text{OD}(\nu)]. \quad (2.30)$$

Their effect on the measured signal intensity  $I(\nu)$  is depicted in Figure 2.6. Incorporating  $\text{Tr}$  into (2.29) yields

$$c_{\text{abs}} = -\frac{k_B \cdot T}{S(T) \cdot L \cdot p} \int_{-\infty}^{+\infty} \ln \left[ \frac{I(\nu(t))}{I_0(\nu(t)) \cdot \text{Tr}} \right] \frac{d\nu}{dt} dt. \quad (2.31)$$

Transmission losses play a particular role for the TDL hygrometers in operation at the cloud chamber AIDA which will be introduced in the following chapter. As we will see in Chapter 5, the cloud particle densities obtained in AIDA expansion experiments can lead to severe

transmission losses well above 50%. Transmission losses up to 99% can be handled without negative impact on the TDLAS measurement.

In actual measurement applications, the integration in (2.31) cannot be performed from minus to plus infinity, but only over a confined time domain. It is therefore necessary to develop specialized algorithms for measurement data evaluation, in order to retrieve absorption line areas  $A$  and absorber concentrations  $c_{\text{abs}}$ . For reliable measurement results, these algorithms have to be accurate as well as robust. One example for such an algorithm will be presented in Chapter 4.

## Chapter 3

# Aerosol and cloud chamber AIDA

The AIDA (Aerosol Interactions and Dynamics in the Atmosphere) cloud and aerosol chamber at the Karlsruhe Institute of Technology is a unique facility for studies of aerosol-cloud interactions and ice nucleation in mixed phase clouds (Möhler et al., 2008; Niemand et al., 2011), cirrus clouds (Möhler et al., 2003; Möhler et al., 2006; Murray et al., 2010) as well as polar stratospheric and noctilucent clouds (Saunders et al., 2010). Moreover, it provides ideal conditions for examination of aerosol chemistry and nucleation (Saathoff et al., 2009) as well as aerosol optical properties (Wagner et al., 2009). Due to the long lasting experience in ice cloud studies and the excellent instrumentation of the AIDA facility, AIDA is perfectly suited for the ice particle growth experiments presented in Chapter 6

The AIDA chamber consists of an aluminum vacuum vessel with a diameter of four meters, a height of 7.5 meters, and a volume of 84.3 m<sup>3</sup>. This large volume keeps boundary effects from the aluminum wall such as temperature and humidity gradients confined to a small fraction of the total volume. The vessel is placed in an isolating and thermostated housing which allows an operation temperature range between  $-90$  °C and  $+60$  °C. Gas temperature inside the AIDA chamber is measured with an accuracy of  $\pm 0.3$  K (Möhler et al., 2006). A mixing fan keeps the gas volume inside the vessel homogeneous which results in temperature differences within the entire gas volume of less than  $\pm 0.2$  K under static conditions (Möhler et al., 2006). Two vacuum pumps allow gas pressures from ambient pressure down to 0.01 hPa. Available cooling rates range from 0.1 K/min to 6 K/min. Low cooling rates are achieved by decreasing temperature of the AIDA wall while high cooling rates are a result of adiabatic cooling by gas pressure reduction due to pumping.

### 3.1 Instrumentation

In the following, an overview of a typical AIDA instrumentation will be given, which also applies to the cirrus cloud experiments presented in Chapter 6, cf. (Wagner et al., 2009). A schematic drawing of AIDA with the individual instruments is depicted in Figure 3.1.

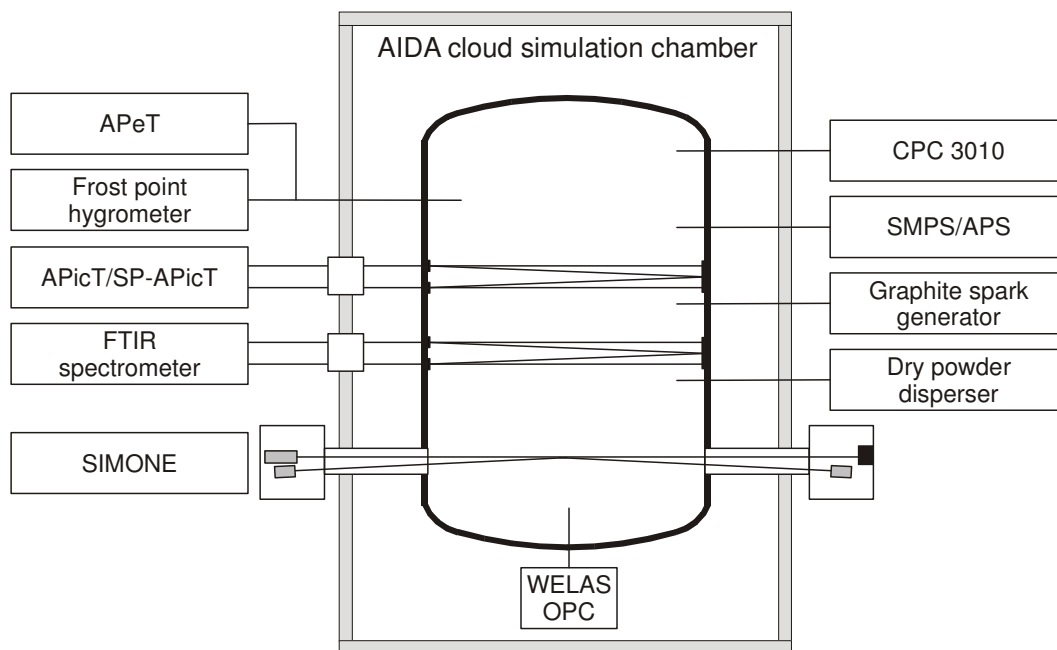


**Figure 3.1** Schematic drawing of the AIDA cloud chamber with instrumentation for humidity measurements (APicT, SP-APicT, APeT, and chilled-mirror frost point hygrometer), ice particle characterization (FTIR spectrometer, SIMONE, and WELAS optical particle counter), aerosol generation (graphite spark generator and dry powder disperser), and aerosol characterization (CPC 3010, SMPS, and APS). The gray frame illustrates the thermostated isolating housing surrounding the AIDA chamber.

*Humidity:* For in situ measurement of water vapor concentration and partial pressure, respectively, as well as extractive measurement of total water content, three tunable diode laser (TDL) hygrometers operating at a wavelength of 1370 nm are available at AIDA. Time resolution of these three TDL hygrometers is approximately 1 s, accuracy is given at  $\pm 5\%$ . A comprehensive discussion of the TDL instruments will be given in Chapter 5. In situ water vapor measurement is performed by APicT (AIDA PCI in cloud TDL) accompanied by its single-path version SP-APicT. Total water content is retrieved by extractive sampling of AIDA gas via a heated stainless steel line to which APeT (AIDA PCI extractive TDL) is connected. From the difference of total water and water vapor measurements, ice water/liquid water content can be derived. Attached to the same sampling line is a chilled-mirror frost point hygrometer (MBW, 373LX) with a nominal time resolution of 1 s and accuracy given by the manufacturer of  $\pm 0.1$  K frost point which translates into an accuracy in water partial pressure ranging from  $\pm 0.8\%$  at  $T = 0^\circ\text{C}$  to  $\pm 1.8\%$  at  $T = -90^\circ\text{C}$  (Murphy and Koop, 2005). For a description of the measurement principle of frost point hygrometers, see (Vömel et al., 2007). Water partial pressure  $e$  obtained by the different humidity instruments can be converted into saturation ratio  $S$  over liquid water as well as over ice by calculating the

respective water vapor saturation pressure  $\hat{e}$  with respect to AIDA gas temperature  $T_g$  (Murphy and Koop, 2005):  $S_{\text{ice/wat}} = e/\hat{e}_{\text{ice/wat}}(T_g)$ . The accuracy of the retrieval of  $S$  is therefore not only determined by the accuracy of the individual hygrometers, but also by the uncertainty of gas temperature  $T_g$ .

*In situ ice water content:* A Fourier transform infrared (FTIR) spectrometer (Bruker, IFS66v) obtains infrared extinction spectra of ice particles in situ in the AIDA chamber in the spectral range 800- 6000  $\text{cm}^{-1}$  at a resolution of 4  $\text{cm}^{-1}$ . From these spectra ice water content as well as ice particle number concentrations and size distributions can be inferred. Time resolution of the instrument is 10 s, accuracy for ice water content is given at  $\pm 10\%$  (Wagner et al., 2006).

*Ice number concentration:* An optical particle counter (OPC; PALAS, WELAS) is available to register ice particle number concentrations for particles in the size range 0.6-40  $\mu\text{m}$ . It counts particles by measuring the pulses of white light scattered by individual particles. The instrument is typically operated at 5 s time resolution. Its accuracy is estimated to be  $\pm 20\%$  (Möhler et al., 2006).

*In situ laser light scattering:* The in situ light scattering and depolarization instrument SIMONE (Scattering Intensity Measurement for the Optical Detection of ice) detects light scattered by aerosol or cloud particles in forward ( $2^\circ$ ) and backward ( $178^\circ$ ) direction. It uses a continuous wave semiconductor laser at 488 nm wavelength. In addition, parallel as well as perpendicular polarization intensity of the backward direction signal can be detected. Due to its high sensitivity, SIMONE is able to precisely determine the onset of cloud particle generation. Further details about the instrument can be found in (Schnaiter et al., 2011).

*Aerosol generation:* For injection of aerosol particles into the AIDA chamber, two aerosol generators are available. A dry powder disperser (TSI, model 3433) for addition of solid aerosol particles and a graphite spark generator (PALAS, GFG 1000) which creates soot particles by spark discharge between two electrodes of pure carbon. The obtained soot particles with sizes mainly in the range 100-200 nm are agglomerates of primary soot particles with diameters below 10 nm. For details on creation, morphology, and properties of GSG soot, see (Möhler et al., 2005) and references therein.

*Aerosol characterization:* Aerosol number concentration is measured by a condensation particle counter (TSI, CPC 3010). Aerosol size distribution is determined by a scanning mobility particle sizer (SMPS, TSI) in combination with an aerodynamic particle sizer (APS, TSI).

## 3.2 AIDA cloud expansion experiments

Controlled expansion cooling experiments at AIDA can be achieved by operation of the vacuum pumps at variable pumping speeds resulting in typical cooling rates between 0.5 K/min and 3 K/min. These expansion experiments simulate the adiabatic expansion cooling that ascending air parcels experience in the atmosphere. The temperature decrease resulting from adiabatic cooling eventually leads to supersaturated water vapor conditions and the formation of cloud droplets or ice particles from seed aerosol particles. Time evolution of a typical AIDA cirrus, i.e., pure ice cloud experiment is depicted in Figure 3.2. This experiment is also representative of the experiments presented in Chapter 6.

Initialization of pumping, i.e. initialization of the adiabatic expansion, from an initial gas pressure around ambient pressure ( $\sim 1$  atm) defines the start of an AIDA experiment. Subsequently, gas pressure and temperature decrease while temperature of the AIDA vessel wall stays nearly constant due to its high heat capacity. With decreasing temperature, the saturation ratio of water vapor as well as total water with respect to ice increases until onset of ice particle formation occurs due to different possible ice nucleation mechanisms. These nucleation mechanisms are typically heterogeneous deposition nucleation as a result of water vapor deposition directly on a solid aerosol particle (Möhler et al., 2006) or homogeneous nucleation of supercooled solution droplets (Koop et al., 2000; Möhler et al., 2003). Other heterogeneous nucleation mechanisms like immersion freezing are typically not relevant for the experimental conditions used in this work. Ice onset is followed by a steep increase of ice particle number concentration as well as of ice water content due to growth of the ice particles. This particle growth leads to a parallel depletion of water vapor supersaturation until water vapor saturation ratios near unity are approached. The end of an experiment is typically marked by stopping the pumping process followed by slow evaporation of the ice cloud.

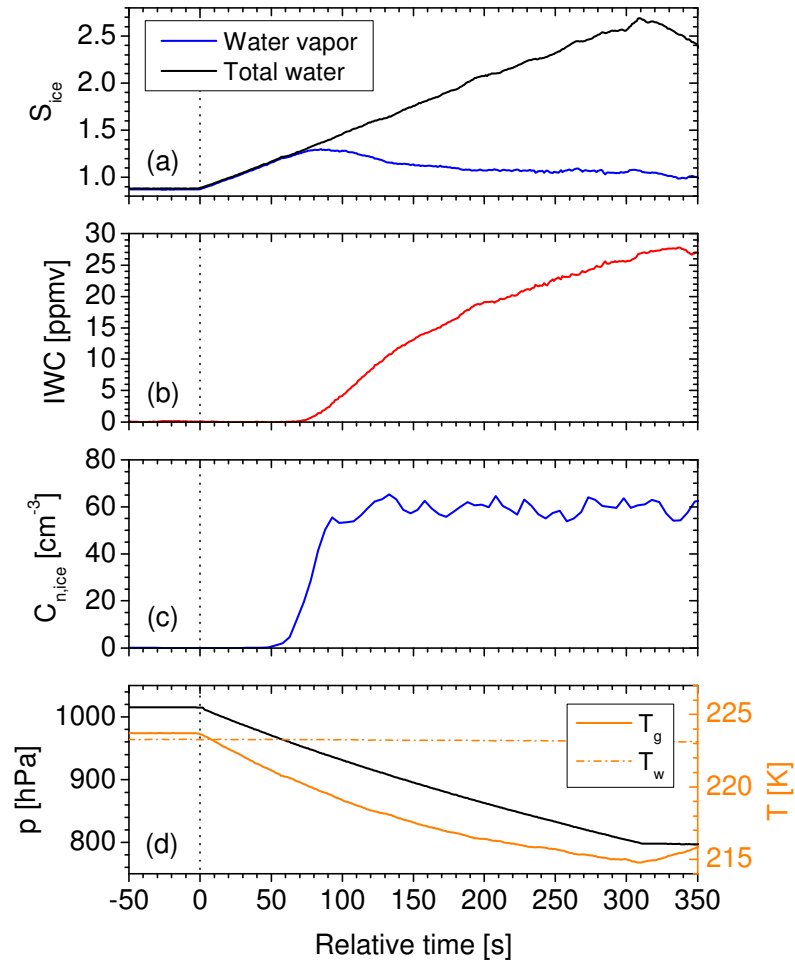


**Figure 3.2** Time series of a typical AIDA expansion experiment. (a) Saturation ratio over ice  $S_{ice}$  derived from APicT water vapor content and APeT total water content; (b) ice water content IWC inferred from APicT water vapor and APeT total water measurement; (c) ice number concentration  $C_{n,ice}$  as measured by the WELAS optical particle counter; (d) thermodynamic variables during expansion: decrease of gas pressure  $p$  and temperature  $T_g$  while wall temperature  $T_w$  of the AIDA vessel remains approximately constant. The dotted line indicates the start of the experiment, i.e. start of pumping.



## Chapter 4

# Integrative fitting of absorption line profiles

Reliable data evaluation procedures are essential for any absorption spectroscopic measurement. In case of direct absorption spectroscopy which retrieves absorber concentrations from single absorption line measurements, this comes down to how accurately an evaluation algorithm can retrieve the area enclosed by a considered absorption line. This area is proportional to the quantity of the absorber concentration.

One quite basic approach to retrieve absorption line areas is the principle of integrative evaluation. Its functionality and properties will be laid out in the following section. Its extension resulting in the development of the novel advanced integrative (AI) fitting algorithm will be described in the subsequent section. The AI fitting algorithm retains the advantages of previous implementations of the integrative evaluation – speed and robustness – but improves accuracy of fit results significantly under typical measurement conditions by introduction of an iterative fitting process. This approach is new in the field of integrative evaluation. A comparison of the novel AI fitting algorithm with the widely common Levenberg–Marquardt (LM) fitting algorithm follows and a discussion of the advantages and disadvantages of the AI algorithm compared to the LM algorithm will close this chapter.

### 4.1 Principle of integrative evaluation

The basic principle of integrative evaluation is straight forward. For linear absorption, the concentration of an examined absorber  $c_{\text{abs}}$  is proportional to the area  $A$  enclosed by an absorption line of the absorber and  $A$  can be retrieved from an absorption line signal  $\text{OD}(\nu)$  in optical density representation by integrating over the entire spectral domain  $\nu$  (cf. Section 2.3.3)

$$c_{\text{abs}} \propto \int_{-\infty}^{+\infty} \text{OD}(\nu) d\nu \equiv \int_{-\infty}^{+\infty} A \cdot \Phi(\nu) d\nu = A \int_{-\infty}^{+\infty} \Phi(\nu) d\nu = A, \quad (4.1)$$

where  $\Phi$  denotes the area normalized profile function of the absorption line which can be described, e.g., by a Voigt profile  $\Phi_V$  (Armstrong, 1967). Since  $\Phi$  does not have to be known explicitly, this kind of evaluation can be performed with very little effort and no actual fitting process is involved. However, it is a fast and very robust method to get a measure for  $c_{\text{abs}}$ .

In reality, the simple method described in (4.1) lacks accuracy if one or several of the following conditions apply.

1. The measured absorption line signal OD includes a varying background, caused e.g. by signal transmission fluctuations.
2. A real measurement cannot cover the entire spectral domain from  $-\infty$  to  $+\infty$ . Thus, the actually retrieved absorption line area is underestimated because the flanks of the absorption line are not entirely included in the spectral measurement interval. This typically is of importance at gas pressures above  $\sim 100$  hPa for which absorption lines are not well represented by a Gaussian profile as for lower pressures. Since absorption line width increases with increasing gas pressure, the impact of line flanks not being covered by the measurement becomes greater with increasing gas pressure as well.
3. Further absorption lines, which lie within the spectral measurement interval, can contribute significantly, but not quantifiable to the measurement signal OD.

All three points make additional corrections necessary. Measures to address the first point go back to (Riedel et al., 1978) where an additional reference integration interval outside the measurement integration interval was used to correct for a constant background. By adding further reference integration intervals, this method was extended to correct for higher order polynomial backgrounds (Riedel et al., 1982; McCaul et al., 1995; Pleban, 1998; Pleban et al., 1999). No further developments seem to have been conducted thereafter.

The second point was neglected except in (Riedel et al., 1982) and (Pleban, 1998; Pleban et al., 1999). In their implementations, a factorial correction – based on comparison of two or more different measurement integration intervals – was applied to perform a first order correction for parts of the absorption line not covered by the measurement interval. The third point is generally complicated to address in integrative evaluation methods and corresponding corrections could not be incorporated into any available integrative method so far. Therefore, previous implementations of the principle of integrative evaluation exhibit a general lack of accuracy unless measurement conditions can be restricted to gas pressures far below standard pressure, i.e. below 100 hPa, to obtain sufficiently narrow absorption lines, and contributions of further absorption lines besides the measurement absorption line can be neglected. A possibility to mitigate the lack of accuracy of existing integrative evaluation methods would be the frequent calibration of the evaluation method during a measurement. This is, however, not always possible or desired.

Besides a general lack of accuracy, the previous implementations of integrative evaluation offered no indicator of measurement result quality, e.g. by output of a signal to noise ratio. On

the other hand, the principle of integrative evaluation only involves basic mathematical operations even when the simple method described in (4.1) is extended, e.g. by signal background correction, and could therefore be realized by means of analog circuits which made data evaluation very fast and robust.

## 4.2 Development of the advanced integrative fitting algorithm

With the exception of multi absorption-line fitting, the AI fitting algorithm has been developed to overcome the shortcomings of previous implementations of integrative evaluation – a lack of accuracy and indication of fit quality – combined with retaining the advantages – robustness and speed – to obtain accurate and reliable results from direct absorption spectroscopy measurements. In its properties, the AI fitting algorithm thus equals much more a versatile and universally applicable fitting algorithm like the LM algorithm (Marquardt, 1963; Press et al., 2007).

The high accuracy of the AI fitting algorithm is the result of an active fitting procedure with iterative improvement of fit results which has been introduced for the first time in the field of integrative evaluation of absorption lines<sup>1</sup>. Application areas of the algorithm could incorporate measurements under highly variable conditions that have to be evaluated with high time resolution ( $\leq 1$  ms) and high fit accuracy ( $\leq 1\%$ ) such as airborne in situ measurements of atmospheric trace gases (Gurlit et al., 2005; May, 1998) or in situ gas analysis of combustion processes (Teichert et al., 2003).

### 4.2.1 Functionality

In order to illustrate the functionality of the AI fitting algorithm, simulated data are used. Figure 4.1 shows simulated data with an absorption line signal OD represented by an analytical approximation (Whiting, 1968; Olivero and Longbothum, 1977) of a Voigt profile  $\Phi_V$ , see Equations (2.18)-(2.20) in Section 2.2.4. The Voigt profile is calculated for a half width at half maximum (HWHM)  $\gamma_V$  of approximately  $0.1 \text{ cm}^{-1}$ , a value which is typical for e.g. water vapor in the near infrared (NIR) at standard conditions (1 atm, 0 °C, cf. Rothman et al., 2009). Contained in the signal is a background BG which is, in this case, simulated by a polynomial of second order. This background has to be corrected for during the fitting procedure. The measurement interval corresponds to approximately  $1 \text{ cm}^{-1}$ , a typical value for tunable diode-laser absorption spectroscopy (TDLAS). Note that the absorption line does

---

<sup>1</sup> Although the iterative evaluation of absorption line profiles by an LM fitting algorithm can, in principle, be regarded to be based on (4.1), the LM algorithm is not counted as an integrative algorithm here, since no actual integration is involved in the fitting procedure.

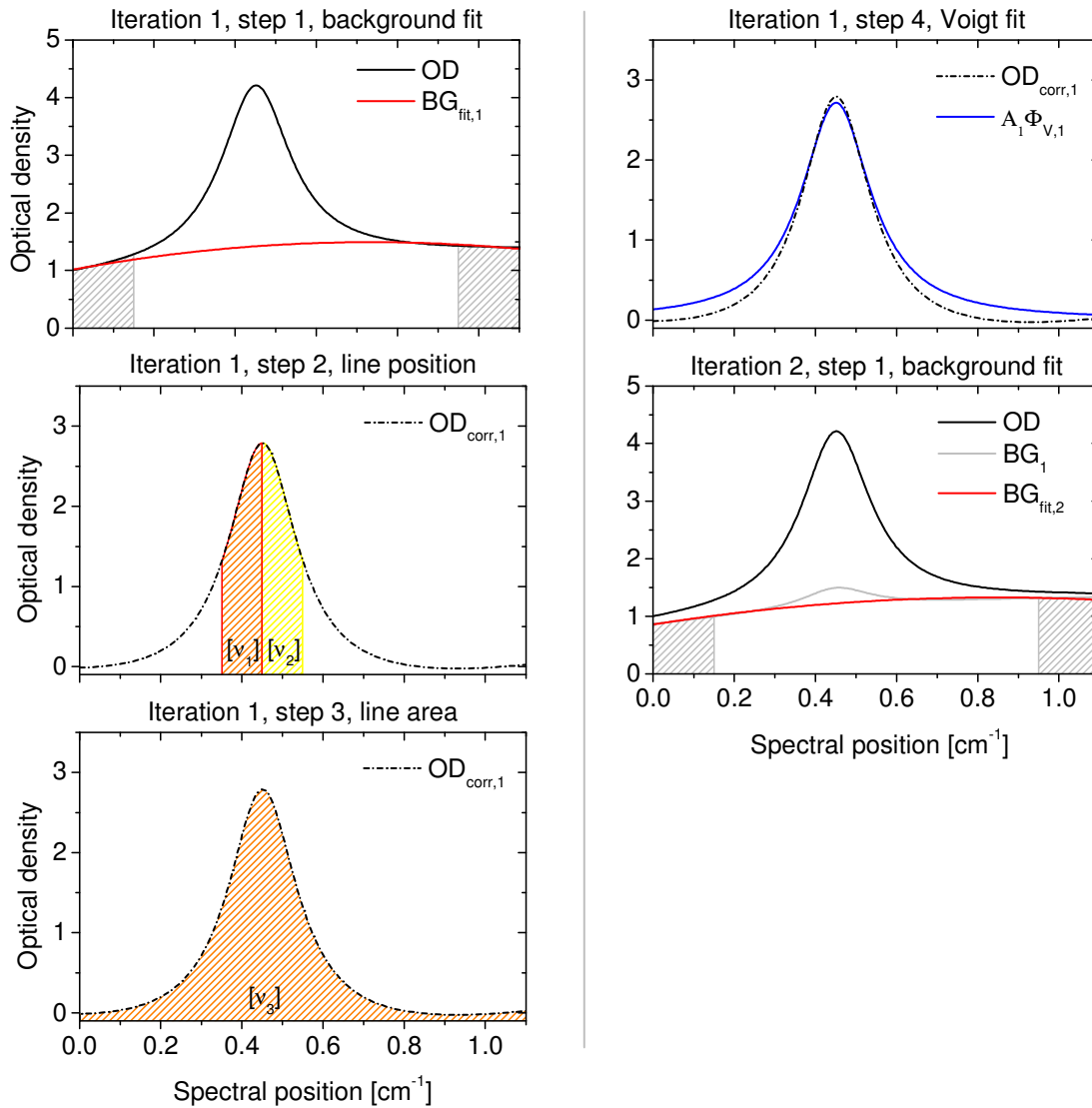


**Figure 4.1** Illustration of the different steps (iteratively repeated with iteration index  $i$ ) of the advanced integrative algorithm for simulated data. Only the first iteration plus step one of the second iteration are shown. Subsequent steps follow the corresponding steps of iteration one. OD denotes the absorption signal,  $BG_{\text{fit},i}$  the fitted background polynomial,  $OD_{\text{corr},i}$  the background-corrected absorption signal,  $A_i\Phi_{V,i}$  the fitted absorption line profile with  $A_i$  the absorption line area and  $\Phi_{V,i}$  the normalized Voigt function, and  $BG_i$  the background approximation used for the subsequent iteration.  $[\nu.]$  denotes the spectral intervals evaluated.

not have to be positioned symmetrically in the measurement interval. Furthermore, its position does not have to be fixed during the measurement which makes special measures for laser frequency stabilization no prerequisite.

The functionality of the AI algorithm consists of different steps, described in detail in the following. These steps are repeated iteratively with  $i$  denoting the iteration index to improve the fit result of the absorption line area  $A_i$  which is the quantity of interest.

### Step 1: background correction

In order to correct for the background BG in the first iteration (background correction in subsequent iterations will be described later on), a polynomial fit  $BG_{\text{fit},i=1}$  to the flanks of the absorption line signal OD, indicated by the grey shaded intervals in Figure 4.1, is applied, similar to (Riedel et al., 1982; McCaul et al., 1995; Pleban, 1998; Pleban et al., 1999). The flanks are represented by the outer parts of the spectral measurement interval and are most suitable to apply a background fit because influence of the absorption line is minimal here. The polynomial fit is an optimized version of the general linear least square method described in (Press et al., 2007) with optimizations<sup>2</sup> taking into account that a special linear problem (polynomial) has to be evaluated. Therefore, polynomial order can be chosen freely as in (Pleban, 1998; Pleban et al., 1999), in contrast to the previous algorithms in (Riedel et al., 1982; McCaul et al., 1995) which support a polynomial background correction of first order only. The absorption line signal OD is corrected by  $BG_{\text{fit},i}$  to

$$OD_{\text{corr},i} = OD - BG_{\text{fit},i}. \quad (4.2)$$

### Step 2: line position

The determination of the line position  $\nu_0$  is similar to the approach in (Preier et al., 1989; McCaul et al., 1995; Pleban, 1998; Pleban et al., 1999). Two symmetric intervals  $[\nu_1]$  and  $[\nu_2]$  are chosen around an initially assumed line position  $\nu_{i,0}$ . This initial condition is determined from the maximum of  $OD_{\text{corr},i}$ . Typically, the width of  $[\nu_1]$  and  $[\nu_2]$  is selected to approximately match the Voigt width  $\gamma_V$  for fast and stable results. For trace gas measurements with negligible self broadening contribution of the absorber,  $\gamma_V$  can directly be computed from gas pressure and temperature data.

Let us define

---

<sup>2</sup> In the matrix inversion process of the general linear least square method, polynomial element  $x^n$  does not have to be computed explicitly, but can be computed from  $x \cdot x^{n-1}$  ( $n \in [2, 2p]$  where  $p$  denotes the polynomial degree). This approach needs only one multiplication instead of  $n - 1$  multiplications to compute  $x^n$ .

$$\delta_0 := \int_{[\nu_1]} \text{OD}_{\text{corr},i} - \int_{[\nu_2]} \text{OD}_{\text{corr},i}. \quad (4.3)$$

If  $\nu_{i,0} = \nu_0$ , it follows that  $\delta_0 \approx 0$  due to the symmetry of the Voigt profile  $\Phi_V$ . For  $\nu_{i,0} \neq \nu_0$ , the following approach can be applied. The absorption line profile is approximated by a Lorentzian function with HWHM  $\gamma_V$  that is expanded to quadratic order around  $\nu_0$ .  $\delta_0$  can then be used to iteratively (iteration index  $j$ ) improve the result for the line position:

$$\nu_{i,j+1} = \nu_{i,j} - \frac{1}{6} \delta_j \frac{\gamma_V}{\Sigma}, \quad (4.4)$$

where  $\delta_j$  is the generalization of  $\delta_0$  in (4.3) with the intervals  $[\nu_1]$  and  $[\nu_2]$  now chosen symmetrically around  $\nu_{i,j}$  and  $\Sigma$  is defined as

$$\Sigma := \int_{[\nu_1]+[\nu_2]} \text{OD}_{\text{corr},i}. \quad (4.5)$$

The iteration process is terminated if the quantity

$$\varepsilon_\nu := \left| \frac{\nu_{i,j+1} - \nu_{i,j}}{\nu_{i,j}} \right| \quad (4.6)$$

falls below a prescribed value. The resulting best fitting value for the line position will be called  $\nu_i$  in the following.

### Step 3: line area

The absorption line area  $A_i^*$  within the measurement interval  $[\nu_3]$  is determined by integrating  $\text{OD}_{\text{corr},i}$  over  $[\nu_3]$ .

$$A_i^* = \int_{[\nu_3]} \text{OD}_{\text{corr},i}. \quad (4.7)$$

$A_i^*$  has to be corrected for the area within the flanks of the absorption line which are not covered by  $[\nu_3]$ . This can be done by calculating the normalized Voigt function  $\Phi_{V,i}$  from the absorption line position  $\nu_i$  from step two and the computed pressure and temperature-dependent absorption line width  $\gamma_V$ . Here, the analytical approximation by (Whiting, 1968; Olivero and Longbothum, 1977) is used for  $\Phi_{V,i}$ , see Equations (2.18)-(2.20). The corrected absorption line area  $A_i$  is then given by

$$A_i = \frac{A_i^*}{\int_{[\nu_3]} \Phi_{V,i}}. \quad (4.8)$$

**Step 4: Voigt fit**

The absorption line profile  $A_i\Phi_{V,i}$ , computed with the results from steps two and three is a better representation for the actually measured absorption line than  $OD_{\text{corr},i}$ , mainly because the flanks of the absorption line are better represented. Therefore,  $A_i\Phi_{V,i}$  can be used to get an approximation for the actual background

$$BG_i = OD - A_i\Phi_{V,i}. \quad (4.9)$$

In principle, any other symmetric profile function besides the Voigt profile can be used in steps three and four, as long as the absorption line width can be precomputed. Also note that the AI fitting algorithm does not need explicit start values for the fit parameters (line area, line position, and background polynomial coefficients) for initialization.

**Step 1, second and subsequent iterations**

Corresponding to step one in the first iteration a polynomial  $BG_{\text{fit},i+1}$  is fitted to  $BG_i$  from the previous iteration. All other steps follow the same manner as the corresponding steps described before.

As terminating condition for the iterative process, the relative deviation of the line area between two subsequent iterations

$$\varepsilon_A := \left| \frac{A_{i+1} - A_i}{A_i} \right| \quad (4.10)$$

can be used. If  $\varepsilon_A$  falls below a prescribed value, the iterative process is stopped.

Figure 4.2 depicts the fit precision of the integrative algorithm with increasing iteration index  $i$ . Since simulated data are used, the actual background  $BG$  is known and shown in Figure 4.2. The convergence of the fitted background  $BG_{\text{fit},i}$  to the actual background  $BG$  is illustrated, together with the convergence of the calculated absorption line profile  $A_i\Phi_{V,i}$  to the background-corrected absorption signal  $OD_{\text{corr},i}$ . This convergence is also illustrated by the residual  $\text{res}_i$ , defined as

$$\text{res}_i = OD_{\text{corr},i} - A_i\Phi_{V,i}. \quad (4.11)$$

A total number of six iterations is necessary to fulfill the chosen terminating conditions  $\varepsilon_A < 10^{-3}$  and  $\varepsilon_v < 10^{-4}$  which yield a fit precision of the line area  $A_6$  of at least  $10^{-3}$  and of the line position  $v_6$  of at least  $10^{-4}$ , respectively.

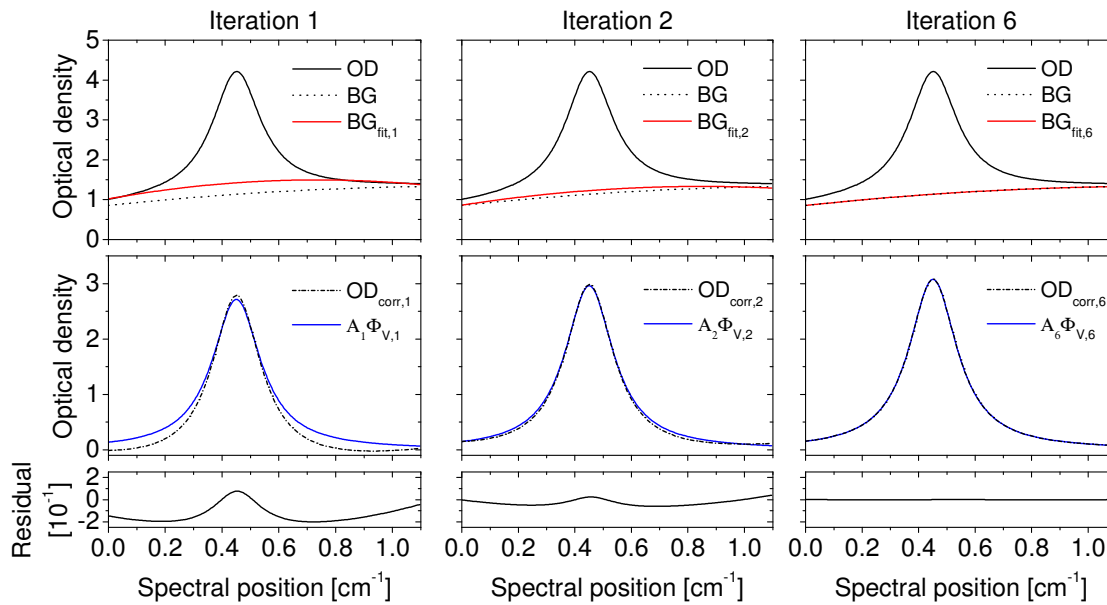


**Figure 4.2** Illustration of the advanced integrative fit precision with increasing iteration index  $i$ . In this example, six iterations are needed for the fulfillment of the following terminating conditions: relative change in line position  $\varepsilon_v < 10^{-4}$ , relative change in line area  $\varepsilon_A < 10^{-3}$ . This corresponds to a fit precision of the line area  $A_6$  of at least  $10^{-3}$ . BG denotes the actual background which is prescribed in the simulated data (polynomial of second order), labeling is otherwise the same as in Figure 4.1.

The residual  $\text{res}_i$  makes the calculation of a signal to noise ratio as indicator for the fit quality possibly – in contrast to previous implementations of the principle of integrative evaluation. The signal to noise ratio  $S/N_{3\sigma,i}$  can be defined as

$$S/N_{3\sigma,i} = \frac{\max[\text{OD}_{\text{corr},i}]}{3 \cdot \sigma_{\text{res}_i}}, \quad (4.12)$$

where  $\sigma_{\text{res}_i}$  denotes the standard deviation of the residual  $\text{res}_i$ . This definition gives the signal to noise ratio at a level of  $3\sigma$ .

Table 4.1 shows the convergence process of the AI fitting algorithm quantitatively together with the fit quality indicator  $S/N_{3\sigma,i}$ . Already in the first iteration the absorption line position is surprisingly accurate despite the deviation between  $\text{BG}_{\text{fit},i}$  and BG. This does not hold for the absorption line area which is the quantity of actual interest. In the first iteration, the deviation of  $A_1$  from the actual value is above 10%, a value which is unacceptable for many applications, but would be representative for some of the previous integrative algorithms (Riedel et al., 1978; McCaul et al., 1995) under the conditions applied here. The more advanced implementations with additional correction of retrieved absorption line area (Riedel et al., 1982; Pleban, 1998; Pleban et al., 1999) are estimated to correspond to the result of the second iteration  $A_2$  which still deviates 4% from the actual value.

Iteration $i$	Rel. dev. line area	Rel. dev. line position	$S/N_{3\sigma,i}$
1	0.118	4E-4	12
2	0.038	3E-4	38
3	0.012	3E-4	119
4	0.004	2E-4	339
5	0.001	2E-4	726
6	<0.001	1E-4	1060

**Table 4.1** Summary of the evolution of relative deviation of absorption line area  $A_i$  and position  $\nu_i$  from the prescribed ‘true’ values together with the signal to noise ratio  $S/N_{3\sigma,i}$  for each iteration of the advanced integrative fit. The values are obtained for the simulated data shown in Figure 4.2 with equal terminating conditions.

The deviation of  $A_i$  from the actual value is independent of the strength of absorption, but mainly depends on the environmental conditions. For gas pressures well below atmospheric pressure,  $\gamma_V$  and therefore the deviation of  $A_1$  in the first iteration would be much smaller and an iterative procedure would most probably be unnecessary. However, for higher gas pressures the opposite would be the case. Table 4.1 also illustrates that after the last (sixth) iteration, the precision of the retrieved absorption line area  $A_6$  is better than  $10^{-3}$  which corresponds to the chosen terminating condition  $\varepsilon_A$  and is approved by a signal to noise ratio  $S/N_{3\sigma,i} > 1000$ . The same holds true for the absorption line position  $\nu_6$  which is retrieved with a precision of  $10^{-4}$  corresponding to the chosen terminating condition  $\varepsilon_\nu < 10^{-4}$ .

#### 4.2.2 Comparison with Levenberg–Marquardt fitting algorithm

A standard algorithm used for the fitting of nonlinear problems is the Levenberg–Marquardt algorithm (Marquardt, 1963; Press et al., 2007). For its application to the fitting of spectral line profiles see, e.g., (Ouyang and Varghese, 1989). It is a very powerful method, but some limitations apply. For initialization, the LM fit needs start values for all fit parameters which is a possible source of instability. If the initial values deviate too much from the actual solution, the LM fit possibly does not converge into this solution. When heavy signal variations are expected as in the case of combustion (Teichert et al., 2003) or airborne measurements (Gurlit et al., 2005; May, 1998), this could result in an possible destabilization of the LM algorithm as long as no additional method is used to obtain educated guesses for these initial values. However, such an additional method would come at the expense of additional computational complexity and lower speed. This complication does not apply for the AI fitting algorithm, since it does not need initial values for the fit parameters (line area, line position, and background polynomial coefficients), but is able to obtain appropriate fit values directly

from the measurement signal. The downhill simplex method (Nelder and Mead, 1965; Press et al., 2007) is another algorithm which does not depend on the choice of good initial values. However, its conversion speed is, in general, low.

An advantage of the LM fitting algorithm is that it is very flexible. For example, a fit to multiple absorption lines can easily be incorporated by extending the mathematical description of the problem. For the AI fitting algorithm this extension would be complex to implement at least without abandoning the entire independence of initial values for the fit parameters. Another advantage of the LM fitting algorithm over the AI fitting algorithm is that the absorption line width  $\gamma_V$  does not have to be precomputed, but can be a free fit parameter.

Besides robustness and flexibility, an aspect of great interest for fitting algorithms is computational speed. For the AI fitting algorithm, only the mathematical function describing the optimization problem has to be calculated for all data points. For the LM fitting algorithm, in addition, the partial derivatives with respect to all fit parameters are needed. This increases computational complexity and is expected to result in reduced computational speed compared to the AI fitting algorithm.

To verify this assumption, calculating times of both fitting algorithms were determined for simulated data with a number of 500 data points dependent on the number of fit parameters, which correspond to the degree of the background polynomial plus absorption line area and position. Background polynomials from zeroth to third degree and, in addition, different levels of uniform white noise were investigated. The amplitude of the uniform white noise signal added is defined as percentage of the maximum value of the absorption line profile. The spectral interval considered is  $1 \text{ cm}^{-1}$ , the absorption line position is slightly off-centered, and the line width  $\gamma_V$  is approximately  $0.1 \text{ cm}^{-1}$ . Note that the absorption line width is no free fit parameter in both fitting algorithms to ensure comparability of calculation speed. As mathematical representation for the absorption line shape, the analytical Voigt profile approximation  $\Phi_V$  from (2.18)-(2.20) was used (Whiting, 1968; Olivero and Longbothum, 1977). Both fitting algorithms were coded in C++ and compiled with the *Microsoft (R) 32-bit C/C++ Optimizing Compiler Version 16.00.30319.01 for 80x86*. The LM fitting algorithm is an optimized version of the one described in (Press et al., 2007). Major optimizations include that partial derivatives with respect to the background polynomial coefficients and the absorption line area are trivial in such a way that they only contain  $\Phi_V$  itself and no derivatives of  $\Phi_V$  because the problem is linear in these parameters. The line position is the only parameter which makes an explicit derivative of  $\Phi_V$  necessary. This derivative is evaluated analytically from (2.18).

The initial values for the fit parameters of the LM fitting algorithm are chosen in the following manner. The initial value for the absorption line position is given by the maximum of the absorption signal OD. All other initial values are randomly varied by a normal distribution around their true values with a standard deviation of 10% of the respective true value. Terminating conditions for both fitting algorithms are  $\varepsilon_V < 10^{-4}$  and  $\varepsilon_A < 10^{-3}$ , respectively. All

calculating times were obtained as an average of 1000 fit runs to obtain good statistics especially for the initial values of the fit parameters of the LM algorithm. Calculations were performed on an Intel Core 2 Quad Q6600 central processing unit (CPU) of which one core was used for calculations. Adaption of the fitting routines to multi-threading would be a possibility to further enhance calculation speed, but would presumably leave the difference in calculation speed between the AI and the LM fitting algorithm unchanged.

Results of the examination of calculation times are shown in Table 4.2. The AI fitting algorithm is able to fully evaluate an absorption line profile within a few hundred microseconds. Generally, calculation speed decreases with increasing number of fit parameters and noise level as expected. The AI fitting algorithm is more susceptible to noise than the LM algorithm. This results from the fact that a noisier signal makes the determination of the correct line position harder for the AI algorithm and therefore, in general, a higher number of iterations are necessary. However, even for noisy conditions a factor of approximately four in calculation speed is retained in favor of the AI algorithm. This factor increases to approximately five if noise levels are low.

Number of fit parameters	3	4	5	6
Background polynomial degree	0	1	2	3
AI fit without noise [ $\mu\text{s}$ ]	150	160	200	210
AI fit with 0.1% noise [ $\mu\text{s}$ ]	160	170	210	220
AI fit with 1% noise [ $\mu\text{s}$ ]	210	210	240	270
AI fit with 10% noise [ $\mu\text{s}$ ]	230	240	270	340
LM fit without noise [ $\mu\text{s}$ ]	820	830	890	960
LM fit with 0.1% noise [ $\mu\text{s}$ ]	830	860	910	970
LM fit with 1% noise [ $\mu\text{s}$ ]	860	890	930	1000
LM fit with 10% noise [ $\mu\text{s}$ ]	910	910	970	1230

**Table 4.2** Calculating times of the advanced integrative (AI) fitting algorithm compared to the Levenberg–Marquardt (LM) fitting algorithm for different numbers of fit parameters which correspond to different background polynomial degrees. Simulated data (500 data points) with different levels of uniform white noise are considered. Further details are given in the main text.

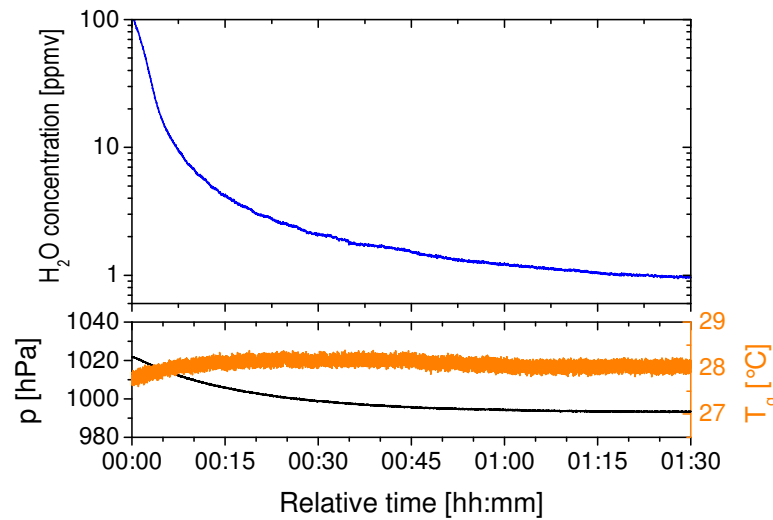


**Figure 4.3** Temporal evolution of absorber (water vapor) concentration data set used to compare the advanced integrative and Levenberg–Marquardt fitting algorithm accuracy. The continuous decrease of water vapor concentration was achieved by purging the measurement volume with dry synthetic air while gas pressure  $p$  and gas temperature  $T_g$  were kept nearly constant.

### 4.2.3 Application to experimental data

After the theoretical comparison between the AI and the LM fitting algorithms presented in the previous section, a comparison for experimental measurement data will be given here. Experimental data was obtained by means of direct TDLAS with the hygrometer APeT, described in detail in Chapter 5. Water vapor absorption line 000-101, 110-211 at 1370 nm, see Section 5.1, was used for the measurement. For data evaluation, the AI fitting algorithm, as described here, had to be adapted in such a way that the background correction does not take place in the domain of optical density, but in the intensity representation of the Beer–Lambert law (2.21). This adaption can be done with very little effort and does not affect the properties of the AI fit in any way.

Figure 4.3 shows the temporal evolution of the water vapor concentration. Approximately two orders of magnitude in water vapor concentration were covered by continuously purging the APeT instrument with dry synthetic air. Environmental conditions were nearly constant throughout the measurement with gas pressure  $p \sim 1000$  hPa and gas temperature  $T_g \sim 28$  °C.

For data evaluation, the polynomial background was taken to be of third order in the AI as well as the LM fitting algorithm. Figure 4.4 shows an example fit from both algorithms for one data sample out of the entire measurement data set given in Figure 4.3. Despite the low signal to noise ratio  $S/N_{3\sigma}$  of 15, the AI fitting algorithm is able to retain a good fit to the data. In comparison, the LM algorithm yields a somewhat better  $S/N_{3\sigma}$  of 19. This better

$S/N_{3\sigma}$  mainly results from the fact that the LM algorithm uses all data points for fitting the background polynomial whereas the AI algorithm only uses part of the data points. Therefore, the LM algorithm obtains a slightly better fit to the background polynomial. The relative deviation of the absorption line area retrieved by the AI algorithm compared to the LM algorithm is 6%. This deviation is covered by the uncertainty resulting from the low  $S/N_{3\sigma}$  as this uncertainty is given by the inverse of  $S/N_{3\sigma}$ .

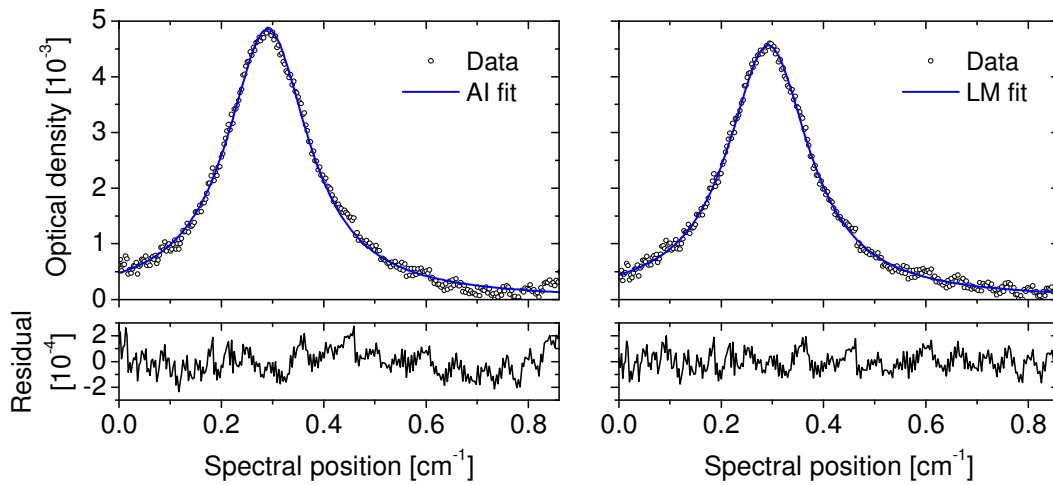


**Figure 4.4** Example of an advanced integrative and Levenberg–Marquardt absorption line fit to the same data sample obtained with direct tunable diode laser absorption spectroscopy. The data sample is part of the temporal evolution of the absorber concentration given in Figure 4.3. Polynomial background was assumed to be of third order, terminating conditions are the same as in the preceding sections. Signal to noise ratio  $S/N_{3\sigma}$  is 15 for the advanced integrative fit and a slightly better 19 for the Levenberg–Marquardt fit. The deviation of the line area obtained by both fitting methods is 6% which is covered by the uncertainty resulting from the signal to noise ratio.

Corresponding to the entire data set given in Figure 4.3, Figure 4.5 depicts the relative deviation of the absorption line area  $A$  retrieved by both fitting algorithms dependent on the signal to noise ratio  $S/N_{3\sigma}$ . A hyperbolic fit with fit function  $f(x) = a/x$  was performed to the data and yielded  $a = 0.76$  where  $a = 1$  would define the uncertainty resulting from  $S/N_{3\sigma}$ . The fit result shows that the relative deviation is lower than and therefore solely defined by the uncertainty given by  $S/N_{3\sigma}$ . This suggests that both fitting algorithms can be treated equivalently in terms of accuracy although the LM algorithm shows slight advantages in terms of better  $S/N_{3\sigma}$  over the AI algorithm for evaluation of the same data sample. Moreover, it suggests that intrinsic uncertainty of AI fit results is dominated by measurement signal noise.

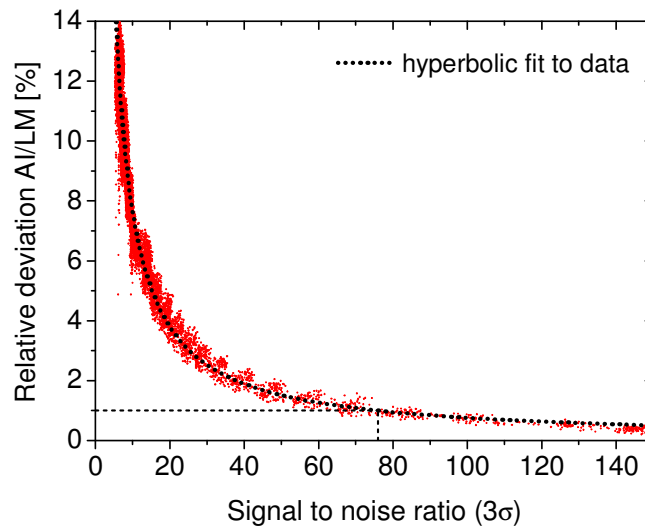


**Figure 4.5** Relative deviation of the absorption line area  $A$  obtained by the advanced integrative and the Levenberg–Marquardt fitting algorithm dependent on the signal to noise ratio  $S/N_{3\sigma}$ . The data set shown here corresponds to the temporal evolution of the absorber concentration given in Figure 4.3. A hyperbolic fit with fit function  $f(x) = a/x$  was applied to the data with  $a = 0.76$ . This fit yields that the relative deviation between both fitting algorithms falls, e.g., below 1% for an  $S/N_{3\sigma}$  greater than approximately 80 (dashed lines).

#### 4.2.4 Discussion of advantages and disadvantages

Compared to previous implementations of the integrative evaluation of absorption line profiles, the developed AI fitting algorithm shows clear advantages in terms accuracy. Previous implementations were limited to an accuracy of several percent for measurements under standard conditions (1 atm, 0 °C) due to their limited capabilities to correct for parts of an absorption line lying outside the spectral interval of the measurement or due to insufficient background correction. The AI fitting algorithm does not show such an intrinsic source of uncertainty. Uncertainties are dominated by measurement signal noise which has been shown by comparison of AI fit results with the results of a LM fitting algorithm. This comparison was only possible due to another advantage of the AI fitting algorithm. In contrast to previous implementations, it offers – with signal to noise ratio – a reliable quality indicator for the fit result.

Therefore, a direct comparison of the AI fitting algorithm with the universally applicable LM fitting algorithm seems to be more appropriate. Table 4.3 summarizes the advantages and disadvantages of both fitting methods. It is apparent that the AI fitting algorithm has advantages in the categories stability and speed which follow from intrinsic properties of the principle of integrative evaluation. In contrast to the LM fitting algorithm, the AI fitting algorithm is not dependent on an adequate choice of initial values for the fit parameters which

could lead to destabilization of the algorithm due to signal variations. This does not mean, however, that the AI fitting algorithm reasonably converges in any case. If the absorption line profile in the measurement signal is too badly defined or the absorption line moves too close to the borders or even out of the measurement interval, a satisfying convergence is not guaranteed. However, this holds for the LM fitting algorithm as well. In favor of the LM fitting algorithm, its higher flexibility can be stated because it is easily extended to more general problems beyond the evaluation of single absorption line profiles with precomputed line width  $\gamma_V$  to which the AI algorithm is restricted.

	AI fitting algorithm	LM fitting algorithm
<b>Stability</b>	<ul style="list-style-type: none"> <li>no initial values for fit parameters necessary</li> <li>no destabilization due to signal variation</li> </ul>	<ul style="list-style-type: none"> <li>initial values for fit parameters necessary</li> <li>possible destabilization due to signal variation</li> </ul>
<b>Speed</b>	AI fitting algorithm a factor 4-5 faster than LM fitting algorithm	
<b>Flexibility</b>	<ul style="list-style-type: none"> <li>Multi absorption-line fit complicated to implement</li> <li>Absorption line width has to be prescribed</li> </ul>	<ul style="list-style-type: none"> <li>Multi absorption-line fit easy to implement</li> <li>Absorption line width can be free fit parameter</li> </ul>

**Table 4.3** Summary of the advantages and disadvantages of the advanced integrative (AI) fitting algorithm compared to the Levenberg–Marquardt (LM) fitting algorithm.

Whether the restriction to a single absorption line is acceptable mainly depends on the measurement application. For a species like water vapor, sufficiently isolated absorption lines can be found which yield excellent retrieval of gas concentrations without need for further corrections. The water vapor absorption line 000-101, 110-211 with impact on line area from adjacent absorption lines summing up to 0.2% (see Section 5.1) is a good example. Prescription of the absorption line width  $\gamma_V$  can be a problem if the spectral parameters of an absorption line are not well-known. In this case, the LM fitting algorithm with the possibility of letting  $\gamma_V$  be a free fit parameter is in advantage, but also for the LM algorithm, a precomputed  $\gamma_V$  can be of great benefit to increase fit stability. The mentioned limitations of the AI fitting algorithm could be addressed in future work. Such an extension of the AI fitting algorithm would be, however, complicated and impact on the robustness of the algorithm is unclear.

The properties discussed make the AI fitting algorithm the ideal choice if stability and speed are crucial in an application, but restricting to a single absorption line with precomputed width  $\gamma_V$  is possible. Potential application areas include atmospheric measurements, aircraft

and balloon based, as well as measurements in combustion environments for which fit stability and high time resolutions are essential. An application of the AI fitting algorithm could be in particular favorable for embedded systems with limited computing power if high compactness and low power consumption are a crucial factor.

At the cloud chamber AIDA, large measurement signal variations caused by transmission losses during periods of dense clouds are not unusual, neither is nonstop measurement operation for more than 24 hours. Both conditions do not impose a problem for the AI fitting algorithm. Thus, the AI algorithm is used as fast, reliable, and accurate online data evaluation of the AIDA in and ex situ TDL hygrometer measurements which will be described in detail in the following chapter.

## Chapter 5

# Tunable diode laser hygrometers at AIDA

Humidity is a crucial quantity for the investigation of aerosol-cloud interactions and ice nucleation capabilities of different aerosol types. As these processes are studied at the AIDA cloud chamber (cf. Chapter 3) in dynamic cloud expansion experiments for a wide range of different temperatures and thus humidity levels, humidity measurement techniques have to fulfill high demands in accuracy of few percent as well as time resolution of equal or less than one second. Moreover, a high dynamic range of several orders of magnitude has to be covered.

These demands make hygrometers based on direct TDLAS (tunable diode laser absorption spectroscopy, cf. Section 2.3) the ideal choice for humidity measurements at AIDA. Direct TDLAS is able to yield both high time resolution due to fast measurement repetition rates as well as high accuracy due to its inherent property of self-calibration. Self-calibration implies that the measurement accuracy of a hygrometer based on direct TDLAS can be quantified for a defined range of measurement conditions without any specific and active calibration measures against a calibration standard.

Three TDL (tunable diode laser) hygrometers based on direct TDLAS are in operation at AIDA at the moment. Two of them, APicT (AIDA PCI in cloud TDL) and the newly developed SP-APicT (SP stands for ‘single path’) complementary measure AIDA in situ water vapor concentrations whereas APeT (AIDA PCI extractive TDL) is able to measure AIDA total water content extractively. This combination of total water and water vapor measurement allows the deduction of ice or liquid water content in AIDA with high accuracy and time resolution.

A description and improvements of the AIDA TDL hygrometers as well as new developments will be given in Section 5.2. The performance of the instruments will be assessed in Section 5.3 especially under the aspect of measurement accuracy and its validation. As this aspect of measurement accuracy is of such importance a discussion of sources of measurement uncertainty regarding the AIDA TDL hygrometers will be given in the following.

## 5.1 Sources of measurement uncertainty

Direct TDLAS is often referred to as self-calibrating (or calibration-free), since the Beer–Lambert law (2.21) can directly be applied to measurement data evaluation for the retrieval of absorber concentrations – in contrast to other TDLAS techniques such as wavelength modulation spectroscopy (WMS; Werle et al., 2002). Due to scanning over a single absorption line, signal perturbations like scattering losses caused by aerosol particles or cloud droplets and background effects can be corrected for by application of the extended Beer–Lambert law (2.30). Moreover, the spectral properties of the absorber, absorption line strength and shape, depend only on gas pressure and temperature and are well described by theoretical line shape models such as the Voigt absorption line profile (cf. Section 2.2.4).

Looking closer at the Beer–Lambert law (2.30) reveals several sources of uncertainty that have impact on the measurement accuracy of direct TDLAS. According to a study performed by (Hunsmann et al., 2006) which directly applies to water vapor measurements at the AIDA chamber, accuracy is mainly limited by the uncertainty of the temperature dependent strength  $S(T)$  of the absorption line used for TDLAS measurements. Figure 5.1 shows absorption lines at a wavelength near 1370 nm of which the absorption line 000-101, 110-211 is used at present for AIDA measurements. The magnitude of  $S(T)$  of this absorption line could be constrained experimentally within 3% (Hunsmann et al., 2006). The second most important source of uncertainty arises from the absorption path length  $L$ . For the AIDA TDL hygrometers, the accuracy of  $L$  is estimated to be 1-2%. For APeT, the path length was verified within 2% by a methane validation measurement at a defined methane concentration (Lauer, 2007). For APicT and SP-APicT, it is estimated that thermal effects causing warping of the AIDA chamber wall can lead to an uncertainty of the order of 1% in  $L$ .

Further, but minor sources of uncertainty originate from insufficient representation of the absorption line shape by a Voigt profile (Ebert and Wolfrum, 2001), from uncertainty in the dynamic tuning behavior  $dv/dt$  of the diode laser used for the measurement, or from the accuracy of pressure and temperature values used for the retrieval of water vapor concentration  $c_{\text{H}_2\text{O}}$ . The total of these minor contributions is typically of the order of 1%, cf. (Hunsmann et al., 2006), with one exception.

According to HITRAN 2008 (Rothman et al., 2009), the self broadening coefficient  $\gamma_{C,\text{self}}$  of the absorption line 000-101, 110-211 is approximately five times larger than the air broadening coefficient  $\gamma_{C,\text{air}}$ . (see Section 2.2.3 for a definition of the broadening coefficients). Although the value of  $\gamma_{C,\text{self}}$  has an accuracy of 5-10% according to HITRAN 2008, there is indication from own measurements that the HITRAN value is up to a factor of two too low. Note that  $\gamma_{C,\text{self}}$  for 000-101, 110-211 in HITRAN has not been retrieved by measurement, but is an interpolated value (Toth, 2005a, b). The resulting uncertainty of absorption line

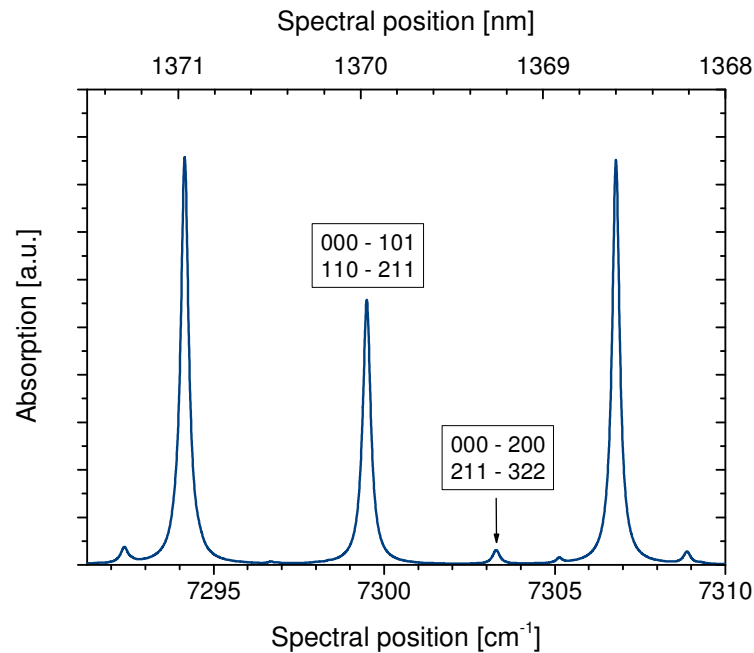


**Figure 5.1** Water vapor absorption lines near 1370 nm for a gas pressure of 1013.25 hPa. The spectral data are based on HITRAN 2008 (Rothman et al., 2009). For AIDA measurements, only absorption line 000-101, 110-211 is used at present while previously the weaker absorption line 000-200, 211-322 was used in addition for high water vapor concentrations.

width translates into potential uncertainty of line area in measurement data evaluation and therefore into uncertainty of water vapor concentration. Self broadening starts to become significant by contributing 2% to the total line width for water vapor concentrations above 4000 ppmv (as long as collision broadening is the dominant broadening mechanism). At this concentration, it is therefore expected that self broadening imposes an additional uncertainty on water vapor concentration of 1-2% which further rises with additional increase of humidity.

Summing up the spectroscopic uncertainties besides that discussed in the last paragraph one arrives at a measurement accuracy of approximately 5% for retrieved water vapor concentration (or equivalently water vapor partial pressure). This estimated accuracy could be confirmed during the AquaVIT intercomparison campaign at AIDA in 2007 (Ebert et al., unpublished; Fahey et al., 2009). In situ measurements of APicT in the temperature range 185-243 K were compared to water vapor saturation pressures over ice during periods of water vapor saturation inside the chamber, i.e. relative humidity  $RH_{ice} = 100\%$ , and deviations of  $\pm 3\%$  at maximum were found.

Besides the spectroscopic uncertainty, two additional factors can degrade measurement accuracy. The first is cross interference from absorption lines which are directly adjacent to the measurement absorption line and covered by the spectral interval of the measurement. For the

$\nu_0$ [ $\text{cm}^{-1}$ ]	Quantum numbers	$S(T_0)$ [ $\text{cm} \cdot \text{molec.}^{-1}$ ]	$\delta S(T_0)$ [%]
7299.43	000-101, 110-211	1.005E-20	–
7298.69	000-101, 1038-1037	1.299E-23	0.1
7299.54	000-200, 1029-1038	7.867E-24	0.1
7299.81	000-021, 1165-1266	2.098E-25	0.002

**Table 5.1** Absorption line 000-101, 110-211 together with directly adjacent water vapor absorption lines that are covered by the usual diode laser measurement scan range of approximately  $1.5 \text{ cm}^{-1}$ .  $\nu_0$  indicates the absorption line position, adjacent lines are sorted by line strength  $S(T_0 = 296 \text{ K})$  and relative line strength  $\delta S(T_0)$  with respect to absorption line 000-101, 110-211 as a measure for cross interference. Total cross interference on absorption line 000-101, 110-211 from adjacent lines sums up to approximately 0.2%. Contributions from other absorber species typically present in air are below 0.01%. The spectral line data are based on HITRAN 2008 (Rothman et al., 2009).

standard AIDA absorption line 000-101, 110-211, cross interference effects are very low and sum up to 0.2%, see Table 5.1. In Figure 5.2, a close up of absorption line 000-200, 211-322 is depicted which is more than a factor of ten weaker than standard absorption line 000-101, 110-211. This weak absorption line was used for high water vapor concentrations at temperatures above  $-15 \text{ }^\circ\text{C}$  prior to the development of SP-APicT. Under these conditions, standard absorption line 000-101, 110-211 would cause saturation in APicT measurements. However, absorption line 000-200, 211-322 suffers strongly from cross interference effects caused by adjacent water vapor lines which are included in the measurement scan range of the diode laser. This factor is illustrated in Table 5.2 which shows that total cross interference on absorption line 000-200, 211-322 sums up to approximately 8%. This value can be taken as measure for the additional measurement uncertainty when using this absorption line, since correction of the cross-interference effects during data evaluation is complicated. Trying to subtract the interfering absorption lines by fitting procedures turns out to be difficult as these absorption lines are not well characterized in the absorption measurement signal due to their relative weakness.

The second additional source of measurement uncertainty results from parasitic absorption of water vapor outside the measurement volume. This can be caused by optics parts, e.g. coupling optics, but also residual water vapor inside the package of the diode lasers can, under very dry measurement conditions, significantly add to the observed amount of absorption.

In the following section, the avoidance or characterization, respectively, of both additional sources of measurement uncertainty discussed above will be laid out. The avoidance of cross interference was, besides other benefits, a key priority in the development of SP-APicT. The issue of parasitic absorption was also directly incorporated into the development of SP-APicT and was addressed in improvements of APicT and APeT as well. Moreover, the characterization of residual laser water vapor absorption could significantly increase measurement accuracy under conditions of very low water vapor concentrations  $c_{\text{H}_2\text{O}} \lesssim 1 \text{ ppmv}$ .

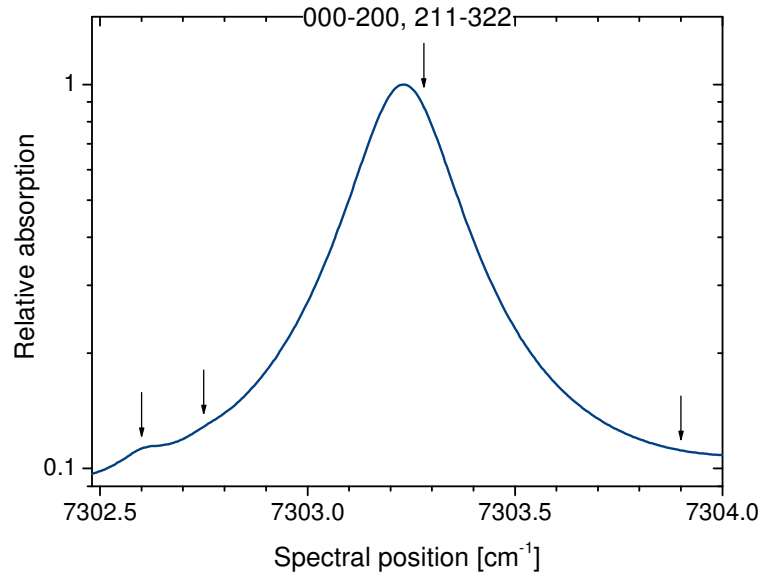


**Figure 5.2** Close up of absorption line 000-200, 211-322 for a gas pressure of 1013.25 hPa based on data from HITRAN 2008 (Rothman et al., 2009). The arrows indicate directly adjacent water vapor absorption lines which are covered by the usual diode laser measurement scan range of approximately  $1.5 \text{ cm}^{-1}$ . The spectral data of these absorption lines are given in Table 5.2.

$\nu_0$ [ $\text{cm}^{-1}$ ]	Quantum numbers	$S(T_0)$ [ $\text{cm} \cdot \text{molec.}^{-1}$ ]	$\delta S(T_0)$ [%]
7303.23	000-200, 211-322	8.028E-22	—
7302.60	000-200, 752-761	4.599E-23	5.7
7302.75	000-200, 753-762	1.521E-23	1.9
7303.90	000-200, 963-972	4.317E-24	0.5
7303.28	000-002, 744-735	2.118E-24	0.3

**Table 5.2** Absorption line 000-200, 211-322 together with directly adjacent water vapor absorption lines that are covered by the usual diode laser measurement scan range of approximately  $1.5 \text{ cm}^{-1}$ . Labeling corresponds to Table 5.1. Total cross interference on absorption line 000-200, 211-322 from adjacent lines sums up to approximately 8%. The spectral line data are based on HITRAN 2008 (Rothman et al., 2009).

## 5.2 Improvements and new developments

The instrumental improvement of the AIDA TDL hygrometers APicT and APeT as well as the development of the novel SP-APicT will be laid out in this section. Besides other benefits like increase of instrumental sensitivity, focus was put to address the sources of measurement uncertainty discussed in Section 5.1. The results of this effort will be summarized in the end of this section. In the following, a short overview of the AIDA TDL hygrometers and their common instrumental setup will be given followed by a detailed individual description of every TDL hygrometer.

### 5.2.1 Instrumental overview

Three TDL hygrometers are currently in operation at the cloud chamber AIDA. Two of them, APicT and SP-APicT, measure water vapor concentrations in situ, i.e. directly inside AIDA, while APeT measures total water concentrations by extractive sampling of AIDA gas. Technical details about all three instruments will be given in the following subsections, but a short overview will be given here.

An overview of applications and optical path lengths of APicT, SP-APicT, and APeT is given in Table 5.3. APicT, a well proven instrument (Giesemann, 2003; Ebert et al., 2005), is based around an optical multipath cell of White type (White, 1942) which allows for adjustment of optical path length between approximately 24 and 100 meters. These long absorption path lengths make it the ideal choice for lower water vapor concentrations at temperatures below  $-30$  °C. For warmer temperatures, the newly developed SP-APicT, which has a much shorter optical path of one time the diameter of AIDA, accompanies APicT and allows measurements at six times higher water vapor concentrations and in by a factor of six denser clouds. Parallel operation of APicT and SP-APicT, which share the same diode laser as light source, also allows for validation of self-calibration of direct TDLAS (see Section 5.3.4).

	<b>Optical path</b>	<b>Application</b>
APicT	23.6-99.8 m	Water vapor; cold clouds
SP-APicT	4.1 m	Water vapor; warm, dense clouds
APeT	30.3 m	Total water
APeT-APicT	–	Ice/liquid water content

**Table 5.3** Overview of optical path lengths and applications of the AIDA TDL hygrometers.

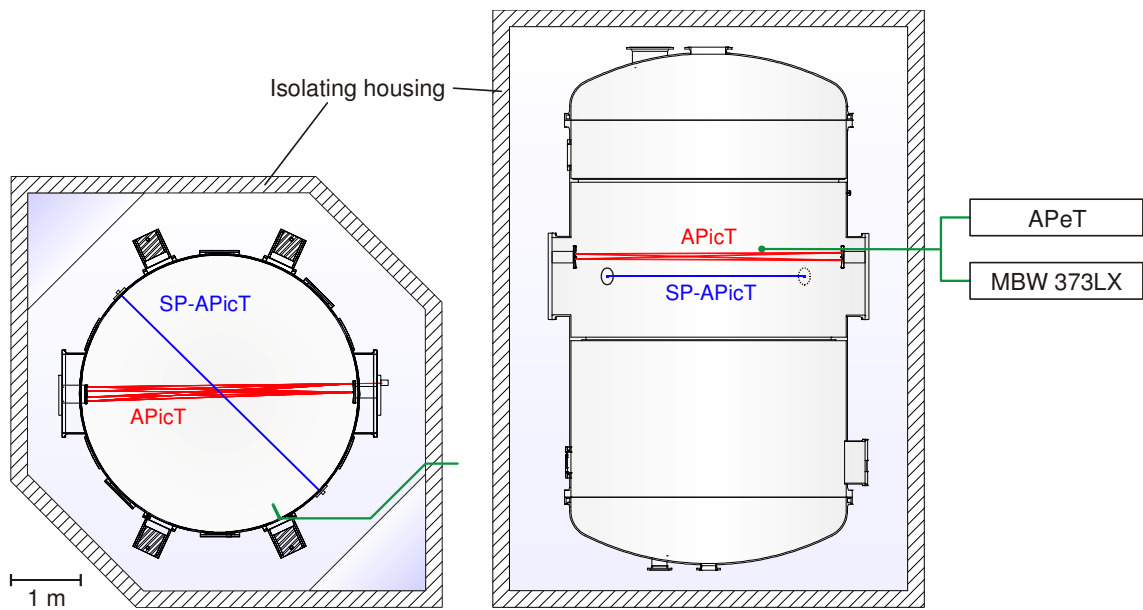


**Figure 5.3** Cross and longitudinal section of the AIDA chamber with depicted positions of the installed tunable diode laser (TDL) hygrometers. Two hygrometers, APicT and SP-APicT, have their total optical paths inside the chamber, in order to measure water vapor concentrations in situ. The optical path of APicT (red) is folded due to coupling into a multipath White cell. For SP-APicT, the optical path (blue) corresponds to approximately one time the diameter of the chamber. Both instrument's optical paths are located approximately at the same level, a little above half the chamber's height, with the path of SP-APicT lying  $\sim 40$  cm beneath that of APicT. The extractive TDL hygrometer APeT is positioned outside the isolating housing of the AIDA chamber in laboratory environment. A heated stainless steel sampling line (green) conveys AIDA gas to the instrument for the measurement of total water concentration. Its heated sampling probe inside AIDA is located at the same height as the measurement path of APicT. Besides APeT, a chilled-mirror frost point hygrometer (MBW 373LX) is connected to this sampling line.

For extractive measurement of total water, APeT has been developed (Lauer, 2007). It is based on an optical multipath cell of Herriott type (Herriott et al., 1964) and allows, together with the in situ TDL hygrometers, the deduction of ice or liquid water content (IWC/LWC) in AIDA by taking the difference between extractive total water and in situ water vapor concentration. The accuracy of the TDL IWC could be verified within this work for the first time (Section 5.3.5).

Figure 5.3 shows the position of the optical measurement paths of APicT and SP-APicT within the AIDA chamber. Both instrument's paths lie approximately at the same level (vertical separation  $\sim 40$  cm), a little above half the chamber's height and are horizontally shifted by an angle of  $45^\circ$  with respect to each other. The heated sampling probe of APeT is located at the same height as the APicT measurement path, but horizontally shifted by an angle of  $60^\circ$ . From this probe, sampling gas is conveyed through a heated stainless steel line (diameter 10 mm, length  $\sim 10$  m) to APeT which is positioned outside the isolating housing of the AIDA chamber in laboratory environment. The sampling probe and stainless steel line are

kept at a temperature of approximately 30 °C. All condensed water content is evaporated in the sampling line and APeT measures total water in gaseous form. At the same sampling line, a chilled-mirror frost point hygrometer (FPH, MBW 373LX, see Section 3.1) is installed and allows direct comparison with the measurement results of APeT.

### 5.2.2 Common instrumental setup and data evaluation

The principal instrumental setup is common for all three AIDA TDL hygrometers APicT, SP-APicT, and APeT. It is therefore briefly pointed out in the following and illustrated in Figure 5.4.

The core component of the TDL hygrometers is a fiber coupled DFB diode laser with a nominal wavelength of 1370 nm (NTT Electronics, NLK1354STB). Laser temperature can be adjusted with a dedicated Peltier element. A laser driver (Thorlabs, Pro8000) regulates laser current and temperature with integrated modules (Thorlabs, LDC8002 and TED8020). Laser current is modulated by a triangular waveform with a frequency of 139.8 Hz which is supplied by a function generator (Stanford Research Systems, DS345). This laser current modulation results in the wavelength tuning of the laser diode. In addition to the modulation signal, the function generator provides trigger signals for timing of data acquisition.

The emitted laser light is guided to the vacuum sealed measurement volume by a single mode optical fiber (Corning, SMF-28) with angled fiber end surfaces (FC/APC) to minimize back reflection and optical interference. The optical fiber enters the measurement volume via an optical feedthrough (VACOM, KF16-FCAPC-09-1-DE-ZR), laser radiation exits the fiber and is guided via individual optics to an InGaAs photodiode (Hamamatsu, G8370 series with peak sensitivity wavelength at 1.55  $\mu\text{m}$ ) serving as signal detector. This setup allows that the entire optical absorption path lies within the measurement volume and parasitic absorption of water vapor outside the measurement volume can be reduced to a minimum.

The detector signal exits the vacuum sealed measurement volume via an electric feedthrough (VACOM, KF16-BNC-SFL-DE-CE-SS) and is preamplified by a current amplifier (FEMTO Messtechnik, DLPCA-200). The signal detector data is acquired and digitized by an analog digital converter card with 18 bit resolution (National Instruments, NI PCI-6281). Sampling rate is typically chosen in such a way that one measurement scan period consists of 1000 data points. This results in a sampling rate of 139.8 kHz. Gas pressure and temperature signals are directly taken from AIDA sensors for APicT and SP-APicT while APeT has its own pressure and temperature sensors.

Data evaluation and storage takes place on a standard personal computer by means of a custom software (Wagner, 2005, 2011) coded in LabVIEW (National Instruments). For online data evaluation of the absorption signal, the advanced integrative fitting algorithm described in Chapter 4 is used while for final data evaluation an adapted Levenberg–Marquardt fitting

algorithm is applied (Fernholz, 2001). During data evaluation, a Voigt profile as described by Equations (2.18)-(2.20) in Section 2.2.4 (Whiting, 1968; Olivero and Longbothum, 1977) is fitted to the absorption signal where collision broadening width  $\gamma_C$  and Doppler broadening width  $\gamma_D$  are calculated from measured gas pressure and temperature data. Spectral parameters for the measurement absorption line 000-101, 110-211 are taken from the HITRAN 2008 database (Rothman et al., 2009) except air broadening coefficient  $\gamma_{C,\text{air}}$  and temperature coefficient  $n_C$  of collision broadening. These have been determined more precisely in (Hunsmann et al., 2006) to  $\gamma_{C,\text{air}} = 0.0981 \pm 0.0002 \text{ cm}^{-1}/\text{atm}$  and  $n_C = 0.74 \pm 0.01$ .

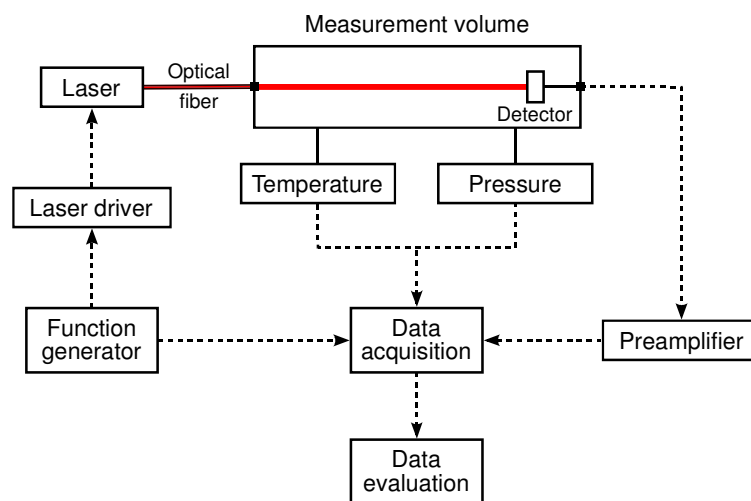


**Figure 5.4** Basic instrumental setup common for the AIDA tunable diode laser hygrometers. Arrows indicate signal flow, propagation of laser radiation is shown in red. Note that the entire optical absorption path lies inside the vacuum sealed measurement volume to minimize effects of parasitic absorption caused by water vapor outside the measurement volume.

### 5.2.3 APicT: long path in situ hygrometer

Of all AIDA TDL hygrometers, APicT has been in operation for the longest time (Giesemann, 2003; Ebert, 2003; Ebert et al., 2005). It was developed to measure dynamic water vapor concentrations in situ in the AIDA chamber for which its absorption measurement path is folded several times inside an optical multipath cell of White type (White, 1942) with a base length of 3.74 m (Ebert et al., 2005). The mirrors of the White cell can be adjusted by stepper motors. This optical setup allows that APicT has an alterable absorption path length of 23.6-99.8 m. Figure 5.5 shows the White cell field mirror and objective mirror optics inside the AIDA chamber where all mirrors are supplied with heating foils on the back to prevent mirror fogging. The field mirror is  $25 \times 16 \text{ cm}^2$  in dimension and the objective mirrors have a

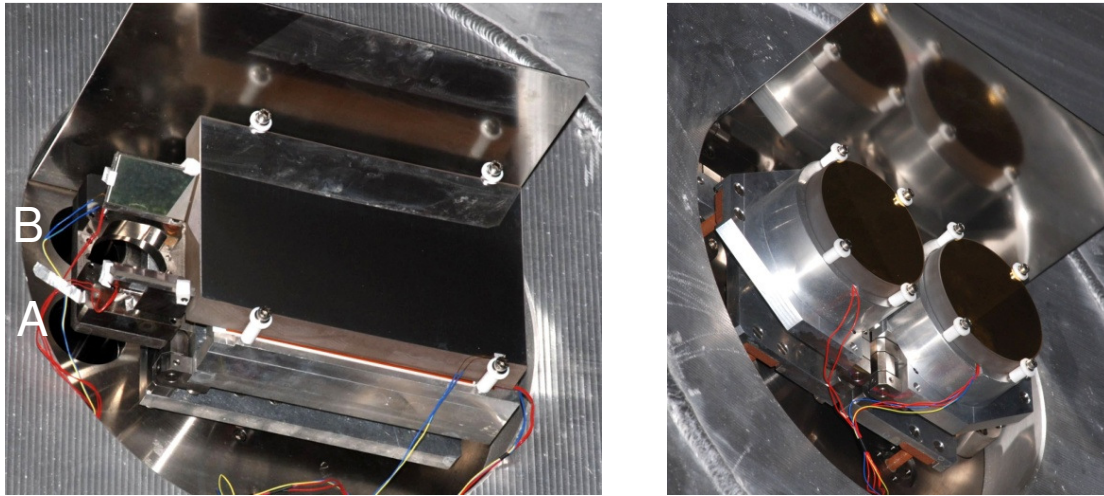


**Figure 5.5** White cell optics with field mirror (left) and objective mirrors (right) mounted at the inside of the AIDA chamber wall. ‘A’ and ‘B’ indicate flanges in the AIDA wall through which laser light is coupled into and out of the White cell. Coupling optics is attached to these flanges from the outside of the chamber wall. Cabling belongs to heating of the White cell mirrors.

diameter of 12 cm. All mirrors are spherical and their radius of curvature equals the base length of the White cell. Laser light is coupled into and out of the White cell through flanges in the AIDA wall next to the field mirror. Coupling optics is attached to these flanges from the outer side of the AIDA wall.

Since APicT has been in operation for almost a decade, it is a mature instrument and improvements of its setup during this work concentrated on advances in measurement accuracy and sensitivity. For this reason, the coupling optics section was entirely redesigned. Previous coupling optics was mounted open on an optical plate attached to the outside of the AIDA wall in the intermediate cold section between the AIDA wall and the isolating housing and coupled into the chamber through optical windows (Giesemann, 2003). This led to an external absorption path of 40 cm outside AIDA which corresponds to a fraction of up to 2% of the total absorption path length. Since humidity conditions in the intermediate cold section approximately correspond to saturation with respect to AIDA wall temperature, the path fraction of 2% directly translates into potential systematic measurement offset in the retrieval of water vapor concentration, especially if humidity conditions inside AIDA change dynamically during expansion experiments. This systematic offset had to be corrected for. However, as humidity conditions in the intermediate cold section are only approximately known, this correction is rather inaccurate.

Figure 5.6 depicts the redesigned APicT coupling optics. It is entirely integrated in Klein flange components (DN40KF) which are attached to the AIDA wall. Therefore, the coupling optics section is directly connected to the AIDA inner volume and the entire absorption path

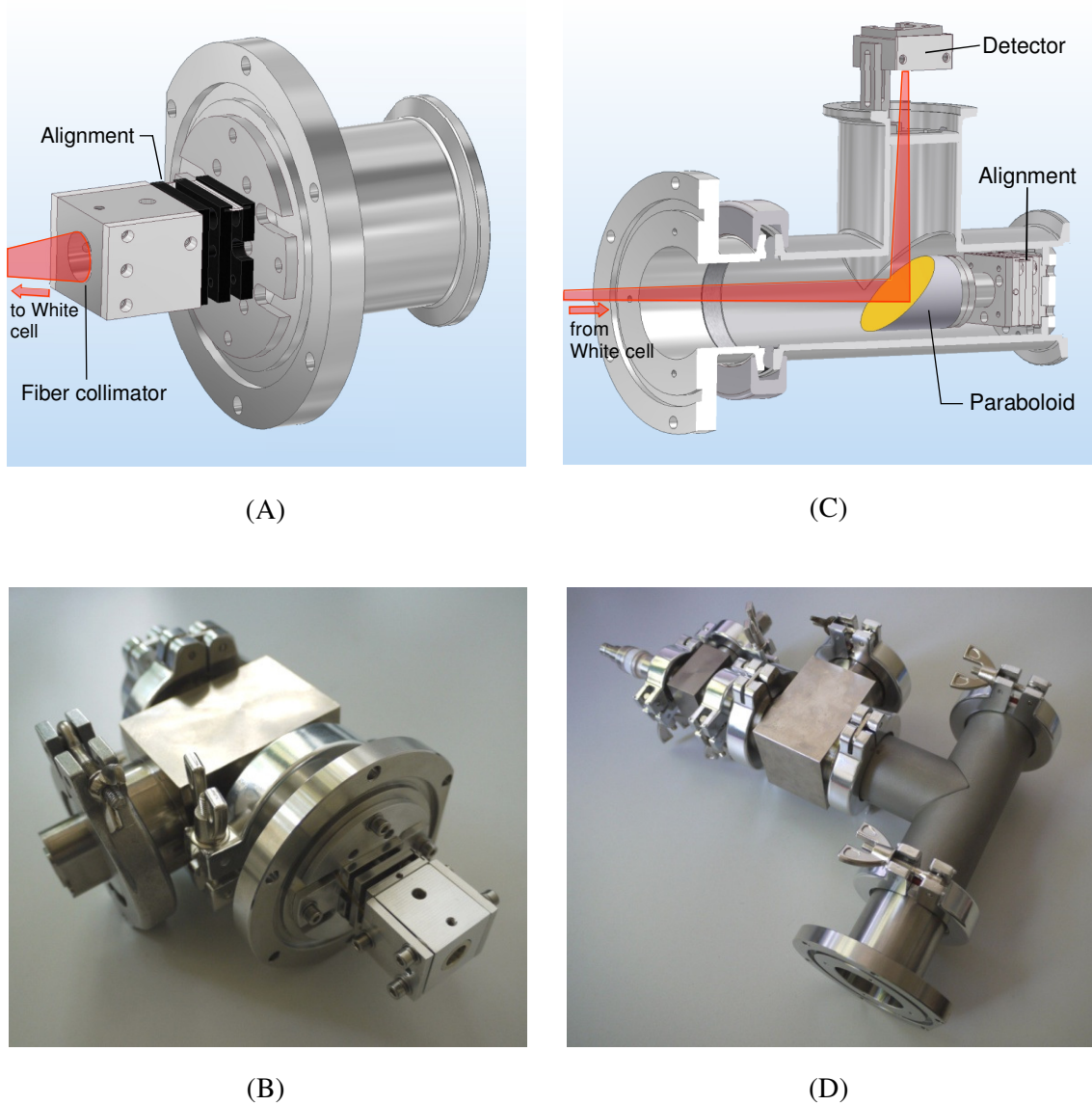


**Figure 5.6** Newly designed APicT coupling optics. Panels on left hand side show the fiber-coupled optics on laser side for coupling into the White cell, technical drawing (A) and realization (B), while panels on right hand side show the detector side for coupling out of the multi path cell, technical drawing (C) and realization (D). Laser beam light is indicated in red. Note that the entire optics is integrated in Klein flange vacuum components (DN40KF) that are directly attached to the AIDA chamber which allows the entire absorption path to be inside AIDA.

length lies inside AIDA which minimizes influence of parasitic water vapor absorption outside the measurement volume. Moreover, this design makes coupling windows obsolete which reduces interference effects that can degrade optical sensitivity of the instrument.

The fiber coupled optics on laser side uses a lens collimator with a focal length of 11 mm (Schäfter+Kirchhoff, 60FC-4-A11-03). This collimator allows an intermediate focal point of the laser light in the plane of the White cell field mirror in connection with a wide illumination (~5 cm spot diameter) of the objective mirrors. For beam alignment, the fiber collimator is attached to an optical flexure mount (Newport, MFM-50). This type of flexure mount has turned out to be very reliable and stable due to the absence of springs as used in conventional optical mounts.

The detector side where the absorption signal is received after exiting the White cell consists of an off-axis paraboloid (Janos, A8037-106, surface gold coating, 25.4 mm diameter, 76.2 mm focal length, 90° deflection angle), which sits on an identical flexure mount as for alignment of the laser side and focuses on the signal detector (Hamamatsu, G8370-02, diameter 2 mm). The signal detector is placed inside a custom made receptacle, tilted slightly with respect to the optical axis to avoid signal degrading etalon interferences. All optical components have polyimide heating foils installed to prevent fogging and foil thermometers (Pt100) for temperature control. Heating foils and foil thermometers are available from Telemeter Electronic. All optical and electric signals enter the vacuum components surrounding the optics via vacuum feedthroughs available from VACOM.

As written before, the optical redesign of APicT is expected to improve measurement accuracy by up to 2% without the need for according corrective measures in measurement data evaluation. Furthermore, measurement sensitivity is expected to increase significantly by avoidance of degrading interference effects. These two aspects as well as validation of the accuracy of APicT will be discussed in Section 5.3.

#### **5.2.4 SP-APicT: novel short path in situ hygrometer**

As discussed in Section 5.1, APicT had to be switched to a weaker absorption line for high water vapor concentrations at warm temperatures above  $-15\text{ }^{\circ}\text{C}$  due to saturation of the absorption line signal when using the standard measurement absorption line. However, this switch of the absorption line can decrease measurement accuracy by up to eight percent due to cross interference of adjacent absorption lines, since corrective measures in measurement data evaluation are difficult. Moreover, clouds that form in the AIDA chamber at these warm temperatures are very dense and APicT signal transmission suffers badly from scattering losses. As the temperature range above  $-15\text{ }^{\circ}\text{C}$  is important for the investigation of ice nucleation ability of, e.g., biogenic aerosol (Möhler et al., 2008), the above mentioned issues have been addressed by the development of the novel SP-APicT.

SP-APicT uses one time the diameter of the AIDA chamber as optical absorption path which results in almost a factor of six lower absorption path length compared to the minimal path length of APicT. This translates into a factor six higher upper limit of dynamic range (see Section 5.3.3). Moreover, scattering losses are significantly reduced whereas optical stability is improved in such a way that realignment of the SP-APicT optics is unnecessary after initial alignment (see Section 5.3.2).

SP-APicT shares with APicT the same diode laser as measurement light source which allows direct comparability of the results of both instruments. The optical design of SP-APicT is aimed to avoid, like for APicT, parasitic absorption of water vapor from outside the measurement volume, but in contrast to APicT also avoids optical parts which are attached from the outside to the AIDA chamber wall. The optical path within these attachments would make up for 10% or more of the entire optical path and humidity conditions inside the attachments could not be representative for humidity conditions in the main volume of AIDA. Therefore, the collimating and focusing optics of SP-APicT are directly attached to the inner side of two opposite blind flanges with 20 cm nominal diameter (DN200 PN10) which are mounted flush with the AIDA wall.

Optical setup of SP-APicT is depicted in Figure 5.7. The fiber coupled laser side and the detector side of the optics are identical in their basic construction that consists of a Microbench (Qioptiq Photonics) cube in which an off-axis paraboloid (Janos, A8037-106, surface gold coating, 25.4 mm diameter, 76.2 mm focal length, 90° deflection angle) is mounted. On laser side, the paraboloid is used for collimating the laser beam exiting the optical fiber, whereas on detector side, it focuses the beam on the signal detector. The cube is attached to flexure mounts (Newport, MFM-100) to allow alignment of the laser beam and alignment of focal point, respectively. The output facet of the optical fiber is mounted in an xy fiber positioner (Qioptiq Photonics, G067-021-000) which is connected to the Microbench cube by four rods 75 mm in length. In combination with the paraboloid, this results in a collimated beam traversing the AIDA chamber with a diameter of approximately 2 cm which prevents that individual particles, e.g. large ice crystals with sizes of up to 200  $\mu\text{m}$ , in the absorption path can have significant effect on SP-APicT signal strength and quality.

Correspondingly on the detector side, the signal detector (Hamamatsu, G8370-01, diameter 1 mm) is placed inside a custom made receptacle. It is mounted with a slight tilt with respect to the optical axis in order to avoid etalon interferences that would degrade absorption signal quality. As for APicT, all optical components can be heated by polyimide heating foils, their temperatures can be monitored by foil thermometers, and all optical and electric signals enter the interior of AIDA via vacuum feedthroughs available from VACOM.

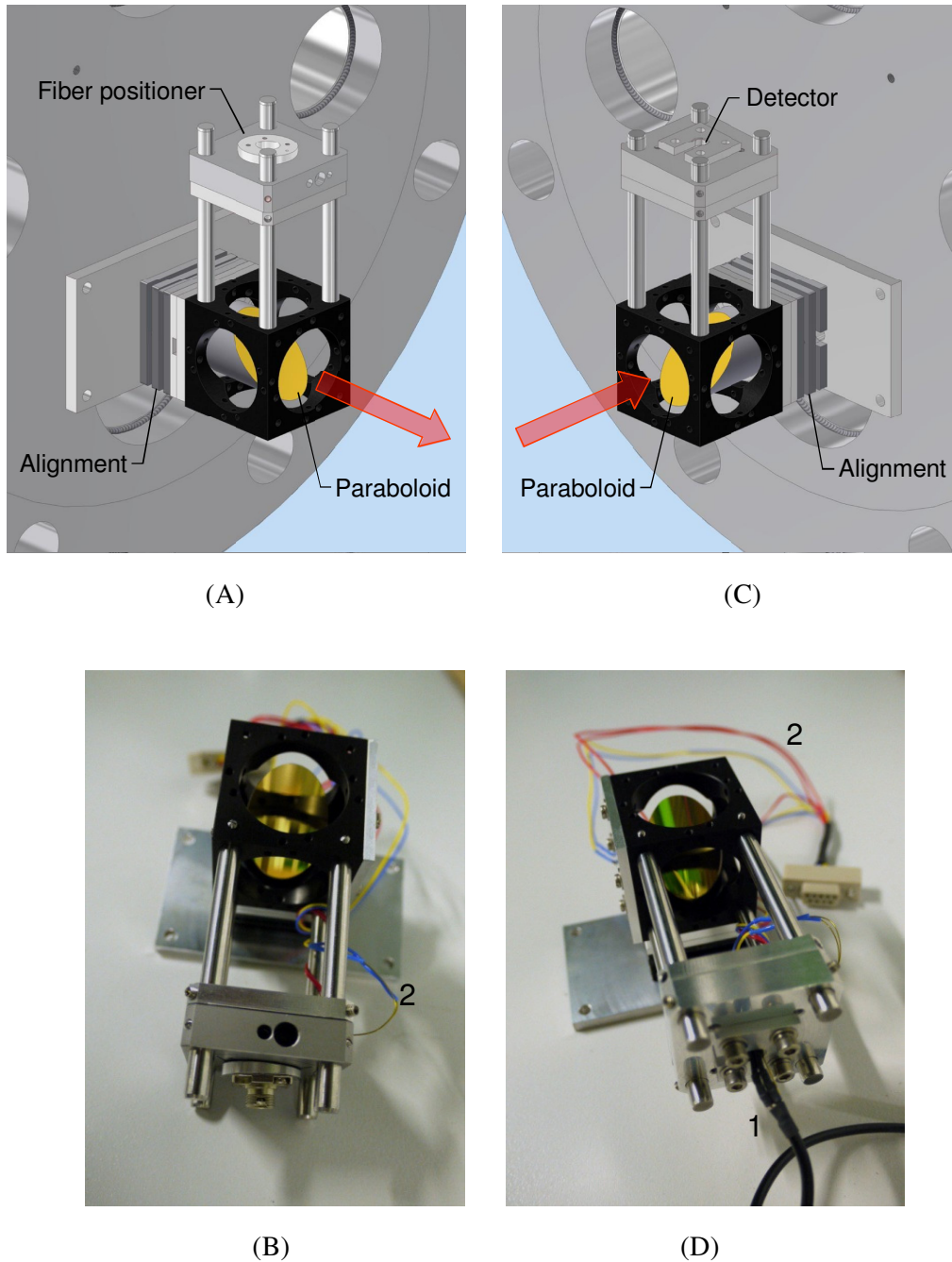


**Figure 5.7** Optics of the newly developed SP-APicT. Panels on left hand side show the fiber-coupled collimating optics on laser side, technical drawing (A) and realization (B), while panels on right hand side show the focusing optics on detector side, technical drawing (C) and realization (D). Red arrows indicate the direction of the collimated laser beam traversing one time the AIDA chamber. Optics is attached on the inner side of a blind flange (DN200 PN10) inside the AIDA chamber (top panels). Cabling on bottom panels corresponds to detector signal (1) and heating of optical components (2).

Besides the benefits discussed above, an additional advance arises from the possibility to operate APicT and SP-APicT in parallel. As APicT and SP-APicT share the same diode laser as light source, this parallel operation directly allows confirmation of the self-calibration property of direct TDLAS which will be discussed in detail in Section 5.3.

### 5.2.5 APeT: extractive total water hygrometer

APeT is the third AIDA TDL hygrometer and accompanies the in situ water vapor measurements of APicT and SP-APicT. It measures total water concentration in laboratory environment at room temperature by extractive sampling of AIDA gas. The stainless steel sampling line which carries the sampling gas to the instrument has a diameter of 10 mm, a length of approximately 10 m, is heated to approximately 30 °C. For typical sampling gas flows, this results in a residence time of the sampling gas within the heated sampling line of approximately five seconds. Therefore, all condensed water content in the sampling air is expected to be vaporized before entering APeT and the instrument measures total water content in gaseous form.

Initial operation of the instrument is described in (Lauer, 2007). However, APeT suffered from severe leakage at that time which caused systematic offsets in the retrieved total water concentrations of more than 4% due to intrusion of ambient air into the instrument. These issues have been resolved due to measures carried out within this work and APeT is a reliable and accurate instrument by now. Therefore, it is now possible to accurately monitor the partition of water into its gaseous and its condensed phases by deduction of LWC/IWC from the difference of APeT total water and in situ TDL water vapor measurement (Ebert et al., 2008). This is for example of great value for the ice crystal growth studies presented in Chapter 6.

The schematic outline of APeT is given in Figure 5.8. It is based around an optical multi path cell of Herriott type (Herriott et al., 1964) which is commercially available (TOPTICA Photonics, CMP-30). The Herriott cell is enclosed by a glass cylinder<sup>1</sup> which results in a cell volume of 0.9 l (cf. Figure 5.9). The base length of the Herriott cell is 0.4 m and laser light undergoes 74 passes within the cell which yields a total absorption path within the cell of 29.9 m. Laser light is coupled into the Herriott cell by a fiber coupler (Schäfter+Kirchhoff, 60SMS-1-4-A11-03) equipped with an aspheric lens with 11 mm focal length. As signal detector serves an InGaAs photo diode (Hamamatsu, G8370-01, diameter 1 mm) which collects the laser light exiting the Herriott cell. Optical path length outside the Herriott cell sums up to 0.4 m which results in a total absorption path length of APeT of 30.3 m.

---

<sup>1</sup> Tests with an electro polished stainless steel cylinder as substitute for the glass cylinder indicated no benefit in terms of improved water adsorption and desorption behavior of APeT.

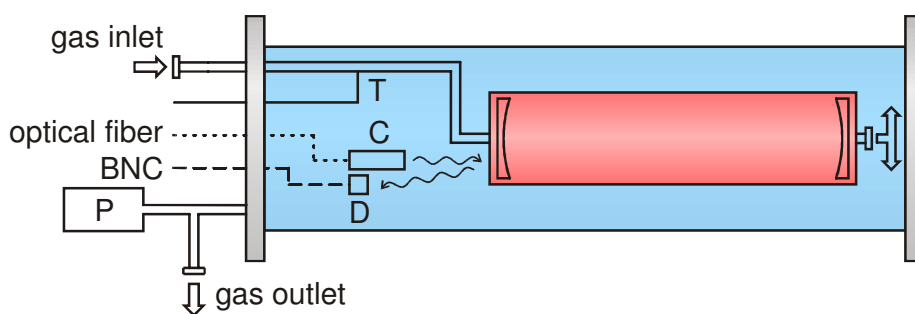


**Figure 5.8** Schematic outline of APeT. The instrument is based on an enclosed multipath cell of Herriott type (red). Coupling to the Herriott cell is realized by fiber-coupled collimating optics (C) and detector focusing optics (D). Sampling gas flow is directed to the Herriott cell after entering the instrument as indicated by arrows. Gas temperature and pressure sensors are denoted by (T) and (P), respectively. The entire optical absorption path is enclosed by a vacuum vessel (blue) to minimize parasitic absorption caused by ambient air water vapor.

To minimize and control parasitic absorption caused by ambient air contamination, the entire absorption path of APeT is enclosed by a stainless steel vacuum recipient with a nominal diameter of 20 cm (DN200CF), a length of 85 cm, and a volume of approximately 25 l. As only 1% of the absorption path lie within this volume, humidity conditions within the recipient do not have to match water vapor concentrations of the sampling gas accurately and small deviations are acceptable. The opposite is the case for the volume of the Herriott cell. Therefore, the sampling gas is lead to the Herriott cell, directly after entering APeT, via a stainless steel line (10 mm, Swagelok fittings). Only after flowing through the Herriott cell, the sampling gas enters the stainless steel recipient before exiting the instrument to the AIDA vacuum system to which APeT is connected. Sampling gas flow is controlled by a mass flow controller (Mykrolis, FC-2901V-4M) positioned behind the instrument. Typical gas flow rate is 5 SLM resulting in a time of 22 s for which integrated sampling gas flow corresponds to two times the volume of the Herriott cell. This results in an exchange of 95% of the gas volume within the Herriott cell making the stated time a measure for the response time of APeT to rapid changes in total water concentration which will be characterized in Section 5.3.1.

APeT has its own gas temperature and pressure sensors. Sampling gas temperature is monitored in the stainless steel line just before the gas enters the Herriott cell. As sensor, a thermocouple of type K is used. Gas pressure is measured by a Baratron gauge (MKS, 627BX13TDC2B) with a range of 0-1333 hPa. The gauge is positioned at the sampling gas outlet of APeT to avoid dead volume at the inlet which could negatively influence water vapor concentrations in the sampling gas.

Special care has been taken to make APeT vacuum proof. Therefore, the vacuum recipient is equipped with several Klein flange and Swagelok fitting connector. All optical and electrical signals enter and exit the instrument via commercial vacuum feedthroughs supplied by

VACOM. Vacuum tightness has been validated by determination of leak rates below 0.01 hPa per day.

To the same sampling line as APeT, a chilled-mirror FPH (MBW 373LX) is connected and allows direct comparison with APeT results. The MBW 373LX is a very accurate instrument under static humidity conditions. However, it responds slowly to dynamic changes of total water concentrations for frost points below  $-60\text{ }^{\circ}\text{C}$  and APeT shows clear advantages in time response under these conditions. The verification of this point will be given in Section 5.3 along with verification of the advances in APeT measurement accuracy. APeT total water measurements will be compared with the chilled-mirror FPH and TDL IWC with parallel measurements of a Fourier transform infrared (FTIR) spectrometer.

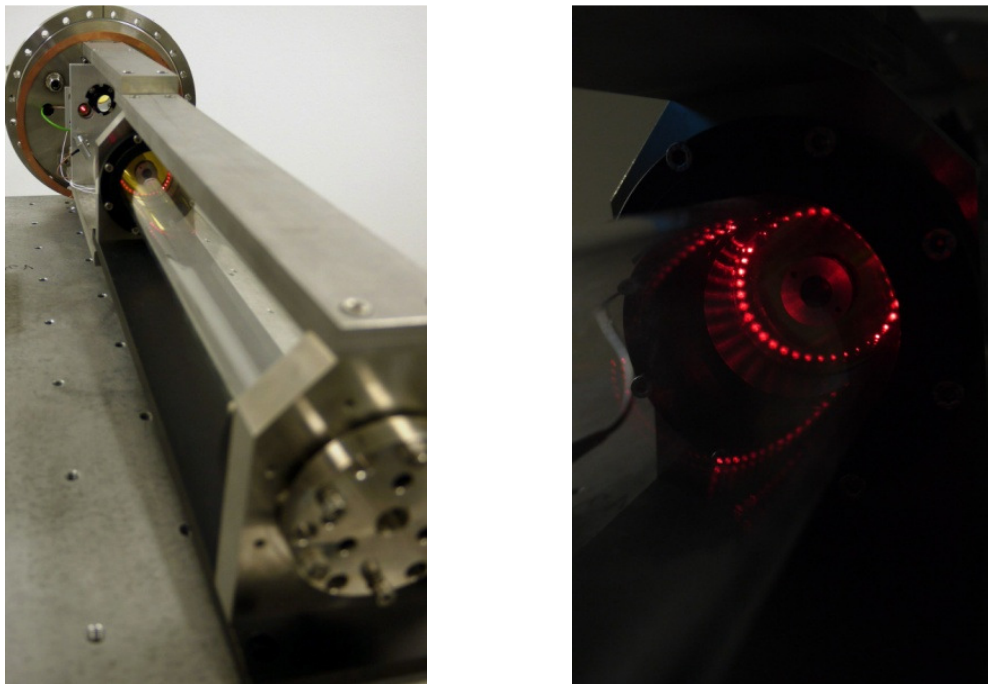


**Figure 5.9** Interior of APeT (left panel) with Herriott cell and its enclosing glass cylinder in the foreground. The right panel shows the laser spot pattern on one of the Herriott cell mirrors for laser light of wavelength 660 nm.

### 5.2.6 Characterization of residual laser water

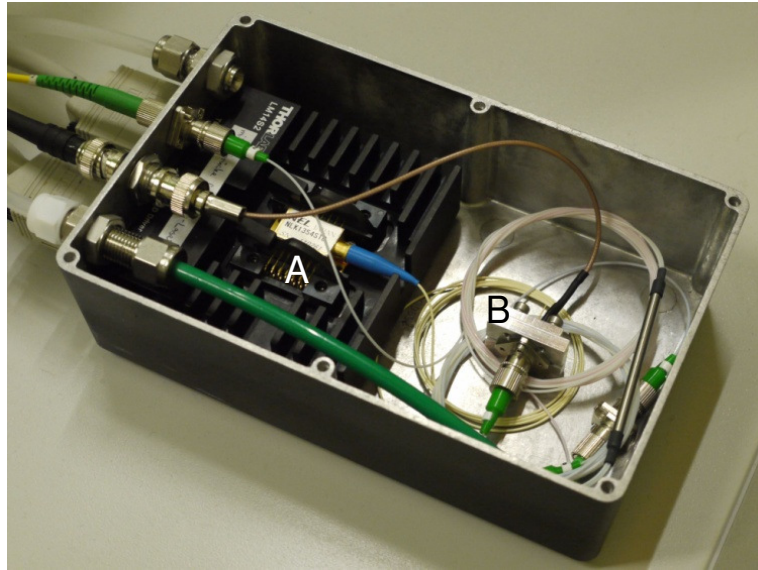
The DFB diode lasers used for the AIDA TDL hygrometers are enclosed by a so called butterfly package common for commercial telecommunication lasers. This butterfly package has the advantage of supplying built-in coupling of light emitted by the laser diode into an optical fiber. However, the butterfly package is susceptible to parasitic absorption caused by water vapor inside the package. Two different cases have to be distinguished:

1. a variable amount of water vapor in the path between laser diode and optical fiber facet which is not sealed to environment,
2. a fixed amount of water vapor inside a hermetically sealed part directly enclosing the laser diode.

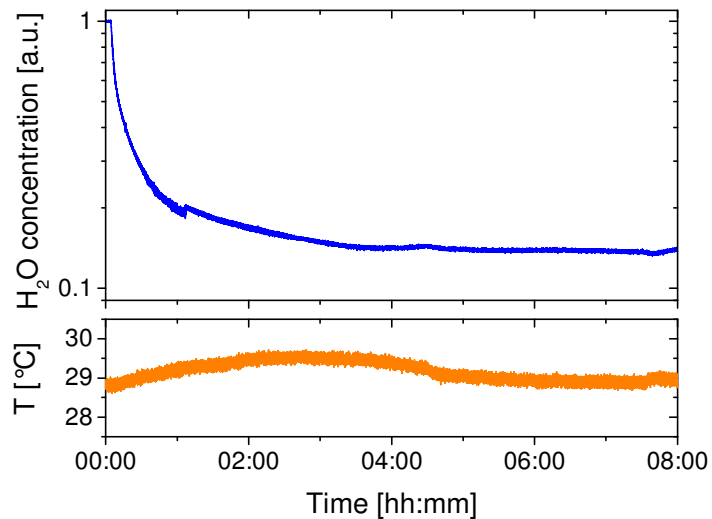
In order to avoid parasitic absorption from case one and to characterize the amount of absorption caused by case two, specialized laser enclosures have been designed of which one is depicted in Figure 5.10. The enclosures are made from aluminum diecast, contain the diode laser on its mount, and, in addition, a fiber coupled reference channel to monitor the amount of water vapor in the laser butterfly package. Light for this reference channel is obtained via a fiber splitter (Laser2000, WT-2L2C05A166) which divides light intensity in the ratio 95%/5%. 95% of intensity is used for the measurement and 5% for the reference channel. A custom made adapter directly connects the fiber output facet of the reference channel with a photodiode (Hamamatsu, G8370-01, diameter 1 mm). The enclosure is equipped with an optical fiber feedthrough and a feedthrough for the detector signal of the reference channel. Moreover, Swagelok connectors are installed to allow purging of the enclosure and the butterfly package of the laser.

Figure 5.11 shows the effect that purging of the laser enclosure with dried compressed air ( $c_{\text{H}_2\text{O}} < 10 \text{ ppmv}$ ) has on the amount of water vapor concentration inside the butterfly package of the laser. Laser enclosure and butterfly package were filled with ambient air initially. Absorption by water vapor as described by case one is efficiently eliminated after a purging duration of several hours and initial absorption can be reduced by almost a factor of ten during this purging process. The residual absorption results from hermetically sealed water vapor as described in case two and is therefore expected to be constant over time which allows corrective measures in data evaluation of the measurement absorption signal.

The characterization of this residual laser water is shown in Figure 5.12 for the two diode lasers which are in operation in the AIDA TDL hygrometers. Residual laser water has been monitored over duration of twelve days, each day containing several hours of measurement. Within the measurement error, absolute water vapor concentration of the residual laser water or equivalently absorption line area stayed constant for the entire duration of twelve days and for both diode laser although the APicT/SP-APicT laser shows 25% higher residual laser water than the APeT laser. This can be explained by manufacturing tolerances of the diode



**Figure 5.10** Newly designed laser enclosure (lid removed) for purging of the diode laser (A) with dried air. A fiber-coupled reference channel (B) is included in the enclosure to monitor the residual water vapor in the butterfly package of the diode laser.



**Figure 5.11** Effect of purging a diode laser with butterfly package. The laser is initially exposed to ambient air before purging with dried compressed air ( $c_{\text{H}_2\text{O}} < 10$  ppmv) is initiated. Ambient temperature  $T$  is shown for reference.

lasers as they are assembled under very clean conditions, but at standard ambient humidity levels.

At very low water vapor concentration levels below 1 ppmv, the absorption caused by residual laser water can be a severe source of systematic errors. For typical measurement conditions, residual laser water corresponds to a water vapor concentration  $c_{\text{H}_2\text{O}} = 46$  ppbv for APicT ( $p = 1013.25$  hPa,  $T_g = -80$  °C, and  $L = 84.006$  m) and  $c_{\text{H}_2\text{O}} = 270$  ppbv for APeT ( $p = 1013.25$  hPa,  $T_g = 25$  °C, and  $L = 30.3$  m). If measurement water vapor concentrations are below 1 ppmv, then these levels of residual laser water can systematically increase the measurement result by several tens of percents, especially for APeT, if not corrected. This will be verified in Section 5.3.

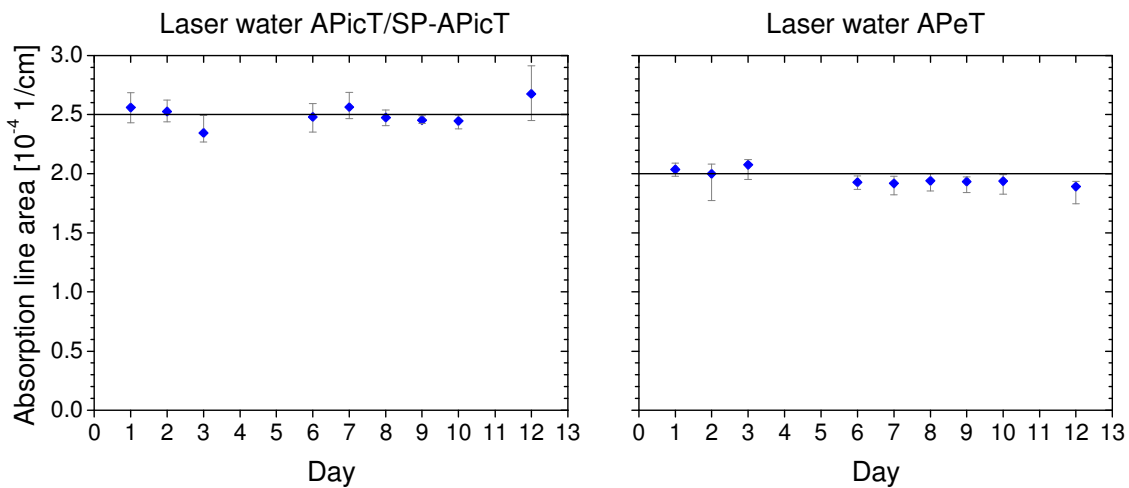


**Figure 5.12** Characterization of residual laser water of APicT/SP-APicT and APeT over several days while continuously purging with dried compressed air. Each day corresponds to a measurement of several hours for which the average retrieved absorption line area is shown. Error bars indicate the variability of retrieved absorption line area for the individual measurements. The solid black lines indicate the time average values of absorption line area. These correspond to a water vapor concentration  $c_{\text{H}_2\text{O}} = 46$  ppbv for APicT ( $p = 1013.25$  hPa,  $T_g = -80$  °C, and  $L = 84.006$  m) and  $c_{\text{H}_2\text{O}} = 270$  ppbv for APeT ( $p = 1013.25$  hPa,  $T_g = 25$  °C, and  $L = 30.3$  m).

## 5.3 Performance

After outlining the instrumental advances of the AIDA TDL hygrometers in the preceding section, an assessment of instrumental performance at present state will be given in the following. Discussion aspects include measurement time resolution and response time, signal stability, instrument sensitivity and dynamic range, measurement reproducibility, and perhaps most important measurement accuracy and its validation.

### 5.3.1 Time resolution and response time

As mentioned in the beginning of this chapter, dynamic AIDA experiments require humidity measurements with a time resolution of approximately one second. This prerequisite can easily be fulfilled by the AIDA TDL hygrometers due to their fast repetition rate of individual absorption line scans of 139.8 Hz. This repetition rate allows averaging of one hundred individual scans to obtain a time resolution of typically 0.8 s which corresponds to a high scan acquisition efficiency of approximately 90 % and permits high-sensitivity measurements with low noise (cf. Section 5.3.3).

Besides time resolution, the time response of a measurement can be of great importance if time response is much slower than the nominal time resolution. In this case, response time can limit the ability of the measurement to actually resolve temporal variations which are of the order of the nominal time resolution. Time response is no issue for APicT and SP-APicT due to their sampling-free in situ measurement of water vapor. APicT and SP-APicT measurements follow variations in the water vapor concentration immediately.

The situation is different for APeT due to the extractive nature of its total water measurement. Time response of APeT is limited for two reasons:

1. delay due to sampling gas transport from the AIDA chamber to the instrument,
2. delay due to sampling gas exchange time inside the instrument.

Total APeT time response as a combination of these two factors has been characterized for the APeT standard sampling gas flow rate of 5 SLM. Results are depicted in Figure 5.13. After starting injection of ice particles into AIDA which marks a sudden change in total water concentration, it takes approximately 17 s for APeT to register this sudden change. As reference signal to determine the exact point of time when ice particle injection starts, the signal transmission of APicT is used. The determined time delay corresponds well to expectations. The sampling line from the AIDA chamber to APeT has a volume of approximately 0.4 l and the determinant volume inside APeT is the Herriott cell with 0.9 l. This yields a combined

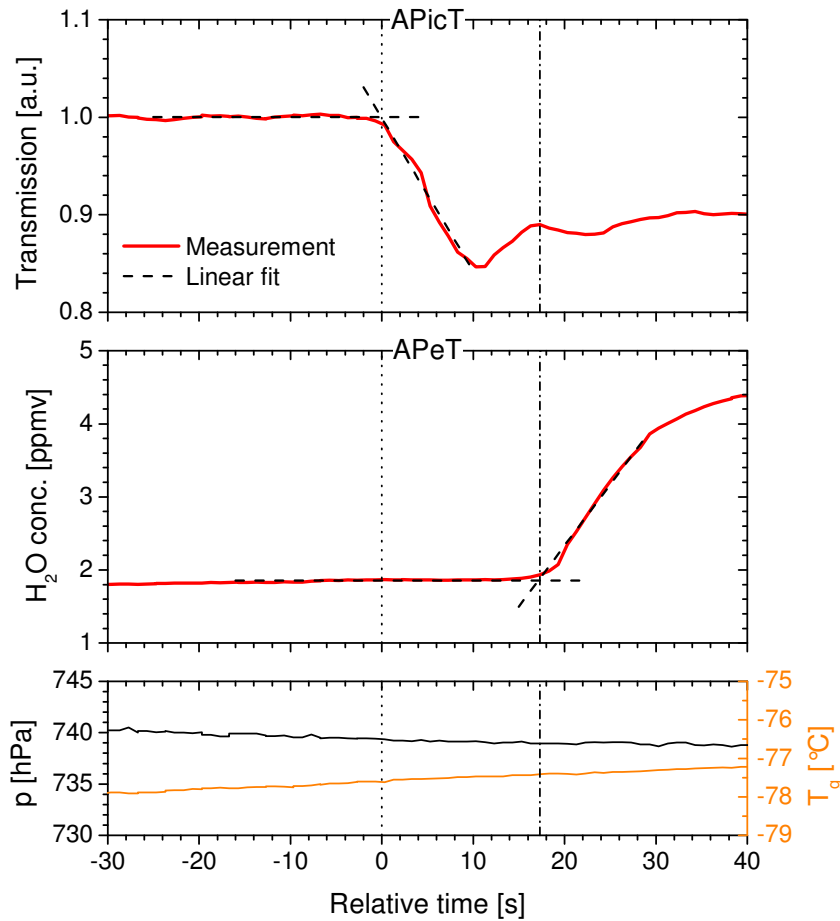


**Figure 5.13** Characterization of response time of APEt for a sudden change of total water concentration (ice particle injection) in the AIDA chamber during static thermodynamical conditions. Panels show (from top to bottom) signal transmission of APicT as indicator of ice particle concentration inside AIDA, total water concentration as measured by APEt, and AIDA gas pressure  $p$  and gas temperature  $T_g$ . Linear fits (dashed lines) are applied to the APicT and APEt signals to determine when the water concentration change is detected by APicT (dotted line) and APEt (dashed-dotted line). The time difference between APicT and APEt response is approximately 17 s.

volume of 1.3 l. For the given gas flow rate of 5 SLM, this combined volume corresponds to the gas flow integrated over a time of 16 s.

The determined response time of APeT seems to be of disadvantage, but typically, total water content changes only few percent during this time period in dynamic AIDA expansion experiments. The reason for this is that, normally, the only source for additional water content is the AIDA chamber wall and water vapor transport from the wall into the chamber volume is governed by diffusion. The diffusive transport is typically slow and mainly governed by an existing temperature gradient between AIDA wall and inner volume. However, in some rather extreme cases when this temperature gradient is of the order of 10 K and extends over more than a couple of minutes water flux from the AIDA wall can increase total water content significantly during time periods of the order of APeT response time. Then, a suitable correction for this instrument time delay has to be applied.

The response time of APeT can also be compared to that of the MBW 373LX chilled-mirror FPH (see Section 3.1) which is connected to the same sampling line as APeT. This allows direct comparison between both instruments. Contrary to the response time of APeT determined above which is expected to be rather universal if the sample gas flow is unchanged, the response time of the FPH is mainly governed by speed and reliability of its built-in mirror temperature control in case of dynamic changes of humidity. This factor especially plays a role at temperatures below  $-60\text{ }^{\circ}\text{C}$  for which water concentrations are low and changes of the frost layer density on the chilled mirror may take several tens of seconds. An example of this effect is given in Figure 5.14 for a dynamic AIDA experiment with AIDA gas temperature  $T_g \approx -60\text{ }^{\circ}\text{C}$ . The FPH shows an increased response time of approximately 30 s compared to APeT under these conditions which are even higher for temperatures below  $-60\text{ }^{\circ}\text{C}$ .

This additional lag in response time is typically not acceptable if an accurate measurement of total water content is desired as in the case of ice particle growth studies in cirrus cloud which will be presented in the following chapter. Moreover, it can be drawn from Figure 5.14 that the mirror temperature control of the FPH does insufficiently follow the dynamic change in humidity under the described conditions which results in sudden ‘steps’ in the retrieved water partial pressure signal. In summary, it can thus be concluded that APeT shows significant advantages in measurement response time of half a minute and more over the MBW 373LX FPH for AIDA experiments at temperatures below  $-60\text{ }^{\circ}\text{C}$ .

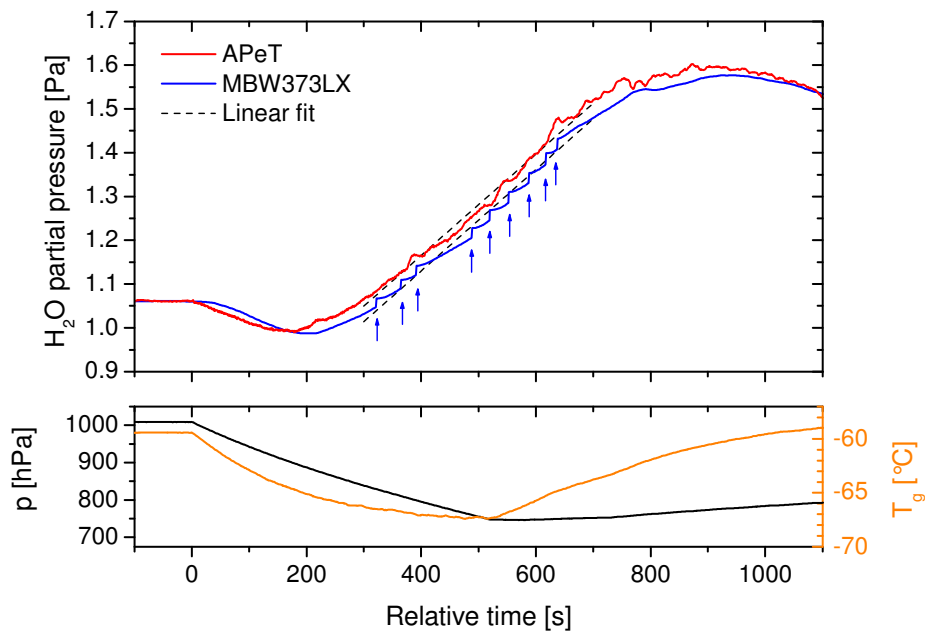


**Figure 5.14** Response time comparison between APeT and MBW 373LX frost point hygrometer for a dynamic AIDA experiment at AIDA gas temperature  $T_g \approx -60$  °C and correspondingly low total water concentrations. From linear fits (dotted lines) to the signals of both instruments, a difference in response time of approximately 30 s is determined in favor of APeT. Arrows indicate sudden jumps in the frost point hygrometer signal due to insufficiently reacting temperature control of the chilled mirror.

### 5.3.2 Signal stability and transmission losses

During the dynamic changes of pressure and temperature in AIDA expansion experiments, it is desirable for the AIDA TDL hygrometers to maintain high signal stability in order to avoid degradation of measurement sensitivity and accuracy. For APeT, this is not an issue because it is placed in laboratory environment under stable temperature conditions and the integrated Herriott multipath cell is unsusceptible to changes of AIDA gas pressure.

For the in situ TDL hygrometers APicT and SP-APicT, conditions are a bit different as they are operated inside AIDA at a temperature range typically between  $-80$  °C and  $0$  °C. This wide temperature variation together with variation of gas pressure ranging from atmospheric pressure down to below 1 Pa leads to significant warping of the AIDA chamber wall. As Figure 5.15 shows, APicT signal strength suffers dramatically from gas pressure variations of more than few hundred hectopascals and temperature variations of more than approximately 20 K. This makes realignment of the APicT optics (White multipath cell) necessary which is, e.g., not feasible during a running AIDA expansion experiment.

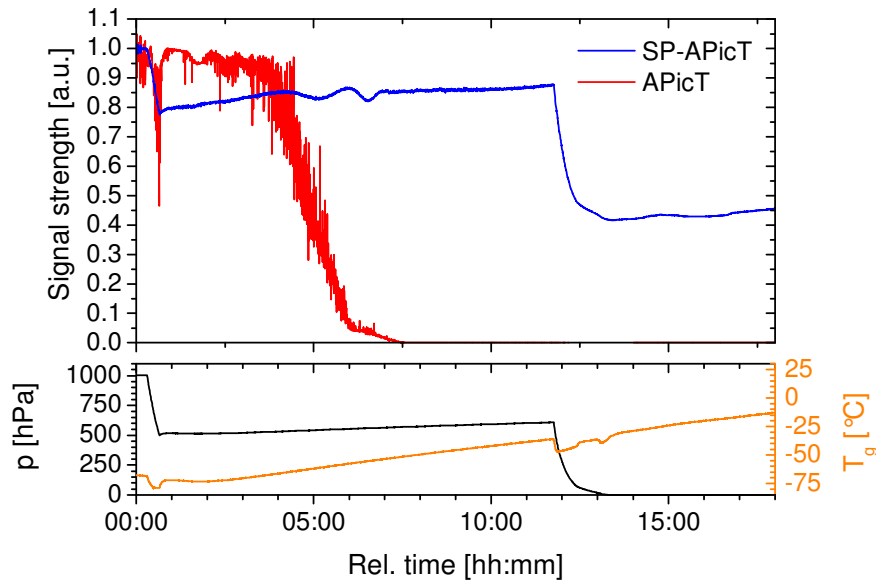


**Figure 5.15** Comparison of signal stability of SP-APicT and APicT during broad gas pressure  $p$  and temperature  $T_g$  variations in AIDA. These variations lead to warping of the AIDA chamber wall to which APicT is very susceptible and which makes optical realignment of APicT necessary. SP-APicT, in contrast, is able to retain an acceptable level of signal strength for the entire range of AIDA pressure and temperature variations without realignment.

SP-APicT, on the contrary, has very stable optics and AIDA wall warping has no such dramatic impact due to its single-path setup. These properties are verified in Figure 5.15 as SP-APicT is able to retain high levels of signal strength over the entire range of AIDA pressure and temperature variations. It therefore marks a significant advance in signal stability under dynamic conditions compared to APicT.

Besides signal stability, signal strength decrease due to transmission losses can be a significant issue for the in situ measurement of water vapor. Transmission losses occur during AIDA expansion experiments due to scattering of the TDL signal off liquid cloud droplets or ice cloud particles. This especially plays a role for warm temperatures above  $-20$  °C for which very dense clouds can be created in the AIDA chamber.

Table 5.4 compares different levels of transmission for SP-APicT with expected transmission levels of APicT. It is assumed that APicT absorption path length  $L_{\text{APicT}}$  is set to 23.6 m and scattering losses of APicT take only place along the White cell base length of 3.74 m. Scattering losses are assumed to follow an exponential dependence with respect to path length  $L$ . This implies for the transmission  $\tau$

$$\tau_{\text{APicT}} = \tau_{\text{SP-APicT}} \frac{L_{\text{APicT}}}{L_{\text{SP-APicT}}} . \quad (5.1)$$

Transmission [%]										
SP-APicT	100	90	80	70	60	50	40	30	20	10
APicT	100	56	30	14	6	2	0.7	0.1	0.02	0.0003

**Table 5.4** Expected signal transmission of APicT ( $L = 23.638$  m) for different levels of transmission of SP-APicT ( $L = 4.11$  m). APicT transmission values are calculated from Equation (5.1).

Transmission losses of up to 99% can be handled without implying additional measurement uncertainty (Ebert, 2003; Ebert et al., 2005; Giesemann, 2003). Table 5.4 shows that this threshold is underrun by APicT when SP-APicT transmission retains a relatively high transmission level of 40%. For 10% SP-APicT transmission, a fraction of below  $10^{-5}$  of the original APicT signal remains. This shows that SP-APicT has, in terms of handling of transmission losses, significant advantages over APicT in its area of application – warm and dense clouds.

In order to verify the transmission values given in Table 5.4, a comparison between APicT and SP-APicT transmission for two AIDA expansion experiments with dense mixed-phase clouds at a temperature of around  $-20$  °C is given in Figure 5.16. For the first experiment, APicT/SP-APicT ratio of transmission is approximately 30%/80%, whereas for the second experiment, this ratio is approximately 15%/70% yielding very good agreement with the expected values given in Table 5.4 for both cases.

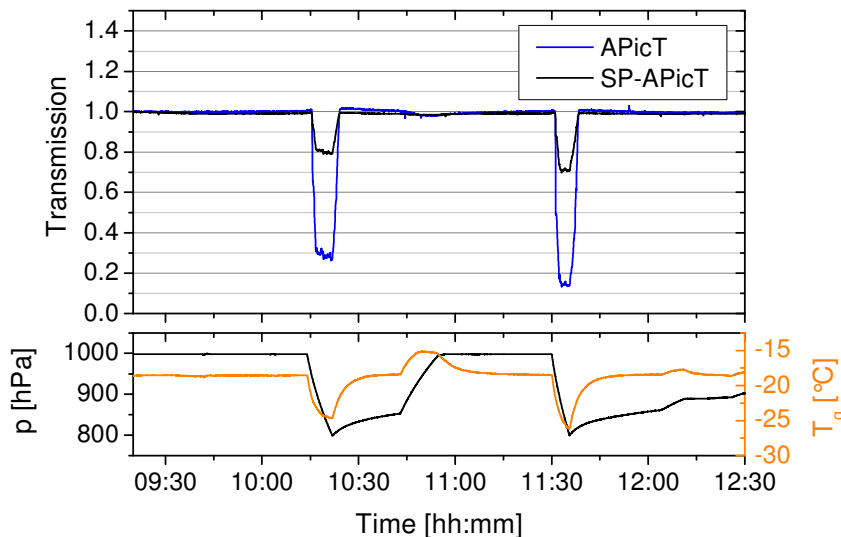


**Figure 5.16** Comparison of transmission losses of APicT ( $L = 23.638$  m) and SP-APicT ( $L = 4.11$  m) during two AIDA expansion experiments with periods of dense mixed-phase clouds at gas temperatures  $T_g$  around  $-20$  °C. Very good agreement with expected values given in Table 5.4 is observed.

### 5.3.3 Sensitivity and dynamic range

Sensitivity is a crucial parameter of any measurement as it defines its precision. For the AIDA TDL hygrometers, sensitivity can be assessed by two ways which will be described in more detail subsequently:

1. from the standard deviation  $\sigma_{\text{res}}$  of the residual between measurement data and fitted line profile in OD representation,
2. from the Allan deviation  $\sigma_A(k)$  with  $k$  being the number of averaged individual measurements.

The residual, i.e. the difference between the TDLAS measurement signal in OD representation and the fitted absorption line profile applied in data evaluation (cf. Section 5.2.2), can be used as a powerful tool to assess measurement sensitivity by computing its standard deviation  $\sigma_{\text{res}}$ .  $\sigma_{\text{res}}$  is a measure for optical resolution and can directly be translated into a water vapor sensitivity  $\Delta c_{\text{H}_2\text{O}}$ . For the three AIDA TDL hygrometers, this approach is shown in Figure 5.17, Figure 5.18, and Figure 5.19 for the typically used average of one hundred individual measurement scans (cf. Section 5.3.1). For APicT and SP-APicT, a very low  $\sigma_{\text{res}}$  of  $5 \cdot 10^{-5}$  OD is obtained which comes close to WMS detection limits of  $< 10^{-5}$  OD for water vapor measurements (Durry et al., 2002; Kerstel et al., 2002; Dyroff et al., 2010). Corresponding water vapor sensitivity is  $\Delta c_{\text{H}_2\text{O}} = 7$  ppbv for APicT and  $\Delta c_{\text{H}_2\text{O}} = 100$  ppbv for SP-APicT. For APicT, the result for  $\sigma_{\text{res}}$  is also an improvement by approximately a

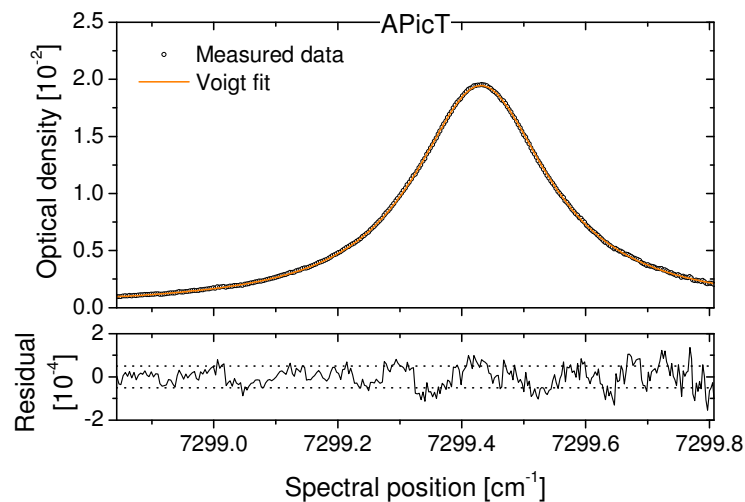


**Figure 5.17** Voigt fit to APicT absorption signal ( $L = 53.822$  m) for an average of 100 individual measurement scans. From the standard deviation of the residual  $\sigma_{\text{res}} = 5 \cdot 10^{-5}$  OD (dotted lines) as measure for optical resolution, a water vapor concentration sensitivity of  $\Delta c_{\text{H}_2\text{O}} = 7$  ppbv is inferred. ( $c_{\text{H}_2\text{O}} = 2.56$  ppmv,  $p = 1019.4$  hPa,  $T_g = -69.3$  °C).

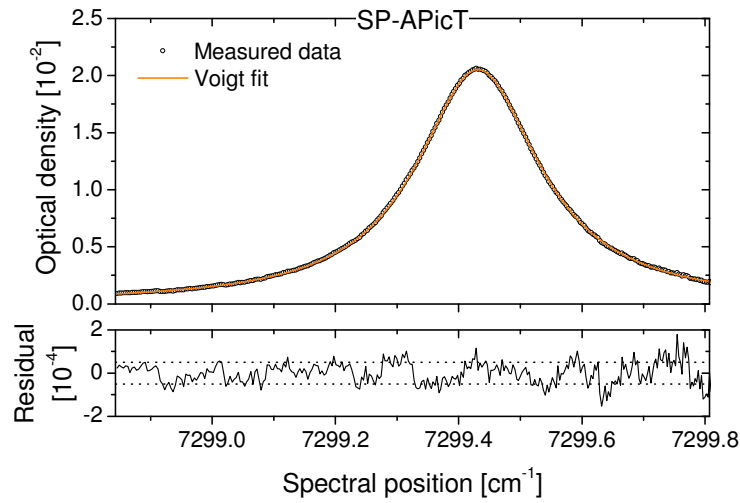


**Figure 5.18** Voigt fit to SP-APicT absorption signal ( $L = 4.11$  m) for an average of 100 individual measurement scans corresponding to Figure 5.17.  $\sigma_{\text{res}} = 5 \cdot 10^{-5}$  OD (dotted lines) implies a sensitivity  $\Delta c_{\text{H}_2\text{O}} = 100$  ppbv ( $c_{\text{H}_2\text{O}} = 40.62$  ppmv,  $p = 1015.6$  hPa,  $T_g = -48.9$  °C).

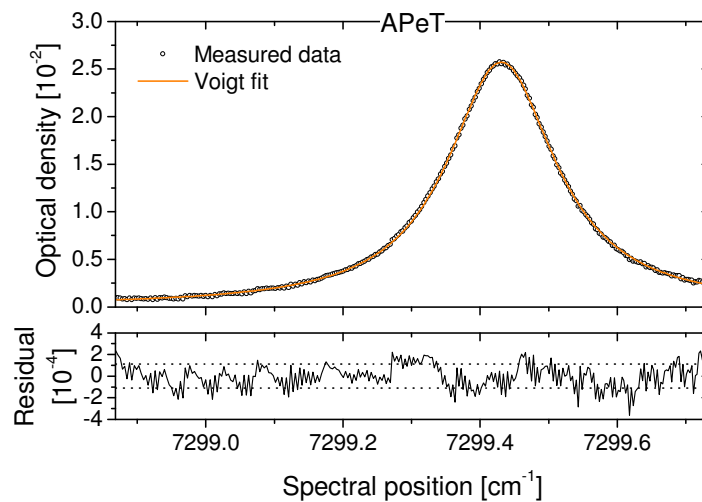


**Figure 5.19** Voigt fit to APeT absorption signal ( $L = 30.3$  m) for an average of 100 individual measurement scans corresponding to Figure 5.17.  $\sigma_{\text{res}} = 1.1 \cdot 10^{-4}$  OD (dotted lines) implies a sensitivity  $\Delta c_{\text{H}_2\text{O}} = 47$  ppbv ( $c_{\text{H}_2\text{O}} = 10.81$  ppmv,  $p = 987.4$  hPa,  $T_g = 27.1$  °C).

factor of five in optical resolution compared to the previous analysis given in (Ebert et al., 2005). The etalon interference structures which were observed in (Ebert et al., 2005) could be completely eliminated by the redesigned setup of APicT coupling optics (see Section 5.2.3). For SP-APicT, there are also no etalon interference effects visible in the residual. Remaining artifacts are most likely attributable to analog to digital conversion in data acquisition. APeT on the other hand shows slight etalon effects whose free spectral range corresponds to the base length of the APeT Herriott multipath cell. This reduces the detection limit to  $\sigma_{\text{res}} = 1.1 \cdot 10^{-4}$  OD, approximately a factor of two worse than for APicT and SP-APicT, and results in a sensitivity  $\Delta c_{\text{H}_2\text{O}} = 47$  ppbv. The elimination of the etalon effects present in the APeT signal will be addressed in future work.

As mentioned above, the second possibility to assess measurement sensitivity is the so called Allan deviation  $\sigma_A(k)$  (Allan, 1966), where  $k$  denotes the number of averaged individual measurements.  $\sigma_A(k)$  serves as a widely accepted and reliable measure to evaluate measurement sensitivity and, in addition, measurement stability (Werle, 2011). Contrary to the sensitivities  $\Delta c_{\text{H}_2\text{O}}$  given above which are determined from optical resolution, the Allan deviation gives sensitivity values by evaluating the fluctuation of retrieved water vapor concentration time series. These time series have to be acquired under static pressure, temperature, and humidity conditions. For the AIDA TDL hygrometers, the used time series to determine  $\sigma_A(k)$  are depicted in Figure 5.20 for which no averaging of individual measurement scans has been applied. Corresponding evolutions of  $\sigma_A(k)$  are shown in Figure 5.21.

Minima of  $\sigma_A(k)$  denoted by  $\sigma_A(k^*)$  corresponding to the optimal sensitivity are reached at  $\sigma_A(k^* = 50) = 4$  ppbv for APicT,  $\sigma_A(k^* = 1000) = 13$  ppbv for SP-APicT, and  $\sigma_A(k^* = 80) = 12$  ppbv for APeT. The different optimal averaging numbers  $k^*$  give a measure for signal stability where the optical multipath cells of APicT and APeT show relatively high instability that allows only for moderate averaging of 50-100 individual measurements. On the contrary, SP-APicT allows averaging of approximately 1000 individual measurements for optimal sensitivity which underlines its very stable optical setup and is comparable to similar single path setups used for water vapor detection (Hunsmann et al., 2008). The optimal normalized Allan deviation resulting for SP-APicT is  $\sigma_A(k^* = 1000) = 53$  ppbv  $\cdot$  m which is also comparable to the optimal value of 45 ppbv  $\cdot$  m given in (Hunsmann et al., 2008). APicT and APeT are not able to reach such a low value, but are almost equivalent in terms of optimal normalized Allan deviation with  $\sigma_A(k^* = 50) = 336$  ppbv  $\cdot$  m and  $\sigma_A(k^* = 80) = 364$  ppbv  $\cdot$  m, respectively.

For the typical number of averages used for AIDA measurements,  $k = 100$ , one obtains the following Allan deviation values:  $\sigma_A(k = 100) = 5$  ppbv for APicT, which marks an improvement by approximately a factor of three with respect to a comparable analysis given in (Ebert et al., 2005),  $\sigma_A(k = 100) = 25$  ppbv for SP-APicT, and  $\sigma_A(k = 100) = 13$  ppbv

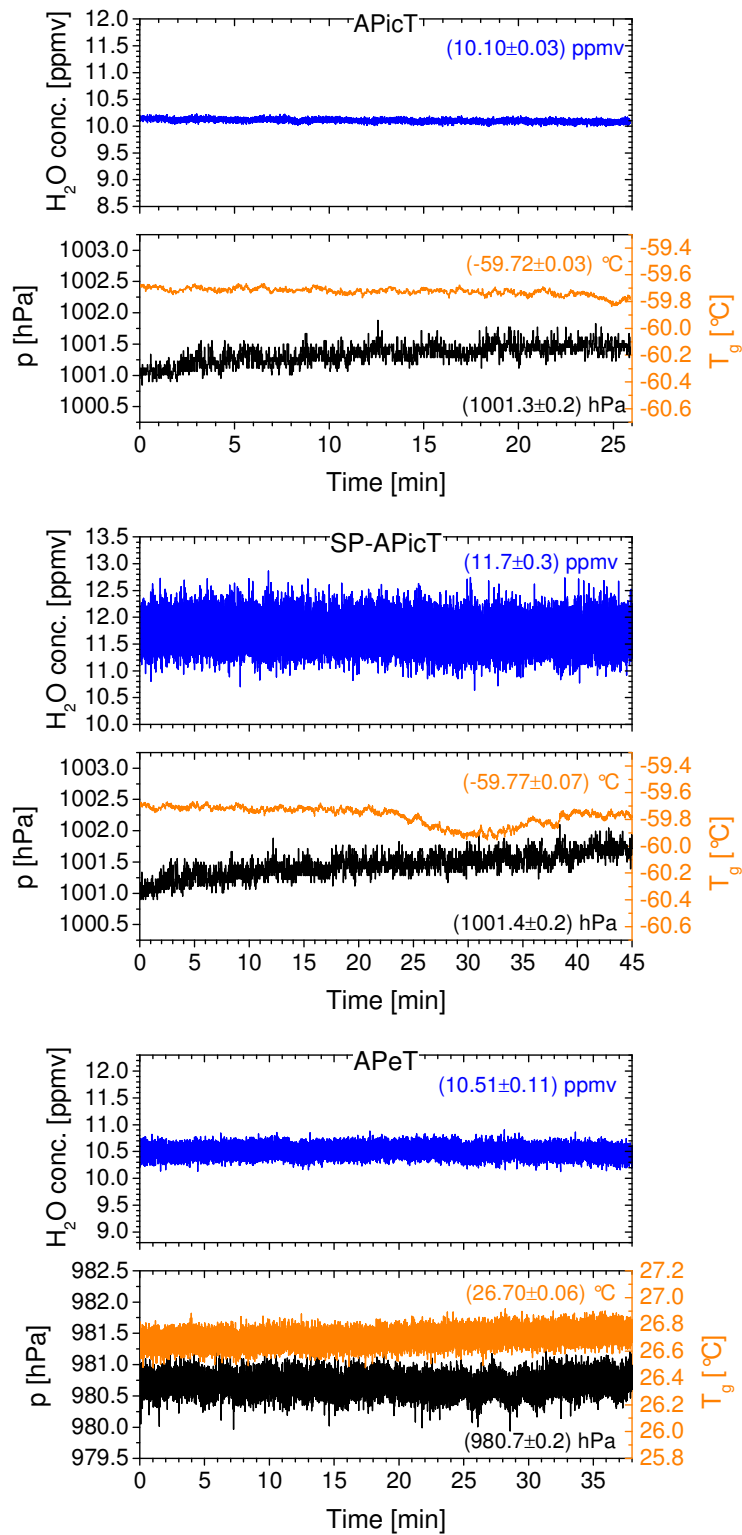


**Figure 5.20** Water vapor time series of APicT ( $L = 84.006\text{im}$ ), SP-APicT ( $L = 4.11\text{AP}$ ), and APeT ( $L = 30.3\text{ A}$ ) for static AIDA gas pressure  $p$ , temperature  $T_g$ , and humidity conditions (no averaging of individual measurement scan data). All vertical axes have same scaling.

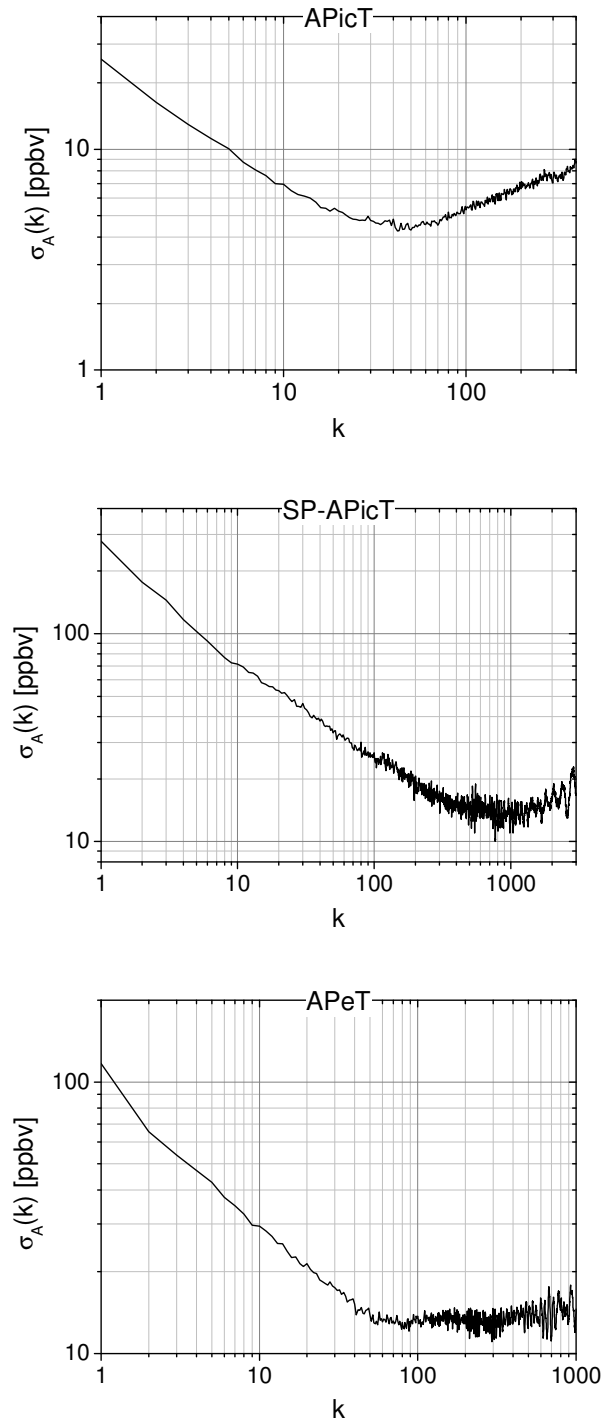


**Figure 5.21** Allan deviations  $\sigma_A(k)$  for APicT ( $L = 84.006$  m), SP-APicT ( $L = 4.11$  m), and APeT ( $L = 30.3$  m) derived from the time series shown in Figure 5.20.  $k$  denotes the number of averaged individual measurement scans.

for APeT. These values can be compared to the  $\Delta c_{\text{H}_2\text{O}}$  values derived from optical resolution given above which were likewise determined for averaging of 100 individual measurement scans. For APicT, both values correspond well with respect to each other (5 ppbv/7 ppbv) whereas for SP-APicT (25 ppbv/100 ppbv) and APeT (13 ppbv/47 ppbv), the Allan deviation values are approximately a factor of four lower than the values of  $\Delta c_{\text{H}_2\text{O}}$ . For APeT, this deviation can be attributed to the observed etalon effects which are relatively stable in time and therefore do not significantly degrade measurement sensitivity with respect to retrieved water vapor concentration which is expressed by  $\sigma_A(k)$ . For SP-APicT, the most likely reason for the deviation is that its very stable optical setup allows higher water vapor concentration sensitivities than its optical resolution would imply.

Besides sensitivity which defines the lower end of the dynamic range of an instrument, the upper limit of dynamic range has to be characterized as well. For SP-APicT, this is exemplarily shown in Figure 5.22. As maximal positively tested absorption for a qualitatively reasonable measurement, a value of 4.4 OD is inferred which is also representative for APicT and APeT measurements. This maximum in optical density translates into a maximum in water concentration of  $c_{\text{H}_2\text{O}} = 13000$  ppmv for SP-APicT,  $c_{\text{H}_2\text{O}} = 2000$  ppmv for APicT ( $L = 23.64$  m), and  $c_{\text{H}_2\text{O}} = 1500$  ppmv for APeT ( $L = 30.3$  m).

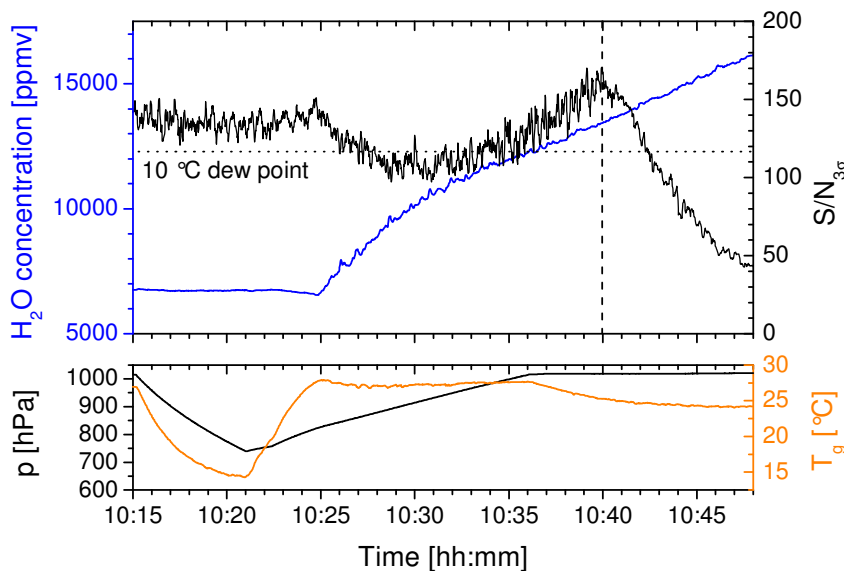


**Figure 5.22** Determination of dynamic range upper limit of SP-APicT ( $L = 4.11$  m). The upper limit is defined as the value in  $c_{\text{H}_2\text{O}}$  above which signal to noise ratio  $S/N_{3\sigma}$  starts to drop (dashed line) due to saturation of the absorption signal. It is reached for  $c_{\text{H}_2\text{O}} \approx 13000$  ppmv which corresponds to a maximum absorption of 4.4 OD. 10 °C dew point (dotted line) as well as AIDA gas pressure  $p$  and temperature  $T_g$  are shown for reference.

Table 5.5 summarizes the previously discussed performance of the AIDA TDL hygrometers in terms of dynamic range, sensitivity, optical resolution, and time resolution. Accompanying the performance values of APicT, SP-APicT, and APeT, derived values for the TDL IWC/LWC, which is inferred from the difference of APeT total water and APicT water vapor content, have been determined where applicable. While assessing the performance of the instruments it is in particular mentionable that APicT performance could be improved by a factor of five in optical resolution and by a factor of three in sensitivity compared to the previous analysis in (Ebert et al., 2005) due to advances in optical design. Moreover, the introduction of SP-APicT has extended the total dynamic range of in situ water vapor detection by more than a factor of six compared to the upper limit of the dynamic range of APicT taken alone.

	DR [ppmv]	Typ. $\Delta c_{\text{H}_2\text{O}}$ [ppbv]	Typ. $\Delta c_{\text{H}_2\text{O}}$ [ppbv·m]	Typ. $\Delta c_{\text{H}_2\text{O}}$ [°C FP]	Typ. $\sigma_{\text{res}}$ [OD]	Typ. $\Delta t$ [s]
APicT	<1-2000	5 (15)	420	-105	$5 \cdot 10^{-5}$ ( $2.5 \cdot 10^{-4}$ )	0.8
SP-APicT	<10-13000	25	103	-97	$5 \cdot 10^{-5}$	0.8
APeT	<1-1500	13	394	-100	$1.1 \cdot 10^{-4}$	0.8
TDL IWC/LWC (APeT-APicT)	<1-1500	14	–	-100	–	0.8

**Table 5.5** Summary of the AIDA tunable diode laser (TDL) hygrometer performance with dynamic range (DR) in ppmv, sensitivity  $\Delta c_{\text{H}_2\text{O}}$  in ppbv, ppbv · m, and equivalent values in °C frost point (FP), and optical resolution  $\sigma_{\text{res}}$  in OD units. Derived values for the TDL ice water and liquid water content (IWC/LWC), which is inferred from the difference of APeT total water and APicT water vapor content, have been determined where applicable. Values in parentheses refer to a previous analysis of APicT performance given in (Ebert et al., 2005). Typical values are given for an average of 100 individual measurement scans resulting in a time resolution  $\Delta t$  of below one second. Sensitivity values  $\Delta c_{\text{H}_2\text{O}}$  are obtained from Allan deviations  $\sigma_A(k = 100)$  in Figure 5.21 and reflect APicT performance for  $L = 84.006$  m. Optical resolution values  $\sigma_{\text{res}}$  are derived from Figure 5.17, Figure 5.18, and Figure 5.19.

### 5.3.4 Reproducibility and self-calibration

As it has been pointed out before, direct TDLAS measurements are self-calibrating in a sense that no calibration measures are necessary to quantify measurement accuracy. This inherent property of self-calibration implies measurement result reproducibility which, in this context, is defined as the coincidence of measurement results obtained under identical conditions and with identical measurement techniques, but with different measurement instruments.

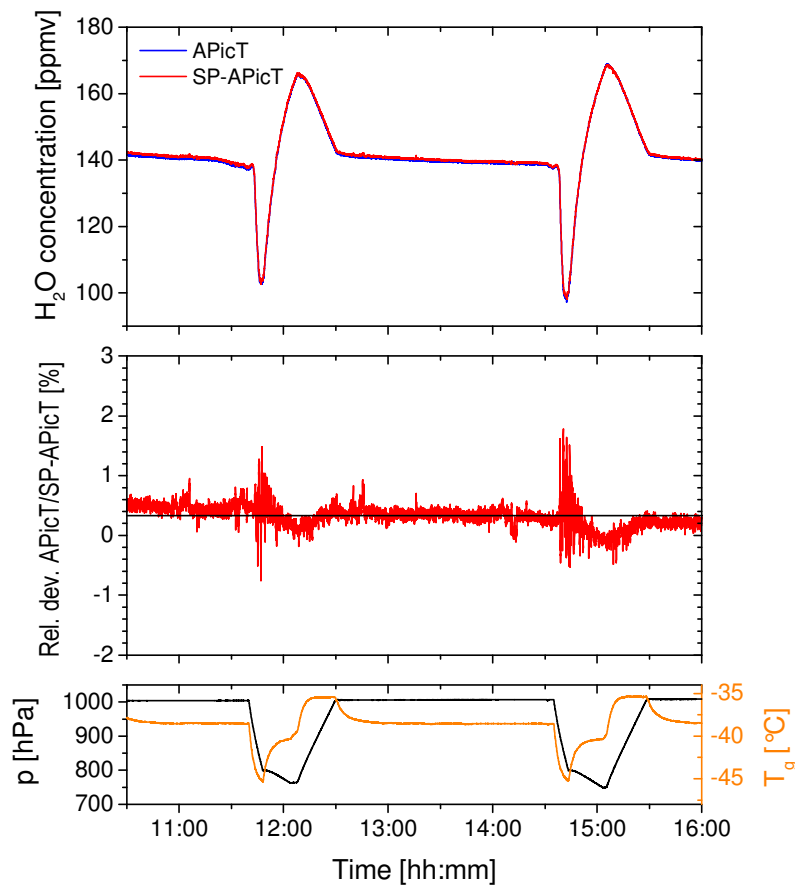


**Figure 5.23** Simultaneous water vapor concentration measurement of APicT and SP-APicT during static and dynamic AIDA conditions (top panel). No alignment or equalization of data has been applied. Average relative deviation between both instruments is 0.3% (solid black line, second panel from top). Bottom panel shows AIDA gas pressure  $p$  and gas temperature  $T_g$ .

For the AIDA TDL hygrometers, the simultaneous measurement of APicT and SP-APicT is ideal to validate self-calibration of direct TDLAS by confirmation of reproducibility according to the given definition. The reason for this is that APicT and SP-APicT share all principal components such as the diode laser, laser driver electronics, and pressure and temperature

sensors and, most important, utilize the same absorption line for measurements. Both instruments only deviate significantly in length and slightly in position of their absorption paths. It is therefore expected that deviation between APicT and SP-APicT are at most 1-2% resulting solely from the uncertainty in absorption path lengths. Effects from differing optical setup are expected to be negligible. Due to the slightly different position of APicT and SP-APicT absorption paths inside the AIDA chamber, deviations can reach higher values than 1-2% during dynamic AIDA experiments, but should stay within 1-2% on average.

An example for reproducibility of APicT and SP-APicT results is given in Figure 5.23 for periods of static AIDA conditions and two dynamic expansion experiments extending in total over six hours. Average deviation between both instruments is 0.3% for static and dynamic conditions combined and well below the expected limit of 1-2%. Maximum deviation during dynamic conditions approaches 2%, but this can be attributed to the different positions of APicT and SP-APicT absorption paths as discussed. The presented example thus confirms the self-calibration property of direct TDLAS.

### 5.3.5 Accuracy and validation by different measurement techniques

In Section 5.1, the sources of measurement uncertainty for the AIDA TDL hygrometers APicT, SP-APicT, and APeT have been discussed. Advances in measurement accuracy that are a result of the improvements and developments concerning all three AIDA TDL hygrometers have been laid out in Section 5.2 and this advances will be briefly summarized in the beginning of this section. Subsequently, examples are given to validate the accuracy of the AIDA TDL hygrometers by comparison with independent measurements of the MBW 373LX FPH and in situ retrieval of ice water content by FTIR spectroscopy (Wagner et al., 2006).

Table 5.6 summarizes the sources of measurement uncertainty that have been eliminated by the measures described in Section 5.2 together with the estimated reduction of measurement uncertainty. Especially elimination of absorption line cross interference and accurate characterization of residual laser water mark major advances in measurement accuracy.

It is expected that for a wide range of measurement conditions all additional sources of measurement uncertainty in water concentration could be eliminated besides the spectroscopic measurement uncertainty of 5% which is dominated by uncertainty of absorption line strength and absorption path length (cf. Section 5.1). The attempt of a verification of the assumption that 5% is the uncertainty or accuracy, respectively, of all TDL water concentration measurements at AIDA for a wide range of pressure, temperature, and humidity conditions will be given in the following.

First confirmation of APicT accuracy could be drawn from the AquaVIT intercomparison campaign at AIDA in 2007 (Ebert et al., unpublished; Fahey et al., 2009). In situ

	Optical design	Residual laser water	Cross interference
APicT	up to 2%	5% (typ.)	n/a
SP-APicT	n/a	<1%	up to 8%
APeT	n/a	27% (typ.)	n/a

**Table 5.6** Summary of estimated measurement uncertainty reduction for the AIDA tunable diode laser hygrometers due to different measures. Optical design changes and characterization of residual laser water address measurement uncertainties resulting from parasitic absorption of water vapor while the introduction of SP-APicT addresses uncertainty from absorption line cross interference. For the application range of SP-APicT ( $c_{\text{H}_2\text{O}} > 100$  ppmv), residual laser water has negligible impact. Typical values are given for a water concentration  $c_{\text{H}_2\text{O}} = 1$  ppmv at typical APicT and APeT measurement conditions (cf. Figure 5.12).

measurements of APicT in the temperature range between  $-90$  °C and  $-30$  °C were compared to water vapor saturation pressures over ice during periods of water vapor saturation inside the chamber, i.e. relative humidity  $\text{RH}_{\text{ice}} = 100\%$ , and deviations of  $\pm 3\%$  at maximum were found.

However, these measurements took place at AIDA gas pressures  $p < 500$  hPa in contrast to most AIDA experiments which start at atmospheric pressure of around 1000 hPa. For these low pressures, it is possible to quite easily correct for parasitic absorption signals from e.g. residual laser water. This can be done in data evaluation because parasitic absorption takes place at environmental pressure and the resulting absorption signal is broad compared to the narrower measurement absorption signal. Due to this distinction, it is possible to subtract the parasitic from the measurement absorption signal.

This approach cannot be taken if gas pressures are around ambient pressure, since it not possible to distinguish between measurement and parasitic absorption under these conditions. It was therefore important to carefully characterize parasitic absorption caused by residual laser water and to minimize any further sources of parasitic absorption (see Section 5.2). The success of these efforts is validated in Figure 5.24 for low water vapor concentrations at around  $-75$  °C and static pressure levels between 200 hPa and 1000 hPa. With correction of parasitic laser water absorption, average deviation between APicT and APeT range between 1% at  $p = 1000$  hPa and 2% at  $p = 200$  hPa.. Average deviation between APeT and MBW 373LX FPH extractive measurements is 3.9% over all pressure levels where FPH measurement accuracy is given by 2% under these conditions. The FPH accuracy is determined by an accuracy of the measured frost point of 0.1 K, cf. Section 3.1.

For comparison, Figure 5.25 shows the same measurements as Figure 5.24, but without correction of parasitic absorption by residual laser water. The effect is clear – deviations between APicT and APeT are now up to 17.3% at  $p = 1000$  hPa and deviations between

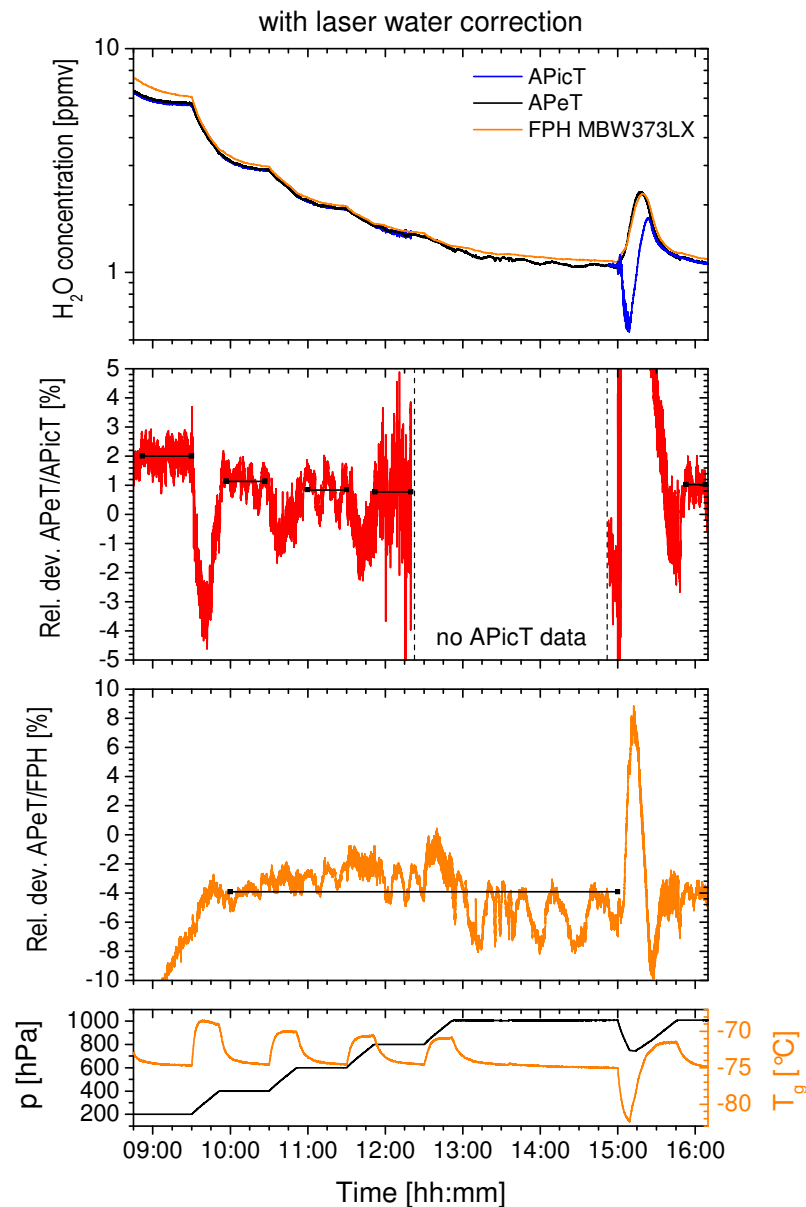


**Figure 5.24** Measurements of water vapor from APicT as well as total water from APeT and MBW 373LX frost point hygrometer (FPH) at low water concentrations during static AIDA conditions at different gas pressure levels between 200 hPa and 1000 hPa and during one dynamic expansion experiment (top panel). Correction of parasitic water vapor inside the diode laser package was applied to APicT and APeT data. No APicT data is available between 12:20 and 14:50 due to increasing misalignment of the APicT White cell optics with increasing gas pressure  $p$ . Average relative deviation between APicT and APeT measurement during static conditions varies between 1% and 2% depending on gas pressure  $p$  (solid black lines, second panel from top). Corresponding average deviation between APeT and MBW 373LX FPH is  $-3.9\%$  (solid black line, third panel from top); accuracy of MBW 373LX measurement is 2% under these conditions. Bottom panel shows AIDA gas pressure  $p$  and gas temperature  $T_g$ . Pressure level 200 hPa has been neglected for the comparison APeT/FPH, since response time of the FPH was too low to approach a constant concentration value. This very long response time also causes the large deviation between APeT and FPH during the dynamic experiment (15:00-15:30).

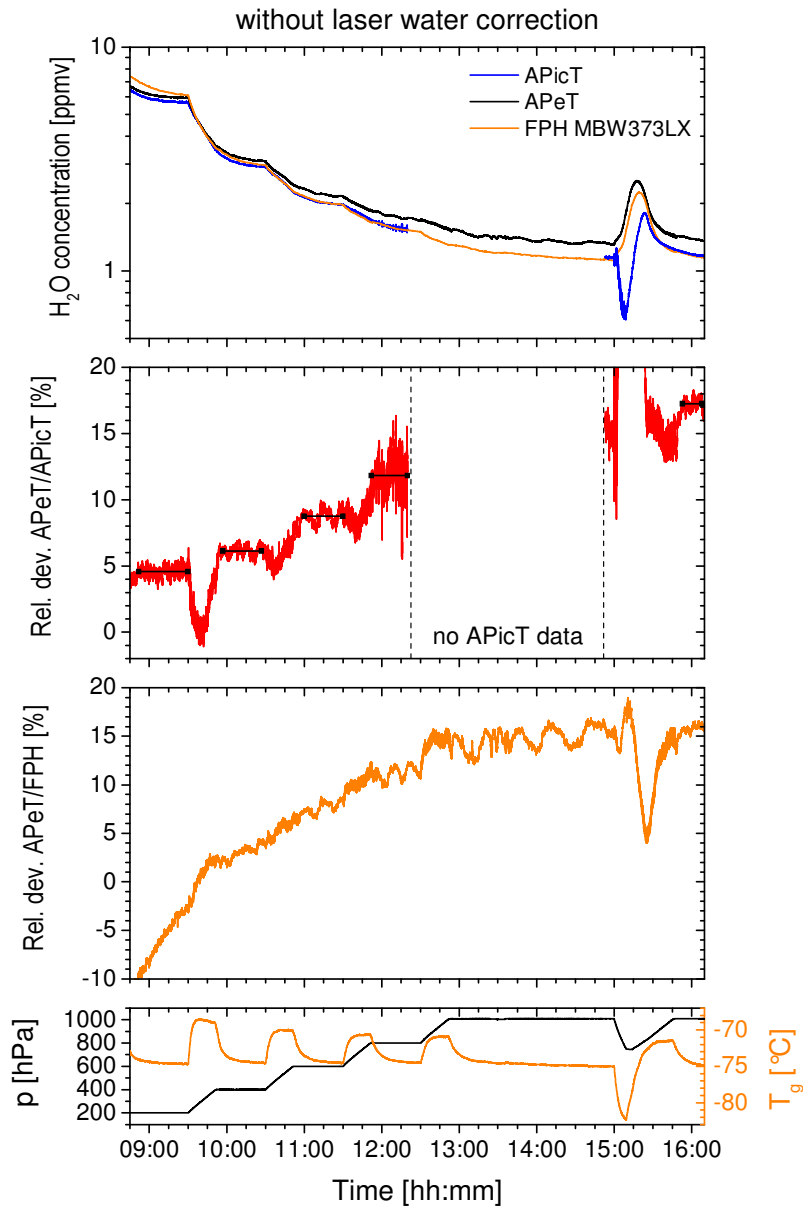


**Figure 5.25** Corresponding data to Figure 5.24 but without correction of parasitic water vapor inside the diode laser package for APicT and APeT. Overall deviations between the instruments are much higher than for applying this correction. Impact of the neglect of laser water increases with increasing gas pressure  $p$ . Maximal deviations are reached for 1000 hPa with 17.3% between APeT and APicT as well as  $\sim 15\%$  between APeT and MBW 373LX FPH.

APeT and FPH up to 15%. This confirms the dramatic effect that parasitic absorption of laser water can have if not corrected.

Further validation is given by time series of APicT, APeT, and MBW 373LX FPH for intermediate humidity levels at gas temperatures around  $-45\text{ }^{\circ}\text{C}$  which are shown in Figure 5.26. AIDA conditions included static conditions at  $p \approx 1000\text{ hPa}$  as well as three dynamic AIDA expansion experiments over a total duration of seven hours. TDL IWC was inferred for the three expansion experiments from the difference of APeT total water and APicT water vapor measurement and is compared to IWC retrieved by FTIR spectroscopy in situ, but at a lower time resolution of 10 s for one experiment. Details of this comparison are shown in Figure 5.27. For more information on the FTIR spectrometer, see Section 3.1 or (Wagner et al., 2006).

Average deviation in Figure 5.26 between APicT and APeT is very low at 0.2% during static cloud-free conditions. The same holds true for the average deviation between APeT and MBW 373LX FPH of 1.6%. It has been determined over the entire time series for which FPH accuracy is approximately 1% (corresponding to 0.1 K frost point accuracy). Looking at the comparison of IWC measurements between TDL and FTIR in Figure 5.27, a slightly higher average deviation of 4.3% is obtained, but this has to be seen in context of the FTIR measurement accuracy of 10% (Wagner et al., 2006).

Summarizing the results given in this section, the measures in instrumental improvement and development as well as characterization of parasitic absorption by residual laser water described in Section 5.2 had clear impact on improving measurement accuracy of the AIDA TDL hygrometers. For the given examples, deviations between the AIDA TDL hygrometers and the MBW 373LX FPH as well as between TDL IWC and FTIR IWC are covered by a TDL measurement accuracy of 5%. Thus, there is strong indication that 5% can be used as valid accuracy for APicT, SP-APicT, APeT, and TDL IWC for a wide range of measurement conditions.

The expected ranges for these conditions are summarized in Table 5.7. The lowest accurately measurable water concentrations are given by 1 ppmv, as these were the lowest humidity levels in AIDA after completion of all described measures to enhance measurement accuracy, cf. Figure 5.24. The upper limit of accurately measurable in situ water vapor concentrations is estimated to be 4000 ppmv following the discussion of self broadening of the standard AIDA water vapor absorption line in Section 5.1.

Future plans aim to yield a more rigorous validation of the accuracy of the AIDA TDL hygrometers and extend the range of accurately measureable water vapor concentrations at the lower and upper end. These plans involve the validation of APeT measurements at the German primary humidity standard at PTB<sup>2</sup>. Moreover, the second water intercomparison

---

<sup>2</sup> Physikalisch-Technische Bundesanstalt, Braunschweig, Germany.

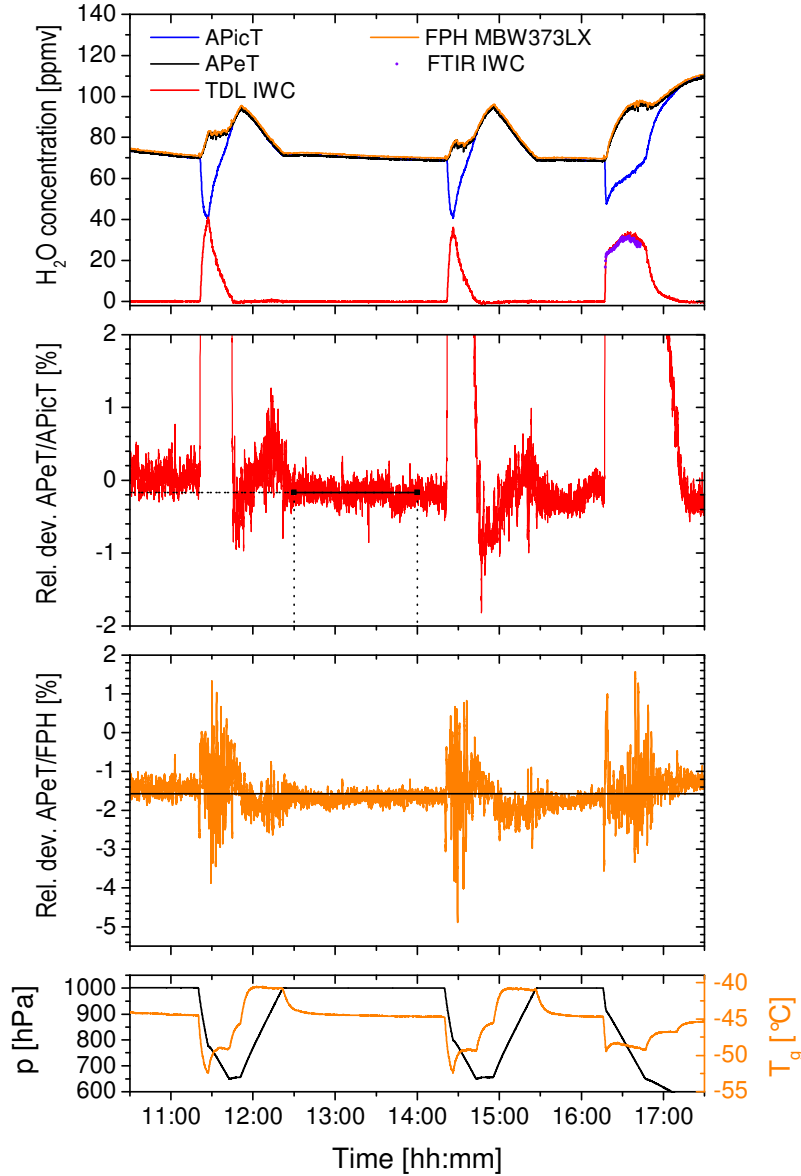


**Figure 5.26** Measurements of water vapor from APicT, total water from APeT and MBW 373LX frost point hygrometer, and ice water content (see details in Figure 5.27) from APeT/APicT and Fourier transform infrared (FTIR) spectroscopy during static and dynamic AIDA conditions (top panel). Average relative deviation between APicT and APeT measurement during static cloud-free conditions is  $-0.2\%$  (solid black line, second panel from top). Average deviation between APeT and MBW 373LX FPH during static and dynamic conditions is  $-1.6\%$  (solid black line, third panel from top); accuracy of MBW 373LX measurement is  $1\%$  under these conditions. Bottom panel shows AIDA gas pressure  $p$  and gas temperature  $T_g$ .

campaign AquaVIT2 at AIDA is planned for 2012. This will allow further validation of APicT, SP-APicT, and APeT measurement by extensive comparison with distinct instruments and measurement techniques.

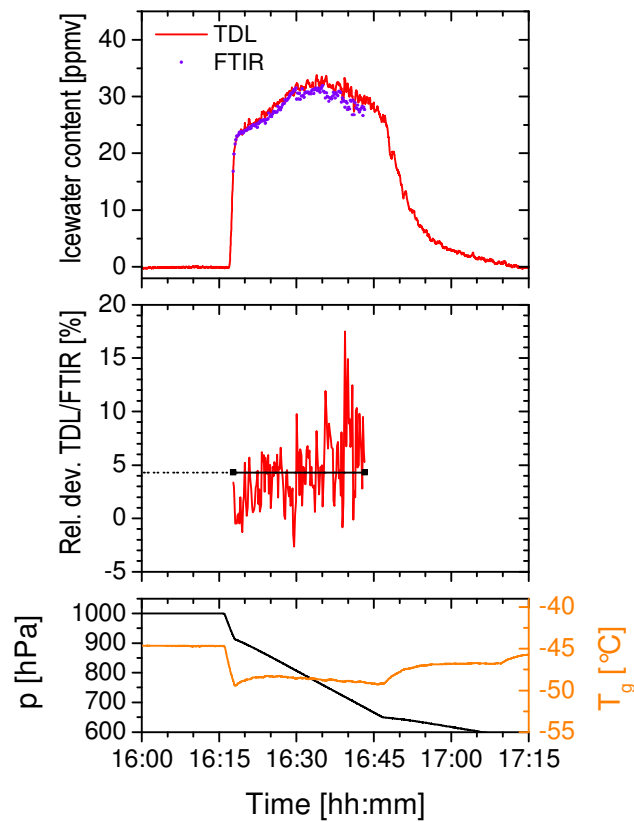


**Figure 5.27** Measurements of tunable diode laser (TDL) and Fourier transform infrared (FTIR) ice water content (top panel) for the third AIDA expansion experiment shown in Figure 5.26. Average deviation between both instruments is 4.3% during the experiment (solid black line, second panel from top); accuracy of FTIR measurement is 10%. Bottom panel shows AIDA gas pressure  $p$  and gas temperature  $T_g$ .

	$c_{\text{H}_2\text{O}}$ range [ppmv] $p = 1000 \text{ hPa}$	$c_{\text{H}_2\text{O}}$ range [ppmv] $p = 200 \text{ hPa}$	$T_g$ range [°C] $p = 1000 \text{ hPa}$
APicT/SP-APicT	1-4000	5-4000	-75 to -5
APeT	1-1500	5-1500	-75 to -15
TDL IWC/LWC (APeT-APicT)	1-1500	5-1500	-75 to -15

**Table 5.7** Expected range of measurement conditions for which an accuracy of 5% is taken to apply for the AIDA tunable diode laser (TDL) hygrometers. The relevant quantities are water vapor and total water concentration  $c_{\text{H}_2\text{O}}$  and AIDA gas pressure  $p$ . The given ranges of AIDA gas temperature  $T_g$  approximately correspond to the respective  $c_{\text{H}_2\text{O}}$  intervals under the assumption of water saturation with respect to ice. According ranges for the TDL ice water and liquid water content (IWC/LWC) have been derived from the intersection of the respective intervals of APicT/SP-APicT and APeT.

## Chapter 6

# Accommodation coefficient of water molecules on growing cirrus ice particles

Cirrus clouds play a major role in the radiative budget of the Earth's atmospheric system through their interactions with incident solar and surface-emitted terrestrial radiation (Liou, 1986). Radiative properties of cirrus clouds strongly depend on ice particle size, shape, and number concentration (Zhang et al., 1999). Ice particle properties and number concentration in cirrus clouds are a direct consequence of ice particle growth rates (Lin et al., 2002). One of the main parameters governing growth of ice particles up to a size of few micrometers, i.e. in the initial stage of ice particle growth in cirrus clouds, is the accommodation coefficient of water molecules on ice. Its magnitude, however, is only weakly constrained by present laboratory and model studies – especially for the case of ice particle growth in cold cirrus clouds.

This chapter is therefore concerned with the determination of the accommodation coefficient of water molecules on ice  $\alpha_{\text{ice}}$  by means of simulated cirrus clouds in experiments at the cloud chamber AIDA. For the evaluation of these experiments in the temperature range between 190 K and 235 K and the retrieval of  $\alpha_{\text{ice}}$ , the ice growth model SIGMA (Simple Ice Growth Model for determining Alpha) has been developed. As  $\alpha_{\text{ice}}$  plays a significant role in cirrus cloud modeling, an overview of previous experimental studies and applications in modeling will be given in the following section. A brief summary of the theoretical description of atmospheric ice particle growth is outlined in Section 6.2 and is used as basis for the ice growth parameterization within SIGMA. Section 6.3 deals with specific details of SIGMA and its development. Realization of the AIDA cirrus cloud experiments along with application of SIGMA to the experimental data is described in Section 6.4 followed by a summary of the results for the accommodation coefficient of water molecules on ice along with a discussion of these results closes this chapter.

## 6.1 Overview and role for modeling of cirrus clouds

The accommodation coefficient of water molecules on ice,  $\alpha_{\text{ice}}$ , also known as deposition coefficient, is defined as the sticking probability of water molecules that collide with an ice surface, e.g. of an ice particle, and is of importance in the so called kinetic growth regime (see Section 6.2.1). It therefore contributes to the mechanisms governing the growth speed of ice particles in cirrus clouds. In the following,  $\alpha_{\text{ice}}$  will be called ice accommodation coefficient or simply accommodation coefficient, for brevity.

The accommodation coefficient can have severe influence on ice growth within cirrus clouds for small ice particles up to few micrometers and also on the general properties of these clouds. Cirrus cloud model calculations have shown that  $\alpha_{\text{ice}}$ -values below 0.1 going down to 0.001 can lead to a significant increase in ice number concentration by several orders of magnitude compared to  $\alpha_{\text{ice}} = 1$  (Lin et al., 2002; Gierens et al., 2003). In contrast, values in the range 0.1-1 have only little impact compared to an ice accommodation coefficient equal to unity. The reason for this increase in ice number concentration will be outlined in the following.

Supersaturations with respect to ice in the upper troposphere can steadily be increased by updraft of an air parcel and the resulting adiabatic cooling. Ice nucleation, i.e. the formation of an ice particle from a primary aerosol particle, requires that a certain supersaturation threshold is exceeded. This is illustrated in Figure 6.1. After ice nucleation has set in, the growing ice particles tend to deplete the supersaturation (green curve in Figure 6.1). The reason for increasing ice number concentrations with decreasing  $\alpha_{\text{ice}}$  is that lower values of  $\alpha_{\text{ice}}$  lead to higher suppression of ice particle growth in cirrus clouds. This suppression results in a longer time during which supersaturation stays above the nucleation threshold allowing more ice nuclei to be activated within the cloud (orange curve in Figure 6.1). This increased ice number concentration enhances optical depth and albedo of cirrus clouds, i.e. the radiative properties, similar to the well-known Twomey effect (Lohmann and Feichter, 2005; Twomey, 1974). In addition, the ice growth suppression leads to higher persisting supersaturations. For such unexpectedly high persisting supersaturations that have been observed in cirrus clouds, a very low ice accommodation coefficient could serve as explanation (Gao et al., 2004; Peter et al., 2006).

The outlined impact on the ice particle growth and the properties of cirrus clouds make  $\alpha_{\text{ice}}$  a relevant parameter in cirrus cloud modeling. It is included in the formalisms for cloud ice formation in general circulation models (Kärcher et al., 2006; Kärcher and Lohmann, 2002a, b, 2003; Morrison and Gettelman, 2008), parcel models (Cotton et al., 2007), and box models (Spichtinger and Gierens, 2009).

However,  $\alpha_{\text{ice}}$  is badly constrained experimentally so far, with experimental values ranging from the order  $10^{-3}$  up to unity. For a comprehensive summary of experimental results for

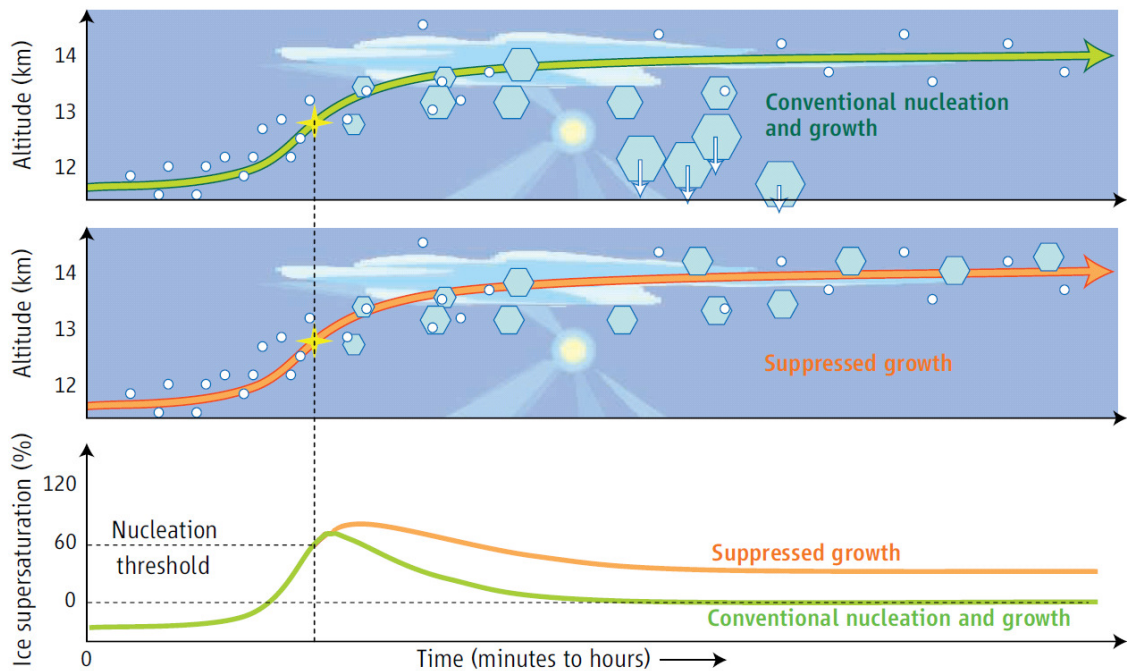


**Figure 6.1** Illustration of the temporal evolution of ice supersaturation in cirrus clouds for conventional ice nucleation (nucleation onset indicated by stars) and ice particle growth as well as for suppressed particle growth, e.g. induced by a low ice accommodation coefficient  $\alpha_{ice}$ . Figure adopted from (Peter et al., 2006) and modified.

$\alpha_{ice}$  from laboratory measurements, see (Choulaton and Latham, 1977; Haynes et al., 1992; Pruppacher and Klett, 1997). A representative selection of laboratory studies that were performed at temperatures relevant for ice growth in cirrus clouds is given in Table 6.1. With respect to the applied experimental approach, they can be divided into two groups.

One approach observes ice growth under very low pressures of less than 1 Pa, e.g. in an ultra-high-vacuum chamber or low-pressure flow reactor. Under these conditions, the ice growth rate is directly proportional to  $\alpha_{ice}$ . Ice growth rates are, e.g., determined by interferometric measurement of the thickness of a plane ice layer (Haynes et al., 1992) or by measurement of the molecular water vapor flux to the ice surface through mass spectroscopic techniques (Pratte et al., 2006). These experiments typically yield results  $\alpha_{ice} > 0.1$  for cirrus cloud temperatures. However, the ice samples investigated are much larger and of different appearance than typical cirrus cloud ice particles.

The other approach monitors the growth of single homogeneously frozen droplets which are electrostatically levitated in vertical wind tunnels (Magee et al., 2006; Earle et al., 2010). These two experiments obtained  $\alpha_{ice}$ -values far below 0.1. The retrieved value by (Earle et al., 2010) is  $\alpha_{ice} = 0.031$  and the results by (Magee et al., 2006) suggest very low  $\alpha_{ice}$ -values in the range 0.004-0.009.

$\alpha_{ice}$	Temperature [K]	Method	Reference
$1.06 \pm 0.1 > \alpha_{ice} > 0.65 \pm 0.08$	20-185	Plane ice layer growth	(Haynes et al., 1992)
$0.48 \pm 0.04 > \alpha_{ice} > 0.08 \pm 0.03$	140-210	Condensed ice sample growth	(Pratte et al., 2006)
$0.004 \pm 0.002 < \alpha_{ice} < 0.009 \pm 0.003$	213-233	Frozen droplet growth	(Magee et al., 2006)
$0.031 \pm 0.001$	234-236	Frozen droplet growth	(Earle et al., 2010)

**Table 6.1** Overview of representative laboratory measurements of the accommodation coefficient  $\alpha_{ice}$  at temperatures relevant for cirrus clouds. Results are spread over almost three orders of magnitude. Previous studies are summarized in (Choulaton and Latham, 1977; Haynes et al., 1992; Pruppacher and Klett, 1997).

Besides these laboratory measurements, there are several cirrus cloud model studies, summarized in Table 6.2, which vary  $\alpha_{ice}$  in model calculations until a good agreement between model output and observational data, i.e. measured ice number concentrations or ice supersaturations, is achieved. They either investigate atmospheric cirrus cloud data from local airborne measurements (Gierens et al., 2003; Kärcher and Ström, 2003; Kay and Wood, 2008) as well as from global retrievals (Lohmann et al., 2008) or simulated cirrus clouds in cloud chamber experiments (Haag et al., 2003; Saunders et al., 2010). Except in the study by (Gierens et al., 2003), an accommodation coefficient greater than 0.1 is preferred. Based on the results of these studies,  $\alpha_{ice}$  is generally assumed in the range of 0.2-1 for the parameterization of cirrus ice particle growth in all the different types of models mentioned previously. However,  $\alpha_{ice}$ -values have either be retrieved for very limited data sets at one specific temperature (Gierens et al., 2003; Kay and Wood, 2008; Haag et al., 2003) or rather weak statements on the magnitude of  $\alpha_{ice}$  are given (Kärcher and Ström, 2003; Lohmann et al., 2008; Saunders et al., 2010). Moreover, none of these analyses have performed a thorough uncertainty analysis for their retrieved  $\alpha_{ice}$ -values.

The reasons for the wide spread of values for the ice accommodation coefficient obtained by different experimental measurements and model studies remains unknown. Some rather speculative explanations have been brought forward such as that  $\alpha_{ice}$  could depend on particle size (Gierens et al., 2003; Magee et al., 2006) or supersaturation (Nelson and Baker, 1996) or that reactions on the ice particle surface take place which inhibit the incorporation of water vapor molecules (Gao et al., 2004). A more detailed discussion of this open question will follow in Section 6.5.

$\alpha_{\text{ice}}$	Temperature [K]	Study	Reference
$0.01 < \alpha_{\text{ice}} < 0.1$	225	Atmospheric, local	(Gierens et al., 2003)
0.2 preferred over 0.05	210-235	Atmospheric, local	(Kärcher and Ström, 2003)
$> 0.1$	225	Atmospheric, local	(Kay and Wood, 2008)
0.5 preferred over 0.006	$< 238$	Atmospheric, global	(Lohmann et al., 2008)
$> 0.2$	202	Cloud chamber	(Haag et al., 2003)
0.1 preferred over 1	180-200	Cloud chamber	(Saunders et al., 2010)

**Table 6.2** Overview of cirrus cloud model studies with their preferred values or ranges for the accommodation coefficient  $\alpha_{\text{ice}}$ . Studies include examination of atmospheric cirrus clouds and of simulated cirrus clouds in cloud chamber experiments.

Due to the specified relevance of the ice accommodation coefficient  $\alpha_{\text{ice}}$  in cirrus cloud modeling, dedicated experiments at the cloud chamber AIDA simulating the formation and evolution of cirrus ice particles under realistic conditions were carried out to quantify  $\alpha_{\text{ice}}$ . The dynamic expansion experiments cover a wide temperature range relevant for cirrus clouds between 190 K and 235 K. Cooling rates and maximally obtained supersaturations are representative of cirrus clouds formed by orographic waves (Field et al., 2001). This resulted in realistic cirrus ice particle growth yielding representative particle sizes and shapes. In addition, the retrieval of  $\alpha_{\text{ice}}$  includes a careful uncertainty analysis in order to set proper lower bounds on the ice accommodation coefficient (see Section 6.4 and following sections).

## 6.2 Theory of atmospheric ice particle growth

Mass transfer of water molecules to the surface of atmospheric ice particles determines the process of their growth. The mathematical expressions for the description of this mass transfer will be outlined in this section. They are adapted from (Seinfeld and Pandis, 2006, Chapter 12) and (Pruppacher and Klett, 1997, Chapter 13). These formulations are based on the assumption of spherical ice particles. Incorporation of non-spherical particle shapes will be discussed in Section 6.2.5.

Three cases or regimes for ice particle growth have to be distinguished dependent on particle radius  $r_p$  compared to the mean free path of water vapor molecules in air  $\lambda_w$ . It is useful to define the Knudsen number  $\text{Kn}$  in this context

$$\text{Kn} = \frac{\lambda_w}{r_p}. \quad (6.1)$$

The Knudsen number is used to distinguish between the different regimes of ice particle growth. If  $\text{Kn} \gg 1$ , mass transport is determined by elementary gas kinetic processes in the so called kinetic regime. In this regime, the accommodation coefficient  $\alpha_{\text{ice}}$  plays a dominant role. On the other hand, if  $\text{Kn} \ll 1$ , the flux of water molecules to the ice particle is governed by diffusion in the so called continuum regime. The intermediate regime between kinetic and continuum regime is called transition regime ( $\text{Kn} \approx 1$ ) and connects the mass transfer formulation of both limiting cases. For atmospheric conditions relevant for cirrus clouds,  $\lambda_w$  typically takes values of 200 nm and above. This means that that ice particles in natural cirrus clouds stay in the kinetic and intermediate regime until they are a few micrometers in size.

### 6.2.1 Kinetic regime

In the kinetic regime ( $\text{Kn} \gg 1$ ), mass transfer is governed by elementary gas kinetic mechanisms, i.e. by collision of randomly moving water vapor molecules with the surface of an ice particle. For water molecules in three-dimensional random motion, the number of molecules  $Z_{\text{H}_2\text{O}}$  in moles hitting a unit area per unit time is given by

$$Z_{\text{H}_2\text{O}} = \frac{1}{4} n_{\text{H}_2\text{O}} \bar{c}_w, \quad (6.2)$$

where  $n_{\text{H}_2\text{O}}$  is the molar concentration of water vapor and  $\bar{c}_w$  the mean thermal speed of water vapor molecules:

$$\bar{c}_w = \left( \frac{8RT_g}{\pi M_w} \right)^{1/2} \quad (6.3)$$

with the universal gas constant  $R$ , the gas temperature  $T_g$ , and the molar mass of water  $M_w$ .

Multiplying (6.2) by  $M_w$  and the surface area of the ice particle  $4\pi r_p^2$  and making use of the ideal gas law, the net mass transfer to the particle per unit time can be expressed by

$$\frac{dm_p}{dt} = \alpha_{\text{ice}} \frac{\pi r_p^2 \bar{c}_w M_w}{R} \left( \frac{e_\infty}{T_g} - \frac{\hat{e}_{\text{ice}}(T_s)}{T_s} \right), \quad (6.4)$$

where  $e_\infty$  is the water vapor partial pressure far away from the ice particle and  $\hat{e}_{\text{ice}}(T_s)$  the saturation vapor pressure with respect to ice for particle surface temperature  $T_s$ . The accommodation coefficient  $\alpha_{\text{ice}}$  enters here as the sticking probability or efficiency, respectively, of water molecules colliding with the surface of the ice particle.

### 6.2.2 Continuum regime

In the continuum regime ( $\text{Kn} \ll 1$ ), diffusion processes govern water vapor mass transfer. The water vapor diffusion to the surface of a spherical ice particle can be described by

$$\frac{dn_{\text{H}_2\text{O}}}{dt} = D_w \left( \frac{\partial^2 n_{\text{H}_2\text{O}}}{\partial r^2} + \frac{2}{r} \frac{\partial n_{\text{H}_2\text{O}}}{\partial r} \right), \quad (6.5)$$

where  $D_w$  is the diffusivity of water molecules in air and  $r$  the radial position with respect to particle center. For the initial and boundary conditions

$$n_{\text{H}_2\text{O}}(r > r_p, t = 0) = n_{\text{H}_2\text{O},\infty}, \quad (6.6)$$

$$n_{\text{H}_2\text{O}}(r = \infty, t) = n_{\text{H}_2\text{O},\infty}, \quad (6.7)$$

$$n_{\text{H}_2\text{O}}(r = r_p, t) = n_{\text{H}_2\text{O},s}, \quad (6.8)$$

the stationary solution of (6.5), i.e.  $dn_{\text{H}_2\text{O}}/dt = 0$ , is given by

$$n_{\text{H}_2\text{O}}(r) = n_{\text{H}_2\text{O},\infty} - \frac{r_p}{r} (n_{\text{H}_2\text{O},\infty} - n_{\text{H}_2\text{O},s}) \quad (6.9)$$

or equivalently in terms of water vapor pressure

$$n_{\text{H}_2\text{O}}(r) = \frac{e_\infty}{RT_g} - \frac{r_p}{r} \left( \frac{e_\infty}{RT_g} - \frac{\hat{e}_{\text{ice}}(T_s)}{RT_s} \right). \quad (6.10)$$

The net mass transfer to the ice particle per unit time can be expressed by

$$\frac{dm_p}{dt} = 4\pi r_p^2 D_w M_w \left. \frac{\partial n_{\text{H}_2\text{O}}}{\partial r} \right|_{r=r_p}, \quad (6.11)$$

which in combination with (6.10) yields

$$\frac{dm_p}{dt} = \frac{4\pi r_p D_w M_w}{R} \left( \frac{e_\infty}{T_g} - \frac{\hat{e}_{\text{ice}}(T_s)}{T_s} \right). \quad (6.12)$$

Note that (6.12) is linear in  $r_p$  compared to (6.4) which is quadratic in  $r_p$ . This implies that  $dr_p/dt \propto 1/r_p$  for the continuum regime, whereas  $dr_p/dt$  is independent of  $r_p$  for the kinetic regime. In contrast to the kinetic regime, radial growth of ice particles in the continuum regime is therefore more and more inhibited for increasing  $r_p$ .

### 6.2.3 Transition regime

The transition regime connects the limiting cases of the kinetic and the continuum regime ( $\text{Kn} \approx 1$ ). One possibility for a description of the transition regime is the so-called flux-matching approach which is illustrated in Figure 6.2. This approach assumes that for distances away from the ice particle surface smaller than the vapor jump length  $\Delta_v$ , water vapor transport is governed by elementary gas kinetic mechanisms, i.e. the kinetic regime applies. For distances greater than  $\Delta_v$ , on the other hand, water vapor transport is governed by diffusion and the continuum regime is valid. At the boundary defined by  $r = r_p + \Delta_v$ , the water vapor fluxes of both regimes have to be matched.

A reasonable choice for the vapor jump length  $\Delta_v$  has to be taken. Here, the approach by Dahneke (Dahneke, 1983; Seinfeld and Pandis, 2006) will be discussed. It assumes  $\Delta_v = \lambda_w$  and furthermore defines

$$\lambda_w = \frac{2D_w}{\bar{c}_w}. \quad (6.13)$$

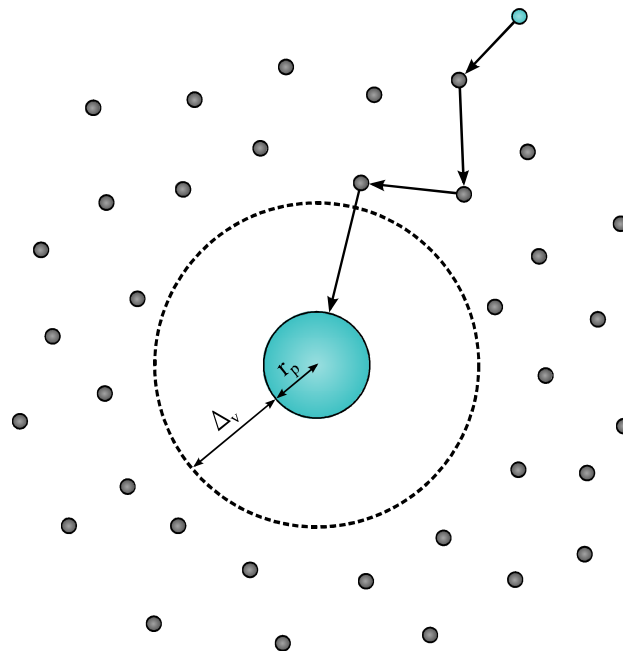


**Figure 6.2** Illustration of growth of a spherical ice particle (blue, center) with radius  $r_p$  in the transition regime. For distances away from the ice particle surface greater than the vapor jump length  $\Delta_v$ , the transport of a water molecule (blue, upper right) to the ice particle is governed by diffusion (continuum regime), i.e. the motion of the water molecule is determined by interaction with the surrounding air molecules (grey). For distances smaller than  $\Delta_v$ , the transport is governed by elementary gas kinetics (kinetic regime).

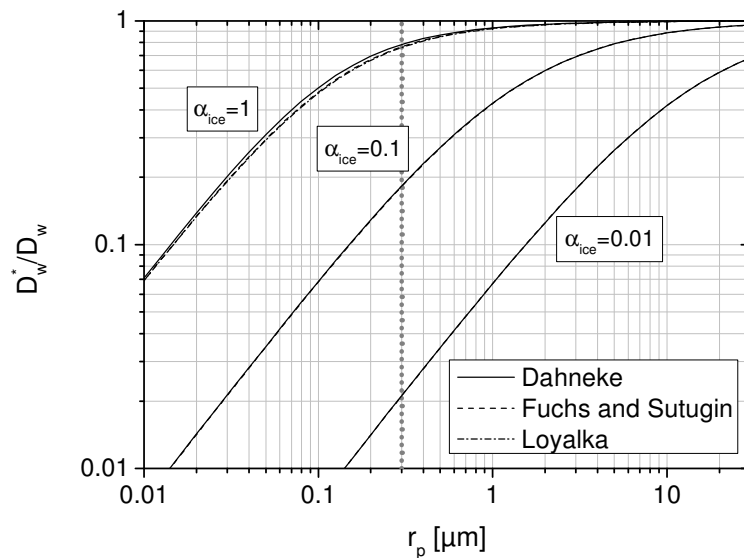


**Figure 6.3** Comparison of different parameterizations of the modified diffusivity  $D_w^*$  in the transition regime dependent on ice particle radius  $r_p$  for accommodation coefficient  $\alpha_{\text{ice}} = 1$ ,  $\alpha_{\text{ice}} = 0.1$ , and  $\alpha_{\text{ice}} = 0.01$ . Mean free path is set to  $\lambda_w = 70$  nm, representative of AIDA expansion experiments. The dotted line at  $r_p = 0.3$   $\mu\text{m}$  indicates the size threshold above which ice particle growth can be detected by the available AIDA instrumentation. Note that the Loyalka parameterization is only valid for  $\alpha_{\text{ice}} = 1$ .

The diffusivity  $D_w$  in (6.12) is then replaced by a modified diffusivity  $D_w^*$ :

$$\frac{dm_p}{dt} = \frac{4\pi r_p D_w^* M_w}{R} \left( \frac{e_\infty}{T_g} - \frac{\hat{e}_{\text{ice}}(T_s)}{T_s} \right). \quad (6.14)$$

$D_w^*$  is connected to  $D_w$  by

$$\frac{D_w^*}{D_w} = \frac{1 + \text{Kn}}{1 + 2\text{Kn}(1 + \text{Kn})/\alpha_{\text{ice}}}. \quad (6.15)$$

For  $\text{Kn} \rightarrow 0$ ,  $D_w^*/D_w \rightarrow 1$  as expected. Likewise for  $\text{Kn} \rightarrow \infty$ ,  $D_w^*/D_w \rightarrow \alpha_{\text{ice}}/(2\text{Kn})$  which in combination with (6.13) transforms (6.14) into the limiting case of the kinetic regime (6.4).

The Dahneke transition regime parameterization (6.15) can be compared to corresponding parameterizations by Fuchs and Sutugin as well as Loyalka (Seinfeld and Pandis, 2006). This is depicted in Figure 6.3 for different values of the accommodation coefficient  $\alpha_{\text{ice}}$  and a mean free path  $\lambda_w = 70$  nm. Differences between all parameterizations are very low with maximum deviations of few percent. The chosen magnitude of  $\lambda_w$  is representative of dynamic AIDA expansion experiments at gas pressures around 1000 hPa. In these AIDA experiments, growth of ice particles with  $r_p > 300$  nm can be observed with the available

AIDA instrumentation (see Section 6.4). For these particle sizes, Figure 6.3 shows significant sensitivity with respect to  $\alpha_{\text{ice}}$ .

### 6.2.4 Latent heat of deposition

As additional effect to be included in (6.14), the release of latent heat from deposition of water molecules on the surface of an ice particle can be investigated. So far, the ice particle surface temperature  $T_s$  has not been considered. If latent heat release can effectively be depleted by a sufficiently high heat conductivity of air,  $k_a$ ,  $T_s$  approaches the temperature of the surrounding air  $T_g$ . However, as for the diffusivity  $D_w$ ,  $k_a$  has to be modified for gas kinetic effects which reduces the magnitude of  $k_a$  for small ice particle sizes  $r_p$  and leads to  $T_s > T_g$ . The modified heat conductivity  $k_a^*$  is given by

$$\frac{k_a^*}{k_a} = \frac{1}{1 + \frac{4k_a}{\alpha_T r_p \rho_a c_{p,a} \bar{c}_a}}, \quad (6.16)$$

where  $\alpha_T$  is the thermal accommodation coefficient,  $\rho_a$  the density of air,  $c_{p,a}$  the specific heat of air, and  $\bar{c}_a$  the mean thermal speed of air molecules corresponding to (6.3). The thermal jump distance  $\Delta_T$  was set to zero according to (Fukuta and Walter, 1970). As choice for  $\alpha_T$ , experimental results suggest a value of unity (Mozurkewich, 1986).

Incorporating the effect of latent heat release into (6.14) yields

$$\frac{dm_p}{dt} = \frac{4\pi r_p (S_{\text{ice}} - 1)}{\frac{RT_g}{\hat{e}_{\text{ice}}(T_g) D_w^* M_w} + \frac{L_s}{k_a^* T_g} \left( \frac{L_s M_w}{RT_g} - 1 \right)}, \quad (6.17)$$

where  $L_s$  is the specific latent heat of sublimation of ice and the water vapor saturation ratio with respect to ice  $S_{\text{ice}}$  is defined as

$$S_{\text{ice}} = \frac{e_\infty}{\hat{e}_{\text{ice}}(T_g)}. \quad (6.18)$$

If latent heat release is negligible, the second term in the denominator of (6.17) is small compared to the first one and (6.17) becomes equivalent to (6.14) with  $T_s \rightarrow T_g$ .

### 6.2.5 Non-spherical ice particles

So far, only spherical ice particles have been considered. For non-spherical ice particles,  $r_p$  in (6.17) has to be substituted by the capacitance  $C$  of the ice particle:

$$\frac{dm_p}{dt} = \frac{4\pi C(S_{\text{ice}} - 1)}{\frac{RT_g}{\hat{\epsilon}_{\text{ice}}(T_g) D_w^* M_w} + \frac{L_s}{k_a T_g} \left( \frac{L_s M_w}{RT_g} - 1 \right)}. \quad (6.19)$$

For a columnar ice crystal, its shape can be approximated by a prolate spheroid of semi-major and minor axes  $a_s$  and  $b_s$  for which the capacitance is given by (McDonald, 1963)

$$C_s = \frac{(a_s^2 - b_s^2)^{1/2}}{\ln \left[ \frac{a_s + (a_s^2 - b_s^2)^{1/2}}{b_s} \right]}. \quad (6.20)$$

For compact ice particles,  $C_s$  deviates only little from the spherical approximation. The capacitance of a spheroid with aspect ratio  $a_s/b_s = 2$  deviates only 4% from the radius  $r_p$  of a volume equivalent spherical ice particle.

For hexagonal columns, the capacitance  $C_h$  is well approximated by (Westbrook et al., 2008)

$$C_h = 0.58 a_h \left( 1 + 0.95 \left( \frac{b_h}{a_h} \right)^{0.75} \right), \quad (6.21)$$

where  $a_h$  is the circumcircle radius of the hexagonal basal face and  $2b_h$  the length of the column. As for the capacitance of spheroids,  $C_h$  is approximated well by a sphere for compact ice particles. When  $b_h/a_h = 1$  the deviation between  $C_h$  and  $r_p$  of a volume equivalent spherical ice particle is 5%.

### 6.3 Development of the ice growth model SIGMA

Specialized on modeling growth of cirrus cloud ice particles dependent on the magnitude of the accommodation coefficient  $\alpha_{\text{ice}}$ , the ice growth model SIGMA (Simple Ice Growth Model for determining Alpha) has been developed. A list of all physical quantities used in SIGMA is given in Appendix A. The parameterization of ice particle growth in SIGMA is based on the framework presented in the preceding section. Ice particle mass increase per time follows Equation (6.17) in conjunction with (6.13), (6.15), and (6.16), i.e. effects of latent heat release of water vapor deposition are incorporated and ice particle shape is assumed to be spherical. Time-dependant ice particle mass  $m_p$  is obtained by integrating (6.17) for discrete time steps  $\Delta t$ .

For the field of application of SIGMA, the assumption of spherical ice particles is justified, since ice particles smaller than 20  $\mu\text{m}$  in diameter have been observed to be compact and nearly spherical in cirrus cloud measurements (Korolev and Isaac, 2003; Mitchell et al., 2011) as well as in laboratory studies (Abdelmonem et al., 2011; Earle et al., 2010) for temperatures

below  $-35\text{ }^\circ\text{C}$ . As it has been outlined in Section 6.2.5, the extension to compact spheroidal ice particles would have negligible impact compared to the spherical case.

Two further relations extending Section 6.2 are needed for the description of ice particle growth. The first determines the pressure and temperature dependence of the diffusivity  $D_w$  of water molecules in air. According to the Chapman-Enskog theory of binary diffusion (Seinfeld and Pandis, 2006) it holds that

$$D_w = D_{w,0} \frac{p_0}{p} \left( \frac{T_g}{T_0} \right)^{3/2}, \quad (6.22)$$

where  $D_{w,0}$  is the diffusivity at  $p_0 = 1013.25\text{ hPa}$  and  $T_0 = 273.15\text{ K}$ . The second relation connects the radius of an ice particle  $r_p$  to its mass  $m_p$ :

$$r_p = \left( \frac{3}{4\pi} \frac{m_p}{\rho_{\text{ice}}} \right)^{1/3}, \quad (6.23)$$

where  $\rho_{\text{ice}}$  is the mass density of ice.

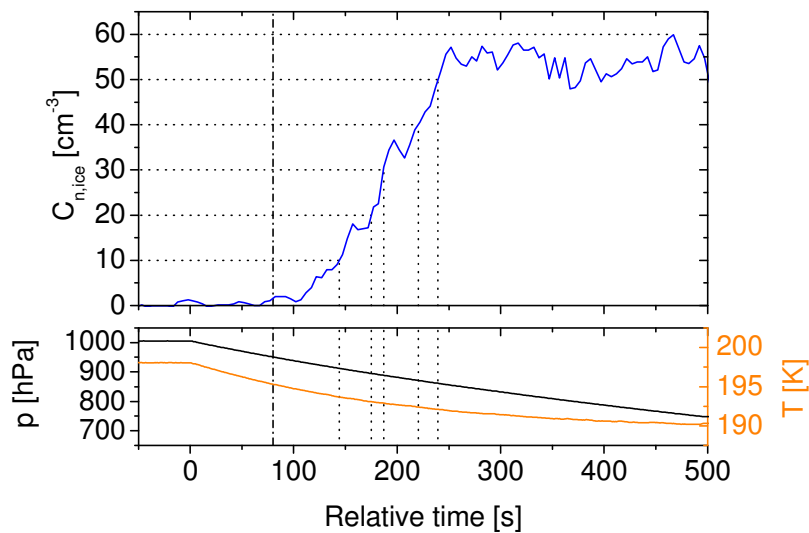


**Figure 6.4** Division of ice particle growth into individual bins in SIGMA. The blue line shows a typical evolution of the ice number concentration  $C_{n,\text{ice}}$  during an AIDA expansion experiment as measured by the WELAS optical particle counter. Ice onset is indicated by the dashed dotted line and is chosen as start time for ice growth in the first ice growth bin. Equidistant division of  $C_{n,\text{ice}}$  with respect to the maximally reached ice number concentration yields ice growth start times in subsequent ice growth bins (dotted lines).

As output quantity, SIGMA calculates time-dependant total ice water content  $IWC_{\text{SIGMA}}$  for segmentation of ice particle growth into individual bins with different start times of ice growth. This is illustrated in Figure 6.4. Of a total number of ice growth bins  $N$ , a fraction  $n(t)$  is active at time  $t$ . Each individual bin is indexed by  $i$  and contains ice particles of mass  $m_p[i]$  with ice number concentration  $C_{n,\text{ice}}[i]$ . By summing over all active bins SIGMA calculates  $IWC_{\text{SIGMA}}$  in terms of volume mixing ratio by the following relation

$$IWC_{\text{SIGMA}} = \frac{RT_g}{M_w p} \sum_{i=1}^{n(t) \leq N} C_{n,\text{ice}}[i] m_p[i]. \quad (6.24)$$

The time-dependent total ice number concentration  $C_{n,\text{ice}}$ , the gas pressure  $p$ , and the gas temperature  $T_g$  are SIGMA input parameters along with the ice saturation ratio  $S_{\text{ice}}$  of water vapor which is used in (6.17). These measured quantities are interpolated to match the model time resolution  $\Delta t$ .

The model output  $IWC_{\text{SIGMA}}$  depends on the accommodation coefficient  $\alpha_{\text{ice}}$ .  $IWC_{\text{SIGMA}}$  can be compared to experimentally determined IWC corresponding to the experimental data sets  $S_{\text{ice}}$ ,  $C_{n,\text{ice}}$ ,  $p$ , and  $T_g$ . This is done by means of a Levenberg–Marquardt fitting algorithm (Marquardt, 1963; Press et al., 2007) which varies  $\alpha_{\text{ice}}$  until a best fit value  $\alpha_{\text{ice}}^*$  resulting in optimal agreement between  $IWC_{\text{SIGMA}}$  and experimental IWC is obtained. The fitting algorithm is constrained to  $\alpha_{\text{ice}}^* \leq 1$  in this procedure as  $\alpha_{\text{ice}}^* > 1$  does not represent a physically plausible state. The best fit value  $\alpha_{\text{ice}}^*$  represents an average for the entire ensemble of ice particles covering a range of different particle sizes. However, as ice particle shape is assumed to be spherical and therefore no exposed facets of enhanced growth (Libbrecht, 2005) exist which could differ from particle to particle,  $\alpha_{\text{ice}}^*$  is expected to be representative for the growth of each individual ice particle.

## 6.4 AIDA cirrus cloud experiments

For determination of the ice accommodation coefficient  $\alpha_{\text{ice}}$  that governs ice particle growth in cirrus clouds, dedicated experiments at the cloud chamber AIDA with simulated cirrus clouds in the temperature range between 190 K and 235 K have been performed. Cooling rates during these dynamic expansion experiments were between 0.5 K/min and 2.7 K/min and maximally obtained supersaturations varied between moderate supersaturations and supersaturations close to the homogeneous freezing threshold of supercooled solution droplets (Koop et al., 2000). These conditions are characteristic of cirrus clouds formed by orographic waves (Field et al., 2001) and resulted in realistic cirrus ice particle growth yielding representative particle sizes and shapes. The SIGMA model has been applied to measurement data of the AIDA experiments in order to retrieve the magnitude of  $\alpha_{\text{ice}}$  for cirrus ice particle

growth. For this retrieval, it was of particular importance to be able to measure saturation ratios of water vapor with respect to ice as well as ice water contents in AIDA with high accuracy. This could be realized with the combination of APicT and APeT which has been described in detail in Chapter 5.

### 6.4.1 Overview of experiments

Instrumentation for the AIDA cirrus cloud experiments consisted of the following. Ice saturation ratio  $S_{\text{ice}}$  was inferred from APicT water vapor concentration measurements and ice water content IWC from the combined APeT total water and APicT water vapor data. Ice number concentration  $C_{n,\text{ice}}$  was measured by an optical particle counter (OPC; PALAS, WELAS) for ice particles in the size range 0.6-40  $\mu\text{m}$ . The lower detection limit of the OPC at 0.6  $\mu\text{m}$  defines the observation threshold for ice particle growth. The ice onset time, i.e. the time at which ice nucleation sets in, was determined from SIMONE scattering and depolarization data. Aerosol instrumentation consisted of a condensation particle counter (TSI, CPC3010) for measurement of aerosol number concentration  $C_{n,\text{ae}}$  as well as a scanning mobility particle sizer (SMPS, TSI) and an aerodynamic particle sizer (APS, TSI) for determination of the aerosol size distribution. All data are obtained with a time resolution of one second except the OPC measurement of  $C_{n,\text{ice}}$ , which has a time resolution of five seconds, and the aerosol size distribution determination, which was carried out close before the start of each expansion experiment. More details about the AIDA instrumentation is given in Chapter 3 as well as in (Wagner et al., 2009).

As aerosol for the experiments, two different samples of synthetic hematite particles (Vragel, 2009) as well as graphite spark generator (GSG) soot was used for their efficiency as ice nuclei in the temperature range 190-235 K (Gallavardin et al., 2008; Möhler et al., 2005). Rigorous cleaning, i.e. evacuating the AIDA vessel to pressures below 0.1 hPa and purging with synthetic air, when changing the aerosol type resulted in very low background concentrations of aerosol particles (typically below  $0.1 \text{ cm}^{-3}$ ) before addition of the aerosol. The hematite particles were added to the AIDA chamber via a dry powder disperser (TSI, model 3433). GSG soot was created by a commercial instrument (PALAS, GFG 1000) by spark discharge between two electrodes of pure carbon. The obtained aerosol particles with sizes mainly in the range 100-200 nm are agglomerates of primary soot particles with diameters below 10 nm. For details on creation, morphology, and properties of GSG soot, see (Möhler et al., 2005) and references therein.

A second reason for the choice of hematite particles and GSG soot as aerosol was that these aerosol particles are hardly detected by the WELAS OPC due to their small size and low reflectivity which reduces aerosol background in the ice number concentration measurement to a minimum. This aerosol background is caused by aerosol particles larger than the lower

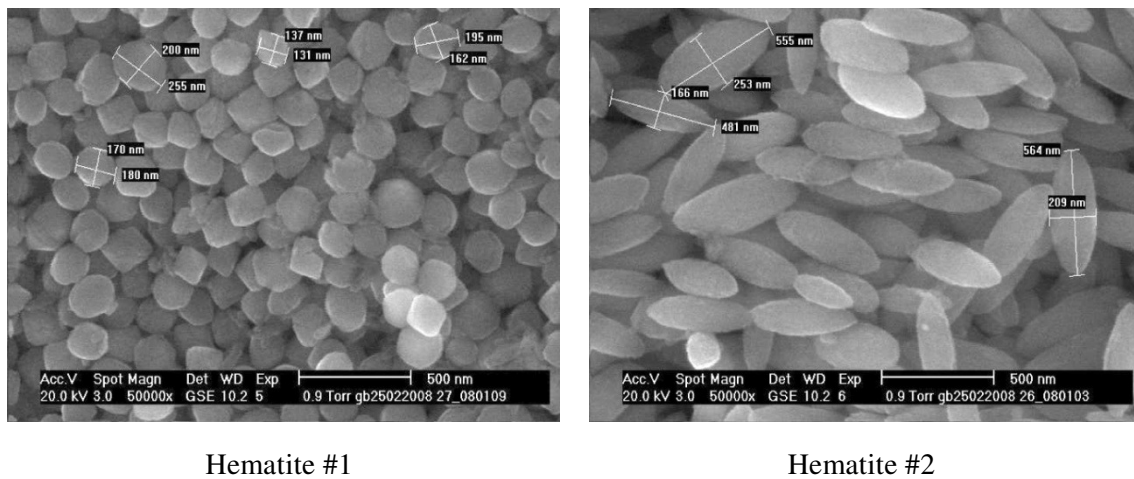


**Figure 6.5** Scanning electron microscopy images of two samples of synthetic hematite particles which were used as aerosol for the AIDA experiments given in Table 6.3. Images are adopted from (Vragel, 2009).

detection limit of the WELAS OPC at  $0.6 \mu\text{m}$ . Figure 6.5 shows electron microscopy images of the two hematite samples used for the AIDA experiments. Hematite sample one (hematite #1) consists of nearly spherical particles with a mean diameter of approximately 200 nm while hematite sample two (hematite #2) consists of prolate spheroids with an aspect ratio of nearly two with mean major extension of approximately 500 nm. For the size distribution of the applied aerosol types, an aerosol background in the OPC measurement of below  $1 \text{ cm}^{-3}$  was obtained for GSG soot and hematite #1 as well as below  $10 \text{ cm}^{-3}$  for hematite #2. This background was characterized in advance of every experiment and corrected during the experiments by the corresponding pressure diluted value.

Table 6.3 gives an overview of the AIDA cirrus cloud experiments carried out for the determination of the ice accommodation coefficient  $\alpha_{\text{ice}}$ . As mentioned before, they spread a temperature range of approximately 190-235 K. In addition, a wide variety of maximum ice number concentrations  $C_{n,\text{ice}}$  between approximately  $40 \text{ cm}^{-3}$  and  $200 \text{ cm}^{-3}$  as well as maximum ice saturation ratios  $S_{\text{ice}}$  from moderate supersaturations of 16% up to supersaturations close to the homogeneous freezing threshold of supercooled solution droplets (Koop et al., 2000) is covered. This variety in  $C_{n,\text{ice}}$  and  $S_{\text{ice}}$  should be able to uncover potential dependence of  $\alpha_{\text{ice}}$  on ice particle size or on supersaturation.

Characterization of aerosol surface size distributions for the AIDA experiments listed in Table 6.3 are given in Figure 6.6. They are obtained from combined SMPS and APS number size distribution measurements for the hematite aerosol as well as pure SMPS measurements

for GSG soot. For the hematite particles, the size distributions are given with respect to their volume-equivalent diameter. A hematite mass density of  $5.2 \text{ g/cm}^{-3}$  (Anthony et al., 1997) was assumed as well as a dynamic shape factor of 1.1 for hematite #1 and 1.0 for hematite #2. For GSG soot, the size distributions are given with respect to the electrical mobility diameter. Lognormal fits were applied to the experimental aerosol surface size distributions, bimodal for the hematite aerosol consisting of monomers as well as agglomerates and monomodal for GSG soot. The lognormal functions are described by median aerosol size  $\mu_{ae}$  and width parameter  $\sigma_{ae}$ . The size distributions show that aerosol particles greater than  $1 \mu\text{m}$  are negligible for both aerosol types and confirm the mean aerosol sizes given above.

Exp. no.	Aerosol	$p(t_0)$ [hPa]	$T_g(t_0)$ [K]	$C_{n,ae}(t_0)$ [ $\text{cm}^{-3}$ ]	$\max [C_{n,ice}]$ [ $\text{cm}^{-3}$ ]	$\max [S_{ice}]$
HALO06_19	Hematite #1	1008.5	234.9	315	111	1.23
HALO06_20	Hematite #1	1011.7	234.9	192	88	1.31
HALO06_21	Hematite #1	1011.3	225.0	287	72	1.16
HALO06_22	Hematite #1	1011.9	224.5	183	61	1.24
HALO05_18	Hematite #1	1009.1	213.7	189	90	1.26
HALO04_05	Hematite #2	995.4	212.5	280	63	1.36
HALO05_24	Hematite #1	1005.7	198.1	185	60	1.69
HALO04_09	Hematite #2	965.9	196.4	—*	56	1.51
HALO06_23	GSG soot	1015.3	233.9	1976	153	1.30
HALO06_24	GSG soot	1015.9	234.0	862	121	1.33
HALO06_25	GSG soot	1015.5	224.3	321	72	1.27
HALO06_26	GSG soot	1015.3	223.7	164	65	1.30
HALO06_27	GSG soot	1019.7	212.8	269	80	1.45
HALO06_28	GSG soot	1019.9	213.0	145	37	1.41
HALO04_26	GSG soot	1011.4	198.2	2410	197	1.37

\* no measurement available

**Table 6.3** Overview of AIDA accommodation coefficient experiments sorted by aerosol type and temperature. Two types of aerosols were used, hematite particles (two different samples) and graphite spark generator (GSG) soot.  $p(t_0)$  and  $T_g(t_0)$  indicate gas pressure and temperature at start time  $t_0$  of the experiments. Experiments cover a broad temperature range relevant for cirrus clouds (approximately between 190 K and 235 K) and a wide variety of initial aerosol number concentrations  $C_{n,ae}(t_0)$ , maximum ice number concentrations  $C_{n,ice}$ , and maximally obtained ice saturation ratios  $S_{ice}$ .

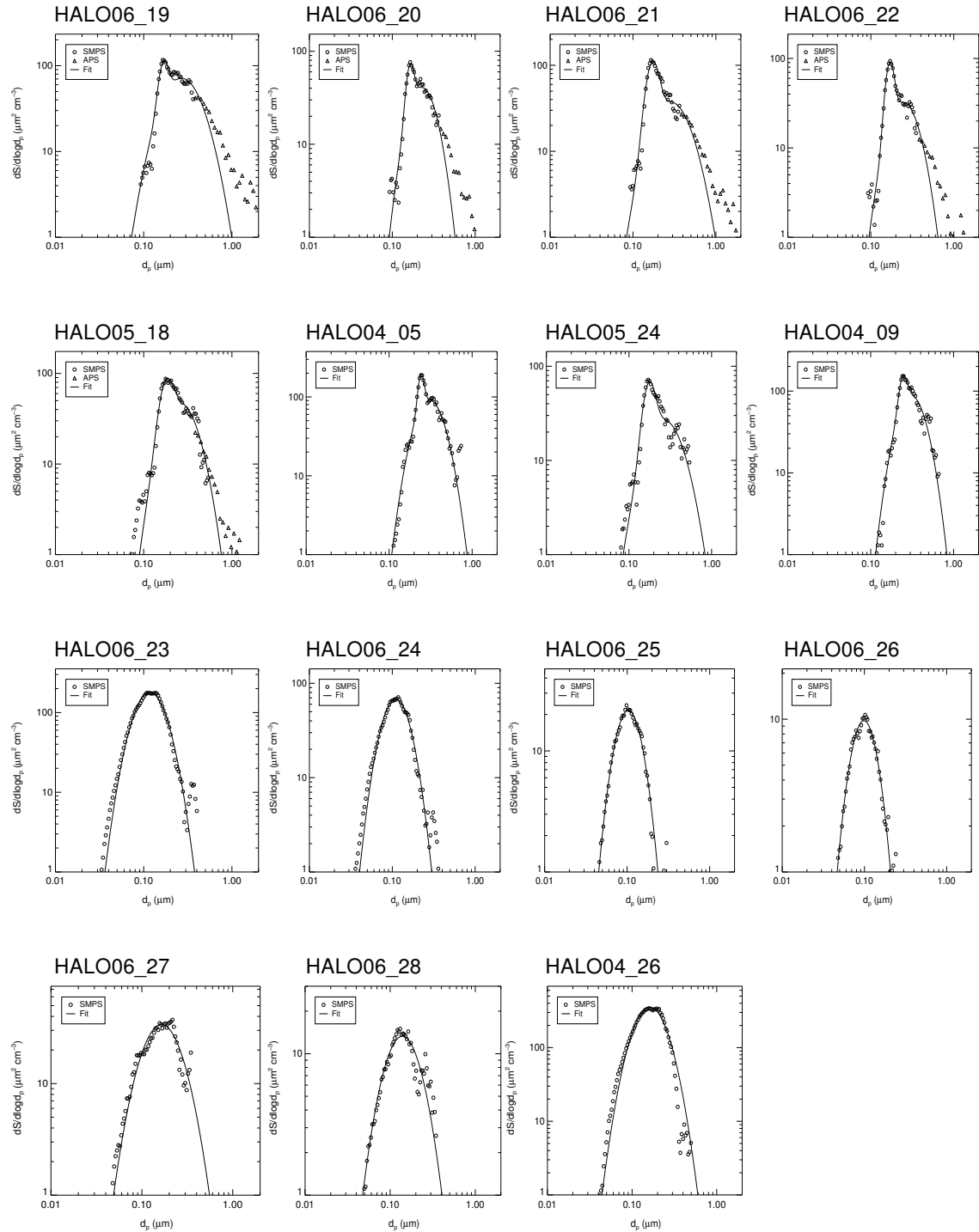


**Figure 6.6** Aerosol surface size distributions for the experiments listed in Table 6.3 (same order). Surface size distributions are inferred from number size distributions as measured by scanning mobility particle sizer SMPS and aerodynamic particle sizer APS. Lognormal fits (solid lines) are applied to the measurement data (open symbols), bimodal for the hematite aerosol (monomers and agglomerates) and monomodal for the graphite spark generator soot aerosol.

### 6.4.2 Application of the ice growth model SIGMA

In order to retrieve accommodation coefficients  $\alpha_{\text{ice}}$  for each of the AIDA cirrus cloud experiments introduced in the last subsection, SIGMA model calculations of the temporal evolution of ice water content  $\text{IWC}_{\text{SIGMA}}$  were performed. Depending on the experiment, these calculations covered time spans approximately between 100 s and 500 s with a time resolution  $\Delta t = 0.1$  s. Ice particle growth was segmented into 20 individual bins with the initial radius of the ice particles in each ice growth bin set to  $0.3 \mu\text{m}$  which corresponds to the lower detection limit of the WELAS OPC. A constant offset correction was applied to the input data set of APeT total water content, in order to match it with APicT water vapor content at ice onset of each experiment. The necessity of this correction by up to 7% for  $T_g < 200$  K could originate from the realization of APeT extractive sampling at one point inside the AIDA chamber close to the vessel wall. Inhomogeneities inside AIDA during dynamic expansion phases would cause deviations compared to APicT water vapor measurement which is representative of humidity conditions along the entire diameter of the chamber.

The maximum size of ice particles stayed below  $20 \mu\text{m}$  for all AIDA experiments given in Table 6.3. As it has been discussed in Section 6.3 this justifies the assumption of spherical ice particles in the SIGMA model calculations. Furthermore, analysis of SIMONE depolarization ratio data for HALO06\_25 and HALO06\_27 as well as two AIDA ice nucleation experiments with GSG soot at approximately 200 K shows that prolate spheroids with maximum aspect ratio of two represent the entire ensemble of ice particles present in these experiments well, cf. (Schnaiter et al., 2011). These results refer to a temperature range approximately between 200 K and 225 K and can be used to estimate an upper bound for the error resulting from the assumption of spherical particles. Spheroids with an aspect ratio of two result in a deviation of ice particle capacitance  $C_s$  in (6.20) compared to radius  $r_p$  of a volume-equivalent sphere of 4%. Ice particle shape cannot be excluded to be hexagonal columnar for a fraction of ice particles in the entire ensemble, but even in this case, the capacitance  $C_h$  in (6.21) for an aspect ratio of two would not deviate more than 11% from  $r_p$  of a volume-equivalent sphere. Therefore, it is expected that the assumption of spherical ice particles does not have significant impact on the retrieval of the accommodation coefficient  $\alpha_{\text{ice}}$ .

For two experiments, HALO05\_18 with hematite aerosol as well as HALO06\_26 with GSG soot aerosol, experimental data along with modeled ice water content  $\text{IWC}_{\text{SIGMA}}$  for different values of  $\alpha_{\text{ice}}$  are depicted in Figure 6.7 and Figure 6.8. In both experiments, a best-fit value  $\alpha_{\text{ice}}^*$  close to unity is preferred and excellent agreement between SIGMA output and experimentally determined ice water content is observed.

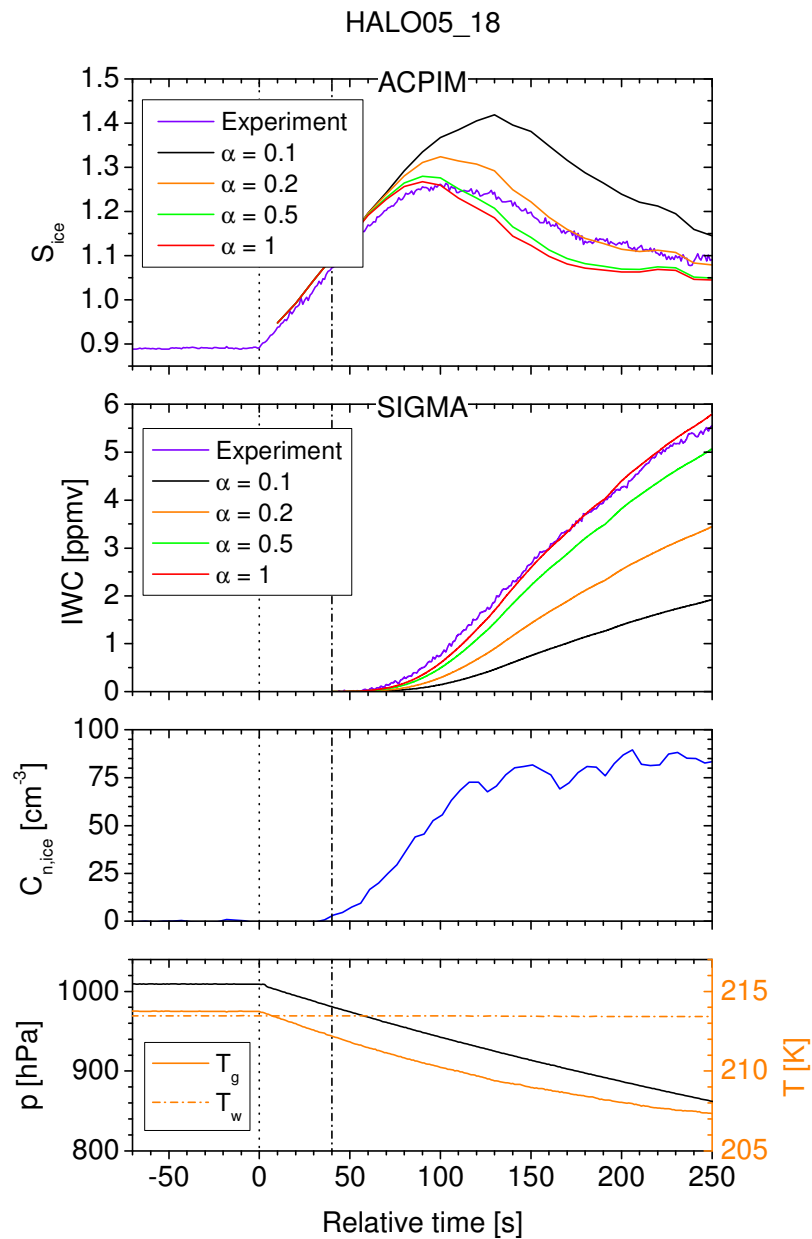


**Figure 6.7** Experimental measurements and model calculations for one experiment with hematite aerosol (HALO05\_18). Panels from top till bottom show ice saturation ratio  $S_{ice}$  derived from APiCT water vapor content, ice water content IWC inferred from APiCT water vapor and APeT total water measurement, ice number concentration  $C_{n,ice}$  measured by WELAS optical particle counter as well as gas pressure  $p$ , gas temperature  $T_g$ , and AIDA wall temperature  $T_w$ . For a range of accommodation coefficients  $\alpha_{ice}$ , results from the SIGMA model for the evolution of ice water content and from the ACPIM model (Connolly et al., 2009) for the evolution of  $S_{ice}$  are included in the respective panels. The dotted line indicates the start time of the experiment while the dashed dotted line depicts ice onset time inferred from SIMONE forward scattering data.

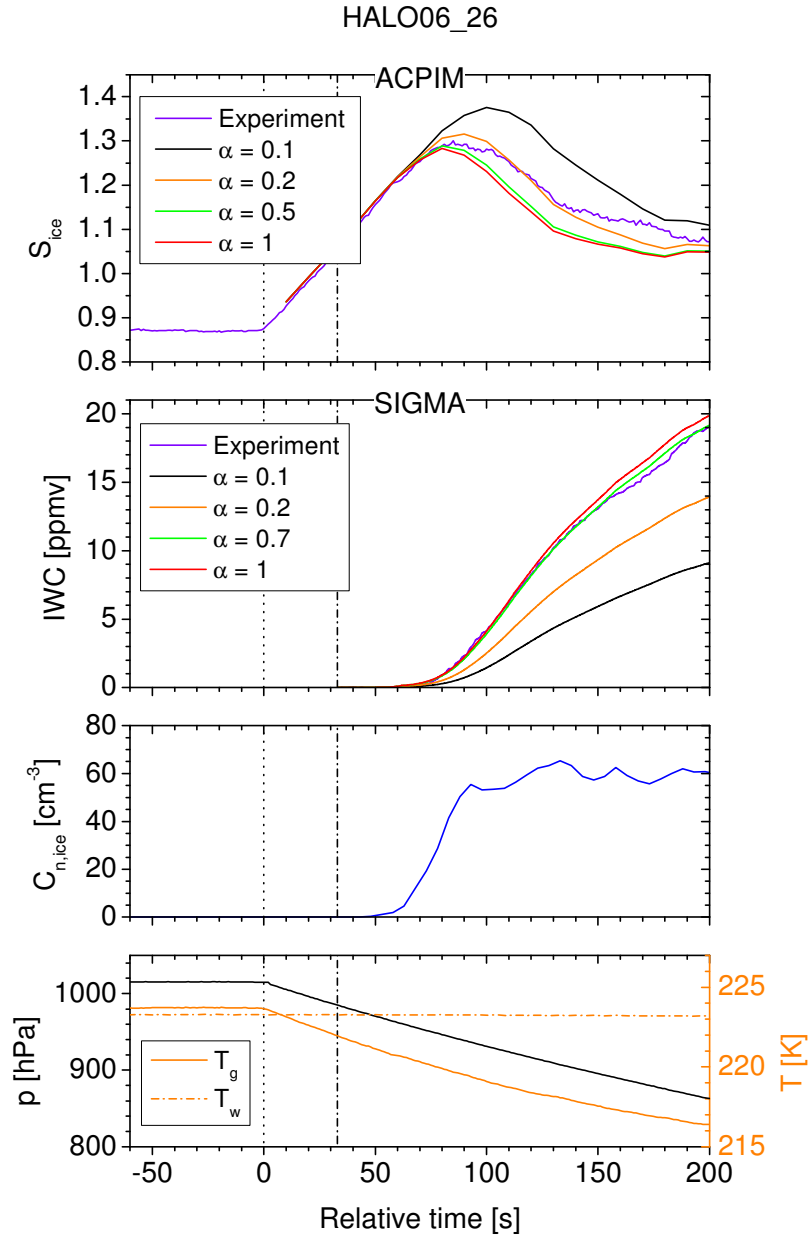


**Figure 6.8** Experimental measurements and model calculations for one experiment with graphite spark generator soot aerosol (HALO06\_26). Panels correspond to those in Figure 6.7.

Along with SIGMA model calculations, independent calculations of the temporal evolution of ice saturation ratio  $S_{ice}$  of water vapor for different values of  $\alpha_{ice}$  are shown in Figure 6.7 and Figure 6.8. These calculations were performed by the aerosol-cloud-precipitation interaction model (ACPIM, cf. Connolly et al., 2009) from the University of Manchester. Main features of ACPIM are the utilization of bin microphysics and the application of the approach of ice-active surface site density to parameterize deposition nucleation on solid aerosol particles (Connolly et al., 2009). ACPIM calculates the temporal evolution of  $S_{ice}$  for each AIDA experiment by initialization with the measured aerosol number concentration  $C_{n,ae}$  and lognormal aerosol surface size distribution parameters ( $\mu_{ae}$  and  $\sigma_{ae}$ ) and subsequent constraining to the measured total water content and ice number concentration  $C_{n,ice}$  (Skrotzki et al., 2011). In agreement with SIGMA,  $\alpha_{ice} > 0.1$  is preferred by ACPIM for the experiments HALO05\_18 and HALO06\_26.

### 6.4.3 Monte Carlo uncertainty analysis

Besides best-fit values for the accommodation coefficient  $\alpha_{ice}^*$  as result of SIGMA model calculations for each AIDA experiment, an uncertainty on these best-fit values has to be quantified to make an assessment of retrieved results possible. For this reason, an uncertainty analysis based on the Monte Carlo method (Rubinstein and Kroese, 2008) has been performed.

The Monte Carlo method was implemented in the following manner, cf. (Cullen and Frey, 1999). For each run of the Monte Carlo simulation, SIGMA input data sets with significant measurement uncertainty as well as experimentally determined ice water content are randomly varied according to their accuracy. Uncertainties of gas pressure  $p$  with  $\pm 1$  hPa and gas temperature  $T_g$  with  $\pm 0.3$  K are expected to be insignificant and are therefore neglected. The probability density functions used for variation are normal distributions with standard deviation corresponding to the respective measurement accuracy. The accuracies taken as basis are given in Table 6.4 where the accuracy for ice saturation ratio  $S_{ice}$  of water vapor as well as ice water content IWC are based on the discussion in Chapter 5 and accuracy of ice number concentration  $C_{n,ice}$  is inferred from (Möhler et al., 2006). As  $S_{ice}$  and IWC are not retrieved from independent measurements, the variation of these two quantities is coupled. For the randomly varied input data sets, SIGMA obtains a best-fit value  $\alpha_{ice}^*$  for each run of the Monte Carlo simulation which consists of 1000 runs in total.

The resulting distribution of  $\alpha_{ice}^*$ -values allows to compute an overall best-fit value with uncertainty bounds for each AIDA experiment. The overall best-fit value is given by the median, its lower bound by the lower quartile, and its upper bound by the upper quartile of the distribution. Note that the given accuracy for the measurement of water vapor  $S_{ice}$  is the factor dominating the obtained uncertainty limits except for the experiments at lowest

temperatures around 200 K for which uncertainty of the ice number concentration  $C_{n,ice}$  starts to become equally important. The contribution of IWC accuracy is of minor importance for all experiments.

	Accuracy
$S_{ice}$ water vapor	$\pm 5\%$
Ice water content IWC	$\pm 5\%$
Ice number concentration $C_{n,ice}$	$\pm 20\%$

**Table 6.4** Accuracies of the experimental data sets used for the SIGMA model uncertainty analysis based on the Monte Carlo method.

## 6.5 Results and discussion

For the fifteen AIDA cirrus cloud experiments covering a temperature range between 190 K and 235 K (see Table 6.3), overall best-fit values of the ice accommodation coefficient  $\alpha_{ice}$  along with uncertainty bounds have been obtained. The best-fit values of  $\alpha_{ice}$  were retrieved from SIGMA model calculations of time-dependent ice water content during the stages of ice particle growth in the AIDA experiments. The uncertainty bounds were derived from the previously described Monte Carlo simulation. The results are presented in Figure 6.9. For all individual experiments,  $\alpha_{ice} > 0.2$  is preferred and  $\alpha_{ice} < 0.1$  is excluded by the uncertainty bounds. No significant temperature dependence of  $\alpha_{ice}$  can be observed. Therefore, an average value of  $\alpha_{ice}$  valid for the given temperature range is computed to be  $\alpha_{ice}^{SIGMA} = 0.8_{-0.5}^{+0.2}$ . In addition, no dependence of  $\alpha_{ice}$  on ice particle size or on supersaturation has been found.

In order to being able to compare the results of this work with an independent model analysis, experimental data of thirteen of the fifteen AIDA cirrus cloud experiments were analyzed by the aerosol-cloud-precipitation interaction model ACPIM (Connolly et al., 2009) from the University of Manchester. The ACPIM results are added in Figure 6.9. Note that ACPIM follows a different approach from SIGMA by modeling time evolution of the ice saturation ratio  $S_{ice}$  of water vapor. Within the uncertainty limits, SIGMA and ACPIM results are in very good agreement with ACPIM as well excluding  $\alpha_{ice} < 0.1$  for all experiments. ACPIM seems to show a slight temperature dependence of  $\alpha_{ice}$  with decreasing values for higher temperature. However, this temperature dependence is not significant. Thus, a temperature-averaged value of the ACPIM retrievals  $\alpha_{ice}^{ACPIM} = 0.5_{-0.3}^{+0.5}$  is obtained which is somewhat

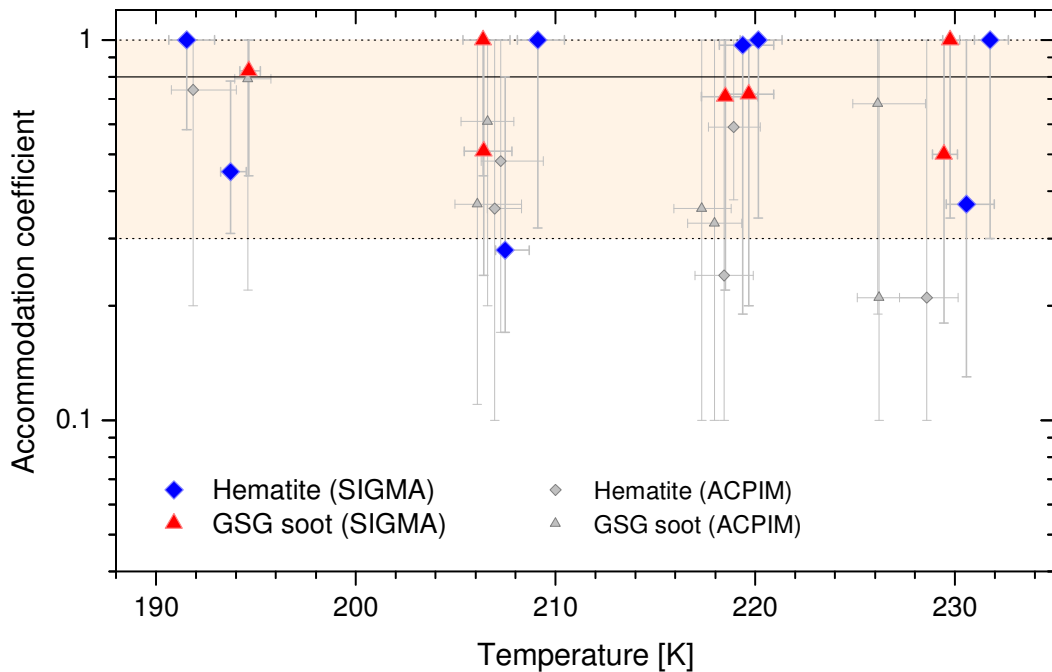


**Figure 6.9** Accommodation coefficients  $\alpha_{\text{ice}}$  obtained from SIGMA model calculations for the AIDA experiments listed in Table 6.3. Corresponding ACPIM results are shown for reference. Best-fit values relate to the median of the distributions of  $\alpha_{\text{ice}}$ -values that were retrieved by the uncertainty analysis described in Section 6.4.3 while error bars indicate the respective lower and upper quartiles. Likewise, median as well as lower and upper quartiles were determined from the temperature distribution of each experiment and applied accordingly. The temperature-averaged  $\alpha_{\text{ice}}$ -value obtained by SIGMA  $\alpha_{\text{ice}}^{\text{SIGMA}} = 0.8_{-0.5}^{+0.2}$  is given by the solid black line with the shaded region indicating its uncertainty.

lower than the SIGMA result  $\alpha_{\text{ice}}^{\text{SIGMA}}$ , but well within the combined uncertainty limits. SIGMA results could thus be validated by an individual retrieval performed by an independent model.

A comparison of the SIGMA result  $\alpha_{\text{ice}}^{\text{SIGMA}}$  with existing literature data is depicted in Figure 6.10. The given literature values are based on laboratory measurements of  $\alpha_{\text{ice}}$  (cf. Table 6.1) and cirrus cloud model studies (cf. Table 6.2).

Discrepancies of the presented results compared to laboratory measurements of  $\alpha_{\text{ice}}$  are in part significant. By (Magee et al., 2006),  $0.004 \pm 0.002 < \alpha_{\text{ice}} < 0.009 \pm 0.003$  was obtained and (Earle et al., 2010) retrieved  $\alpha_{\text{ice}} = 0.031 \pm 0.001$ . A possible explanation for the very low values of  $\alpha_{\text{ice}}$  obtained by these experiments could be the systematic underestimation of the ice saturation ratio  $S_{\text{ice}}$  of water vapor. As it has been pointed out in Section 6.4.3 uncertainty in the measurement of  $S_{\text{ice}}$  is the dominant source for uncertainty in the retrieval of  $\alpha_{\text{ice}}$ . An accuracy for  $S_{\text{ice}}$  of 5% is given in (Magee et al., 2006) albeit  $S_{\text{ice}}$  is not directly measured in the region of ice particle growth, but inferred from the amount of water vapor

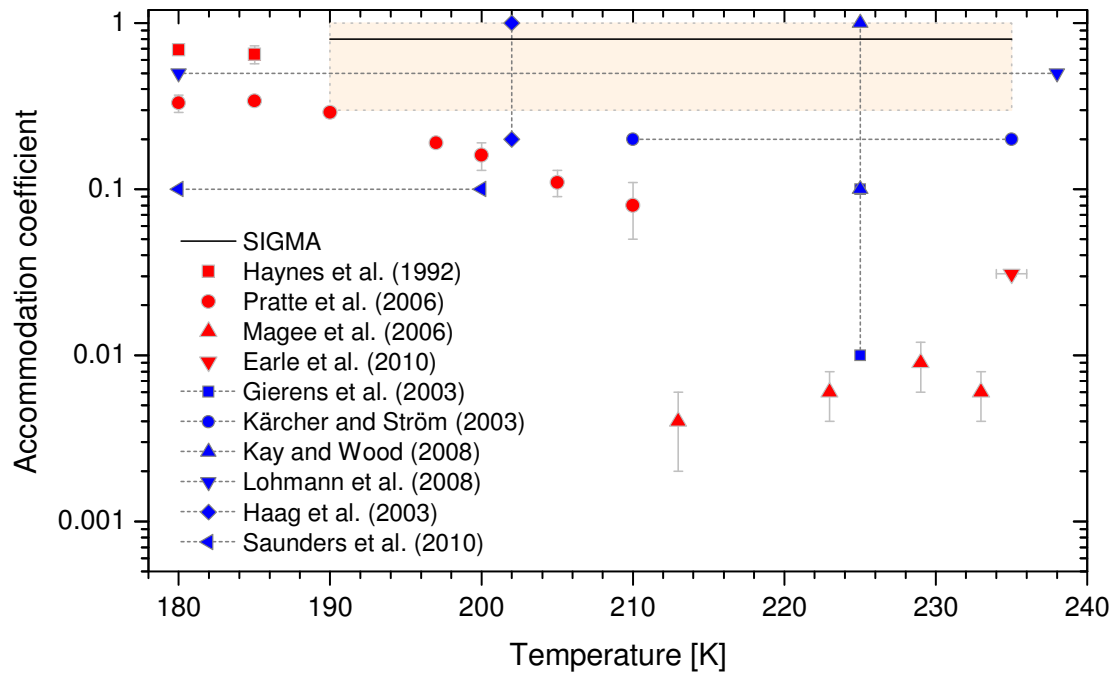


**Figure 6.10** Comparison of  $\alpha_{ice}^{SIGMA} = 0.8^{+0.2}_{-0.5}$  (uncertainty illustrated by the shaded region) valid in the temperature range between 190 K and 235 K with literature data from laboratory measurements (red symbols, cf. Table 6.1) and cirrus cloud model studies (blue symbols, cf. Table 6.2). Error bars are included when given in the original publication. For the cirrus cloud model studies, the dashed lines indicate the range of preferred  $\alpha_{ice}$ -values or the considered temperature range, respectively.

emitted from a water source into the experimental apparatus. If the given accuracy is assumed to be correct, it translates into a minimum uncertainty of 25% in supersaturation with respect to ice ( $S_{ice} - 1$ ), since maximally obtained  $S_{ice}$  in (Magee et al., 2006) is around 1.2. According to individual estimates, this would allow for  $\alpha_{ice}$ -values of up to several times  $10^{-2}$ . If the given uncertainty in  $S_{ice}$  has been estimated too low, e.g. if water vapor losses to the wall of the experimental apparatus have been evaluated incorrectly, even much higher values  $\alpha_{ice} > 0.1$  could not be excluded by the experiments of (Magee et al., 2006).

Classification of the presented results with respect to previous cirrus cloud model studies generally shows good agreement. A possible source of uncertainty in the model studies relying on atmospheric in situ cirrus cloud data is the measurement of ice particle number concentrations which could yield artificially enhanced number concentrations due to shattering of cloud ice particles (Field et al., 2003; McFarquhar et al., 2007). This enhanced ice number concentrations would result in an underestimated  $\alpha_{ice}$ . However, this explanation does presumably not apply to the study by (Gierens et al., 2003) in which  $0.01 < \alpha_{ice} < 0.1$  was preferred. It seems that shattering of cloud ice particles can be excluded for the field measurement data on which the analysis by (Gierens et al., 2003) is based (Gayet et al., 2006).

The ice accommodation coefficient  $\alpha_{\text{ice}}^{\text{SIGMA}} = 0.8_{-0.5}^{+0.2}$  retrieved for conditions representative of ice particle growth in cirrus clouds implies that cirrus ice particle growth is not significantly suppressed by impeded sticking of water vapor molecules on the ice particle surface. Implications of  $\alpha_{\text{ice}}$  for cirrus clouds and their characteristics should therefore be minor. As pointed out before, the retrieved value of  $\alpha_{\text{ice}}^{\text{SIGMA}}$  is in agreement with most previous cirrus cloud studies. Typical choices for  $\alpha_{\text{ice}}$  in cirrus cloud modeling lie in the range 0.2-1 resulting in no significant effect on ice particle growth compared to  $\alpha_{\text{ice}}^{\text{SIGMA}} = 0.8$ . Thus, the impact of the presented results on prior calculations of cirrus cloud properties in e.g. climate models is expected to be negligible and future cirrus model studies can rely on a well constrained ice accommodation coefficient  $\alpha_{\text{ice}}$ .



## Chapter 7

# Summary

The AIDA (Aerosol Interactions and Dynamics in the Atmosphere) aerosol and cloud chamber is a unique and well established facility for the study of cirrus cloud processes. AIDA's different tunable diode laser (TDL) humidity measurement instruments utilize the same water vapor absorption line at a wavelength of 1369.97 nm and provide high accuracy, sensitivity and time resolution.

Successfully addressing the main objectives given in the introduction of this thesis has led to the following major achievements of this work:

1. New and improved AIDA TDL hygrometers covering a wider measurement dynamic range and allowing accurate multiphase water measurements,
2. the advanced integrative fitting algorithm for fast and reliable online TDL data analysis, and
3. a well constrained accommodation coefficient of water molecules on growing cirrus cloud ice particles in the temperature range 190-235 K.

### **Accurate and precise TDL multiphase water measurements at AIDA**

The established in situ water vapor TDL instrument APicT has been accompanied by its newly developed short-path version SP-APicT. In addition, APeT obtains total water content by extractive sampling from the AIDA chamber which involves the entire evaporation of the condensed cloud water content within the sampling gas in advance of the APeT measurement. APicT and APeT have undergone major revisions performed during this work which increased measurement accuracy and, in case of APicT, sensitivity. APeT and SP-APicT have been thoroughly characterized in this thesis for the first time. The same holds for the TDL retrieval of ice water content which has found first scientific application during this work.

The measurement dynamic range of the in situ combination of APicT and SP-APicT has been determined to reach from below 1 ppmv up to 13000 ppmv – covering over five orders of magnitude. The development of SP-APicT could increase the upper measurement limit compared to APicT by more than a factor of six and allows measurements without the accuracy

degrading effects of absorption line cross interference which had to be accepted previously when APicT was used at high water vapor concentrations above 2000 ppmv. APeT total water dynamic range has been characterized to reach from below 1 ppmv up to 1500 ppmv. The dynamic range of the now possible retrieval of TDL ice water content has been determined to match the dynamic range of APeT. The AIDA TDL measurements of water vapor, total water, and ice water content are achieved at a high sensitivity in the one to low two digit ppbv range at a time resolution of less than one second. Within the present work, APicT sensitivity was increased from 15 ppbv to 5 ppbv due to optimizations of the instrument's optics.

AIDA TDL measurement uncertainties were significantly reduced in this work, by e.g. more than 20% in case of APeT for total water concentrations below 1 ppmv. This has been achieved by optical design optimizations of the TDL hygrometers and the characterization of residual laser water vapor within the TDL enclosing. For the current state of the AIDA TDL hygrometers, there is strong indication that measurement accuracy is 5% for a wide range of typical AIDA conditions down to water concentrations of 1 ppmv or temperatures of  $-75\text{ }^{\circ}\text{C}$  respectively. AIDA TDL water vapor and total water measurements were validated by comparison with a high-accuracy chilled mirror frost point hygrometer, whereas the accuracy of the TDL ice water content was verified independently by in situ Fourier transform infrared spectroscopy.

### **New high speed data analysis concept for TDL spectrometers**

The newly developed advanced integrative (AI) fitting algorithm offers a fit accuracy which is only limited by the quality of the evaluated measurement signal. This high accuracy is achieved by a new iterative fitting concept which has not been realized in the field of integrative fitting algorithms before. In addition, the AI fitting algorithm retains the advantages of previous implementations of integrative fitting, high speed and robustness, as it essentially relies on basic mathematical principles.

The AI fitting algorithm has been compared to a Levenberg–Marquardt fitting algorithm optimized to the problem of absorption line profile evaluation. Both fitting algorithms have been shown to be equivalent in terms of accuracy for the evaluation of representative measurement data. The Levenberg–Marquardt fitting algorithm has advantages in terms of flexibility due mainly to its ability to perform multi absorption-line fits which is not possible yet with the AI algorithm. Advantages of the AI fitting algorithm lie in its insensitivity with respect to measurement signal variations, e.g. caused by signal losses due to cloud particles in the absorption path, and its high speed – it is four to five times faster than the Levenberg–Marquardt algorithm depending on measurement signal quality achieving typical fit times of 150–300  $\mu\text{s}$  on a standard personal computer.

As its current limitations do not impose negative impact on measurement accuracy for typical AIDA applications, the positive properties of the AI fitting algorithm make it an ideal choice

for the online evaluation of AIDA TDL hygrometer measurements. Besides application at AIDA, it could be applied in areas for which stability and speed are crucial. Several potential areas of application are given in the outlook of this thesis.

### **Investigation of ice particle growth in cirrus clouds**

Accurate measurements of the AIDA TDL hygrometers were essential for fifteen AIDA ice growth experiments carried out during this work, as water vapor supersaturation as well as ice water content are crucial parameters in these studies. The goal of the experiments was to determine the accommodation coefficient of water molecules on growing cirrus ice particles,  $\alpha_{\text{ice}}$ , in the temperature range between 190 K and 235 K. Previous literature values of  $\alpha_{\text{ice}}$  cover a range of almost three orders of magnitude. Therefore, it is difficult to assess the impact of  $\alpha_{\text{ice}}$  on growth rates of ice particles in cirrus clouds, and consequently on ice particle properties, number concentrations, and cirrus cloud radiative forcing. The experiments were conducted for a range of atmospheric conditions under which cirrus clouds typically form – including cooling rates and water vapor supersaturations. This resulted in realistic cirrus ice particle growth conditions yielding representative particle sizes and shapes.

The ice growth model SIGMA (Simple Ice Growth Model for determining Alpha) has been developed for evaluating the experimental data sets of the performed AIDA experiments. With this model, it was possible to retrieve a best-fit value for the ice accommodation coefficient  $\alpha_{\text{ice}}$  along with uncertainty bounds for each individual experiment. A comparably comprehensive study performed under realistic cirrus conditions has not been carried out before. No significant temperature dependence of  $\alpha_{\text{ice}}$  was observed. The temperature averaged value resulting from the SIGMA model is  $\alpha_{\text{ice}}^{\text{SIGMA}} = 0.8_{-0.5}^{+0.2}$ . This result is in good agreement with an independent analysis of the same experimental data by the aerosol-cloud-precipitation interaction model (ACPIM) from the University of Manchester (Connolly et al., 2009) yielding  $\alpha_{\text{ice}}^{\text{ACPIM}} = 0.5_{-0.3}^{+0.5}$ . The obtained values for  $\alpha_{\text{ice}}$  compare well with most of the previous model studies of cirrus ice particle growth in the atmosphere or in cloud chambers. There are, however, significant discrepancies with respect to two relevant laboratory retrievals of  $\alpha_{\text{ice}}$  (Magee et al., 2006; Earle et al., 2010). The reason for these discrepancies can only be speculated upon at present.

The results of this work suggest that ice particle growth in cirrus clouds is not significantly impeded as it would be for a low value of the ice accommodation coefficient  $\alpha_{\text{ice}} < 0.1$ . Implications of  $\alpha_{\text{ice}}$  for cirrus clouds and their characteristics should therefore be minor. Furthermore, the obtained results are in good agreement with typical choices for  $\alpha_{\text{ice}}$  in cirrus cloud modeling which lie in the range 0.2-1. Impact on prior calculations of cirrus cloud properties, e.g. in climate models, is thus expected to be negligible and future cirrus model studies can rely on a well constrained ice accommodation coefficient.



## Chapter 8

# Outlook

Several aspects for further improvement of the presented work could not be covered in this thesis and will be addressed in the future.

The advanced integrative fitting algorithm does not match the flexibility of the Levenberg–Marquardt fitting algorithm yet due mainly to its lack of being able to perform multi absorption-line fits. Integration of this feature could be realized in the future, although the consequences for the robustness of the advanced integrative fitting algorithm cannot currently be assessed. In addition, there is no urgent demand for this feature arising from the application of the advanced integrative fitting algorithm to measurements of the AIDA TDL hygrometers.

Besides application of the advanced integrative fitting algorithm at AIDA, it could be applied in areas for which stability and speed are crucial. This could include atmospheric trace gas measurements, aircraft as well as balloon based, or in situ combustion process analysis. An application of the AI fitting algorithm could be in particular favorable for embedded systems with limited computing power, if high compactness and low power consumption are a crucial factor.

Potential advancements of the AIDA TDL hygrometers include operation at a second wavelength of 2.6  $\mu\text{m}$  for further enhancement of measurement sensitivity – up to a factor of ten to twenty – which is for example needed for the determination of water vapor isotope ratios. Future plans for further verification of the AIDA TDL hygrometer accuracy involve the validation of APeT measurements at the German primary humidity standard at PTB<sup>1</sup> and the second water vapor intercomparison campaign AquaVIT2 at AIDA in 2012.

---

<sup>1</sup> Physikalisch-Technische Bundesanstalt, Braunschweig, Germany.



## Appendix A

# Physical quantities used in SIGMA

*Thermal accommodation coefficient* (Mozurkewich, 1986)

$$\alpha_T = 1$$

*Specific heat of air* (Weast et al., 1987)

$$c_{p,a} = 1.005 \text{ J}/(\text{g} \cdot \text{K})$$

*Diffusivity of water molecules in air at standard conditions* (Montgomery, 1947)

$$D_{w,0} = 0.226 \text{ cm}^2/\text{s}$$

*Heat conductivity of air* (Beard and Pruppacher, 1971)

$$k_a = (5.69 + 0.0168 T/^\circ\text{C}) \cdot 10^{-5} \text{ cal}/(\text{cm} \cdot \text{s} \cdot \text{K})$$

*Specific latent heat of sublimation of ice* (Feistel and Wagner, 2007)

$$L_s = 2836 \text{ J/g for } 190 \text{ K} < T < 273 \text{ K}$$

*Molar mass of air* (Weast et al., 1987)

$$M_a = 28.964 \text{ g/mole}$$

*Molar mass of water* (Weast et al., 1987)

$$M_w = 18.015 \text{ g/mole}$$

*Universal gas constant* (Weast et al., 1987)

$$R = 8.314 \text{ J}/(\text{mole} \cdot \text{K})$$

*Mass density of ice* (Pruppacher and Klett, 1997)

$$\rho_{\text{ice}} = \left( 0.9167 - 1.75 \cdot 10^{-4} T/^\circ\text{C} - 5.0 \cdot 10^{-7} T^2/(\text{C}^\circ)^2 \right) \text{ g/cm}^3$$



# Bibliography

- Abdelmonem, A., Schnaiter, M., Amsler, P., Hesse, E., Meyer, J., and Leisner, T.: *First correlated measurements of the shape and scattering properties of cloud particles using the new Particle Habit Imaging and Polar Scattering (PHIPS) probe*, Atmos. Meas. Tech. Discuss., 4, 2883-2930, doi:10.5194/amtd-4-2883-2011, 2011.
- Allan, D. W.: *Statistics of atomic frequency standards*, Proceedings of the IEEE, 54, 221-230, doi:10.1109/PROC.1966.4634, 1966.
- Anthony, J. W., Bideaux, R. A., Bladh, K. W., and Nichols, M. C.: *Handbook of Mineralogy*, Mineralogical Society of America, Chantilly, Virginia, 1997.
- Armstrong, B. H.: *Spectrum line profiles: The Voigt function*, Journal of Quantitative Spectroscopy and Radiative Transfer, 7, 61-88, doi:10.1016/0022-4073(67)90057-x, 1967.
- Beard, K. V., and Pruppacher, H. R.: *A Wind Tunnel Investigation of the Rate of Evaporation of Small Water Drops Falling at Terminal Velocity in Air*, J. Atmos. Sci., 28, 1455-1464, doi:10.1175/1520-0469(1971)028<1455:AWTIOT>2.0.CO;2, 1971.
- Choullarton, T. W., and Latham, J.: *Measurements of the deposition coefficient for ice, and its application to cirrus seeding*, Q. J. R. Meteorol. Soc., 103, 307-318, doi:10.1002/qj.49710343608, 1977.
- Connolly, P. J., Möhler, O., Field, P. R., Saathoff, H., Burgess, R., Choullarton, T., and Gallagher, M.: *Studies of heterogeneous freezing by three different desert dust samples*, Atmos. Chem. Phys., 9, 2805-2824, doi:10.5194/acp-9-2805-2009, 2009.
- Cotton, R. J., Benz, S., Field, P. R., Möhler, O., and Schnaiter, M.: *Technical Note: A numerical test-bed for detailed ice nucleation studies in the AIDA cloud simulation chamber*, Atmos. Chem. Phys., 7, 243-256, doi:10.5194/acp-7-243-2007, 2007.
- Cullen, A. C., and Frey, H. C.: *Probabilistic Techniques in Exposure Assessment: A Handbook for Dealing with Variability and Uncertainty in Models and Inputs*, Plenum Press, New York, 335 pp., 1999.
- Dahneke, B.: *Simple Kinetic Theory of Brownian Diffusion in Vapors and Aerosols*, in: Theory of Dispersed Multiphase Flow, edited by: Meyer, R. E., Academic Press, New York, 97-133, 1983.
- Demtröder, W.: *Laser Spectroscopy Volume 2: Experimental Techniques*, 4th ed., Springer-Verlag, Berlin, Heidelberg, 697 pp., 2008a.
- Demtröder, W.: *Laser Spectroscopy Volume 1: Basic Principles*, 4th ed., Springer-Verlag, Berlin, Heidelberg, 457 pp., 2008b.

- Dicke, R. H.: *The Effect of Collisions upon the Doppler Width of Spectral Lines*, Physical Review, 89, 472-473, doi:10.1103/PhysRev.89.472, 1953.
- Durry, G., Danguy, T., and Pouchet, I.: *Open Multipass Absorption Cell for In Situ Monitoring of Stratospheric Trace Gas with Telecommunication Laser Diodes*, Appl. Opt., 41, 424-433, doi:10.1364/AO.41.000424, 2002.
- Dyroff, C., Fütterer, D., and Zahn, A.: *Compact diode-laser spectrometer ISOWAT for highly sensitive airborne measurements of water-isotope ratios*, Applied Physics B: Lasers and Optics, 98, 537-548, doi:10.1007/s00340-009-3775-6, 2010.
- Earle, M. E., Kuhn, T., Khalizov, A. F., and Sloan, J. J.: *Volume nucleation rates for homogeneous freezing in supercooled water microdroplets: results from a combined experimental and modelling approach*, Atmos. Chem. Phys., 10, 7945-7961, doi:10.5194/acp-10-7945-2010, 2010.
- Ebert, V., and Wolfrum, J.: *Absorption spectroscopy*, in: Optical Measurements - Techniques and Applications, 2nd corr. edition ed., edited by: Mayinger, F., and Feldmann, O., Springer Verlag, Heidelberg, München, 227- 265, 2001.
- Ebert, V.: *Neue Laserabsorptionsspektroskopische Verfahren zur In-situ-Bestimmung von Konzentrationen, Temperaturen und der Verweilzeit*, habilitation thesis, Fakultät für Chemie und Geowissenschaften, Ruprecht-Karls-Universität Heidelberg, Heidelberg, 281 pp., 2003.
- Ebert, V., Teichert, H., Giesemann, C., Saathoff, H., and Schurath, U.: *Fibre-coupled in-situ laser absorption spectrometer for the selective detection of water vapour traces down to the ppb-level*, Tech. Mess., 72, 23-30, doi:10.1524/teme.72.1.23.56689, 2005.
- Ebert, V., Saathoff, H., Lauer, C., Hunsmann, S., and Wagner, S.: *Simultaneous, absolute gas-phase and total water detection during cloud formation studies in the AIDA chamber using a dual 1.37 $\mu$ m TDL-spectrometer*, Geophysical Research Abstracts, 10, EGU2008-A-10066, 2008.
- Eng, R. S., Calawa, A. R., Harman, T. C., Kelley, P. L., and Javan, A.: *Collisional narrowing of infrared water-vapor transitions*, Appl. Phys. Lett., 21, 303-305, doi:10.1063/1.1654387, 1972.
- Fahey, D. W., Gao, R. S., and Möhler, O.: *Summary of the AquaVIT Water Vapor Intercomparison: Static Experiments*, available online at <https://aquavit.icg.kfa-juelich.de/AquaVit/AquaVitWiki>, 2009.
- Feistel, R., and Wagner, W.: *Sublimation pressure and sublimation enthalpy of H<sub>2</sub>O ice Ih between 0 and 273.16 K*, Geochimica et Cosmochimica Acta, 71, 36-45, doi:10.1016/j.gca.2006.08.034, 2007.
- Fernholz, T.: *Entwicklung und Aufbau eines DSP-gestützten Diodenlaserspektrometers zum In-situ-Gasnachweis in industriellen Feuerungsanlagen*, PhD thesis, Naturwissenschaftlich-Mathematische Gesamtfakultät, Ruprecht-Karls-Universität Heidelberg, Heidelberg, 112 pp., 2001.
- Field, P. R., Cotton, R. J., Johnson, D., Noone, K., Glantz, P., Kaye, P. H., Hirst, E., Greenaway, R. S., Jost, C., Gabriel, R., Reiner, T., Andreae, M., Saunders, C. P. R.,

- Archer, A., Choulaton, T., Smith, M., Brooks, B., Hoell, C., Bandy, B., and Heymsfield, A.: *Ice nucleation in orographic wave clouds: Measurements made during INTACC*, Q. J. R. Meteorol. Soc., 127, 1493-1512, doi:10.1002/qj.49712757502, 2001.
- Field, P. R., Wood, R., Brown, P. R. A., Kaye, P. H., Hirst, E., Greenaway, R., and Smith, J. A.: *Ice Particle Interarrival Times Measured with a Fast FSSP*, Journal of Atmospheric and Oceanic Technology, 20, 249-261, doi:10.1175/1520-0426(2003)020<0249:ipitmw>2.0.co;2, 2003.
- Fukuta, N., and Walter, L. A.: *Kinetics of Hydrometeor Growth from a Vapor-Spherical Model*, J. Atmos. Sci., 27, 1160-1172, doi:10.1175/1520-0469(1970)027<1160:kohgfa>2.0.co;2, 1970.
- Galatry, L.: *Simultaneous Effect of Doppler and Foreign Gas Broadening on Spectral Lines*, Phys. Rev., 122, 1218-1223, doi:10.1103/PhysRev.122.1218, 1961.
- Gallavardin, S. J., Froyd, K. D., Lohmann, U., Moehler, O., Murphy, D. M., and Cziczo, D. J.: *Single Particle Laser Mass Spectrometry Applied to Differential Ice Nucleation Experiments at the AIDA Chamber*, Aerosol Sci. Technol., 42, 773-791, doi:10.1080/02786820802339538, 2008.
- Gao, R. S., Popp, P. J., Fahey, D. W., Marcy, T. P., Herman, R. L., Weinstock, E. M., Baumgardner, D. G., Garrett, T. J., Rosenlof, K. H., Thompson, T. L., Bui, P. T., Ridley, B. A., Wofsy, S. C., Toon, O. B., Tolbert, M. A., Kärcher, B., Peter, T., Hudson, P. K., Weinheimer, A. J., and Heymsfield, A. J.: *Evidence that nitric acid increases relative humidity in low-temperature cirrus clouds*, Science, 303, 516-520, doi:10.1126/science.1091255, 2004.
- Gayet, J.-F., Shcherbakov, V., Mannstein, H., Minikin, A., Schumann, U., Ström, J., Petzold, A., Ovarlez, J., and Immler, F.: *Microphysical and optical properties of midlatitude cirrus clouds observed in the southern hemisphere during INCA*, Q. J. R. Meteorol. Soc., 132, 2719-2748, doi:10.1256/qj.05.162, 2006.
- Gierens, K. M., Monier, M., and Gayet, J. F.: *The deposition coefficient and its role for cirrus clouds*, Journal of Geophysical Research, 108, 4069, doi:10.1029/2001jd001558, 2003.
- Giesemann, C.: *Entwicklung und Einsatz eines Diodenlaserspektrometers zum quantitativen In-situ-Nachweis von Methan und Wasser in der Stratosphäre*, PhD thesis, Naturwissenschaftlich-Mathematische Gesamtfakultät, Ruprecht-Karls-Universität Heidelberg, Heidelberg, 111 pp., 2003.
- Graybeal, J. D.: *Molecular spectroscopy*, McGraw-Hill, New York, 732 pp., 1988.
- Gurlit, W., Zimmermann, R., Giesemann, C., Fernholz, T., Ebert, V., Wolfrum, J., Platt, U., and Burrows, J. P.: *Lightweight diode laser spectrometer CHILD (Compact High-altitude In-situ Laser Diode) for balloonborne measurements of water vapor and methane*, Appl. Optics, 44, 91-102, doi:10.1364/AO.44.000091, 2005.
- Haag, W., Kärcher, B., Schaefers, S., Stetzer, O., Möhler, O., Schurath, U., Krämer, M., and Schiller, C.: *Numerical simulations of homogeneous freezing processes in the aerosol chamber AIDA*, Atmos. Chem. Phys., 3, 195-210, doi:10.5194/acp-3-195-2003, 2003.

- Haynes, D. R., Tro, N. J., and George, S. M.: *Condensation and evaporation of H<sub>2</sub>O on ice surfaces*, J. Phys. Chem., 96, 8502-8509, doi:10.1021/j100200a055, 1992.
- Herriott, D., Kogelnik, H., and Kompfner, R.: *Off-Axis Paths in Spherical Mirror Interferometers*, Appl. Opt., 3, 523-526, doi:10.1364/AO.3.000523, 1964.
- Hümmer, M., Rößner, K., Lehnhardt, T., Müller, M., Forchel, A., Werner, R., Fischer, M., and Koeth, J.: *Long wavelength GaInAsSb-AlGaAsSb distributed-feedback lasers emitting at 2.84 μm*, Electron. Lett., 42, 583-584, doi:10.1049/el:20060528, 2006.
- Hunsmann, S., Wagner, S., Saathoff, H., Möhler, O., Schurath, U., and Ebert, V.: *Messung der Liniestärken und Druckverbreiterungskoeffizienten von H<sub>2</sub>O-Absorptionslinien im 1,4 μm - Band*, in: VDI Berichte 1959, VDI, Düsseldorf, 149-164, 2006.
- Hunsmann, S., Wunderle, K., Wagner, S., Rascher, U., Schurr, U., and Ebert, V.: *Absolute, high resolution water transpiration rate measurements on single plant leaves via tunable diode laser absorption spectroscopy (TDLAS) at 1.37 μm*, Applied Physics B, 92, 393-401, doi:10.1007/s00340-008-3095-2, 2008.
- Hunsmann, S.: *Fasergekoppelte Mehrkanal-Laser-Hygrometer zur in-situ Messung der globalen und lokalen Transpirationsdynamik einzelner Pflanzenblätter*, PhD thesis, Naturwissenschaftlich-Mathematische Gesamtfakultät, Ruprecht-Karls-Universität Heidelberg, Heidelberg, 158 pp., 2009.
- Kamp, M., Hofmann, J., Schäfer, F., Reinhard, M., Fischer, M., Bleuel, T., Reithmaier, J. P., and Forchel, A.: *Lateral coupling – a material independent way to complex coupled DFB lasers*, Optical Materials, 17, 19-25, doi:10.1016/s0925-3467(01)00014-3, 2001.
- Kärcher, B., and Lohmann, U.: *A Parameterization of cirrus cloud formation: Homogeneous freezing including effects of aerosol size*, J. Geophys. Res., 107, 4698, doi:10.1029/2001jd001429, 2002a.
- Kärcher, B., and Lohmann, U.: *A parameterization of cirrus cloud formation: Homogeneous freezing of supercooled aerosols*, J. Geophys. Res., 107, 4010, doi:10.1029/2001jd000470, 2002b.
- Kärcher, B., and Lohmann, U.: *A parameterization of cirrus cloud formation: Heterogeneous freezing*, J. Geophys. Res., 108, 4402, doi:10.1029/2002jd003220, 2003.
- Kärcher, B., and Ström, J.: *The roles of dynamical variability and aerosols in cirrus cloud formation*, Atmos. Chem. Phys., 3, 823-838, doi:10.5194/acp-3-823-2003, 2003.
- Kärcher, B., Hendricks, J., and Lohmann, U.: *Physically based parameterization of cirrus cloud formation for use in global atmospheric models*, J. Geophys. Res., 111, D01205, doi:10.1029/2005jd006219, 2006.
- Kay, J. E., and Wood, R.: *Timescale analysis of aerosol sensitivity during homogeneous freezing and implications for upper tropospheric water vapor budgets*, Geophys. Res. Lett., 35, L10809, doi:10.1029/2007gl032628, 2008.
- Kerstel, E. R. T., Gagliardi, G., Gianfrani, L., Meijer, H. A. J., van Trigt, R., and Ramaker, R.: *Determination of the <sup>2</sup>H/<sup>1</sup>H, <sup>17</sup>O/<sup>16</sup>O, and <sup>18</sup>O/<sup>16</sup>O isotope ratios in water by means of*

- tunable diode laser spectroscopy at 1.39  $\mu\text{m}$* , Spectrochimica Acta Part A: Molecular and Biomolecular Spectroscopy, 58, 2389-2396, doi:10.1016/s1386-1425(02)00053-7, 2002.
- Kjaergaard, H.: *Calculation of vibrational fundamental and overtone band intensities of H<sub>2</sub>O*, J. Chem. Phys., 100, 6228, doi:10.1063/1.467086, 1994.
- Klostermann, T.: *Entwicklung und Erprobung des Hygrometer for Atmospheric Investigations*, PhD thesis, Fachbereich C - Mathematik und Naturwissenschaften, Bergische Universität Wuppertal, Wuppertal, 118 pp., 2011.
- Kogelnik, H., and Shank, C. V.: *STIMULATED EMISSION IN A PERIODIC STRUCTURE*, Appl. Phys. Lett., 18, 152-154, doi:10.1063/1.1653605, 1971.
- Koop, T., Luo, B. P., Tsias, A., and Peter, T.: *Water activity as the determinant for homogeneous ice nucleation in aqueous solutions*, Nature, 406, 611-614, doi:10.1038/35020537, 2000.
- Korolev, A., and Isaac, G.: *Roundness and Aspect Ratio of Particles in Ice Clouds*, J. Atmos. Sci., 60, 1795-1808, doi:10.1175/1520-0469(2003)060<1795:RAAROP>2.0.CO;2, 2003.
- Lauer, C.: *Aufbau und Validierung eines kalibrationsfreien, extraktiven 1.4 $\mu\text{m}$ -Laserhygrometers für den Einsatz an der Aerosolkammer AIDA*, diploma thesis, Fakultät für Physik und Astronomie, Ruprecht-Karls-Universität Heidelberg, Heidelberg, 81 pp., 2007.
- Lepère, M., Henry, A., Valentin, A., and Camy-Peyret, C.: *Diode-Laser Spectroscopy: Line Profiles of H<sub>2</sub>O in the Region of 1.39  $\mu\text{m}$* , Journal of Molecular Spectroscopy, 208, 25-31, doi:10.1006/jmsp.2001.8372, 2001.
- Libbrecht, K. G.: *The physics of snow crystals*, Rep. Prog. Phys., 68, 855, doi:10.1088/0034-4885/68/4/R03, 2005.
- Lin, R. F., Starr, D. O., DeMott, P. J., Cotton, R., Sassen, K., Jensen, E., Kärcher, B., and Liu, X. H.: *Cirrus Parcel Model Comparison Project. Phase 1: The critical components to simulate cirrus initiation explicitly*, J. Atmos. Sci., 59, 2305-2329, doi:10.1175/1520-0469(2002)059<2305:CPMCP>2.0.CO;2, 2002.
- Liou, K.-N.: *Influence of Cirrus Clouds on Weather and Climate Processes: A Global Perspective*, Monthly Weather Review, 114, 1167-1199, doi:10.1175/1520-0493(1986)114<1167:iocow>2.0.co;2, 1986.
- Lohmann, U., and Feichter, J.: *Global indirect aerosol effects: a review*, Atmos. Chem. Phys., 5, 715-737, doi:10.5194/acp-5-715-2005, 2005.
- Lohmann, U., Spichtinger, P., Jess, S., Peter, T., and Smit, H.: *Cirrus cloud formation and ice supersaturated regions in a global climate model*, Environ. Res. Lett., 3, 045022, doi:10.1088/1748-9326/3/4/045022, 2008.
- Magee, N., Moyle, A. M., and Lamb, D.: *Experimental determination of the deposition coefficient of small cirrus-like ice crystals near -50 °C*, Geophys. Res. Lett., 33, L17813, doi:10.1029/2006gl026665, 2006.

- Marquardt, D. W.: *An Algorithm for Least-Squares Estimation of Nonlinear Parameters*, Journal of the Society for Industrial and Applied Mathematics, 11, 431-441, doi:10.1137/0111030, 1963.
- May, R. D.: *Open-path, near-infrared tunable diode laser spectrometer for atmospheric measurements of H<sub>2</sub>O*, J. Geophys. Res., 103, 19161-19172, doi:10.1029/98jd01678, 1998.
- McCaul, B. W., Doggett, D. E., and Thorson, E. K.: *Gas spectroscopy*, Patent US 5448071, United States, 1995.
- McDonald, J. E.: *Use of the electrostatic analogy in studies of ice crystal growth*, Zeitschrift für Angewandte Mathematik und Physik (ZAMP), 14, 610-620, doi:10.1007/bf01601268, 1963.
- McFarquhar, G. M., Um, J., Freer, M., Baumgardner, D., Kok, G. L., and Mace, G.: *Importance of small ice crystals to cirrus properties: Observations from the Tropical Warm Pool International Cloud Experiment (TWP-ICE)*, Geophys. Res. Lett., 34, L13803, doi:10.1029/2007gl029865, 2007.
- Milonni, P. W., and Eberly, J. H.: *Laser physics*, John Wiley & Sons, Hoboken, New Jersey, 830 pp., 2010.
- Mitchell, D. L., Lawson, R. P., and Baker, B.: *Understanding effective diameter and its application to terrestrial radiation in ice clouds*, Atmos. Chem. Phys., 11, 3417-3429, doi:10.5194/acp-11-3417-2011, 2011.
- Möhler, O., Stetzer, O., Schaefers, S., Linke, C., Schnaiter, M., Tiede, R., Saathoff, H., Krämer, M., Mangold, A., Budz, P., Zink, P., Schreiner, J., Mauersberger, K., Haag, W., Kärcher, B., and Schurath, U.: *Experimental investigation of homogeneous freezing of sulphuric acid particles in the aerosol chamber AIDA*, Atmos. Chem. Phys., 3, 211-223, doi:10.5194/acp-3-211-2003, 2003.
- Möhler, O., Buttner, S., Linke, C., Schnaiter, M., Saathoff, H., Stetzer, O., Wagner, R., Krämer, M., Mangold, A., Ebert, V., and Schurath, U.: *Effect of sulfuric acid coating on heterogeneous ice nucleation by soot aerosol particles*, J. Geophys. Res.-Atmos., 110, D11210, doi:10.1029/2004jd005169, 2005.
- Möhler, O., Field, P. R., Connolly, P., Benz, S., Saathoff, H., Schnaiter, M., Wagner, R., Cotton, R., Krämer, M., Mangold, A., and Heymsfield, A. J.: *Efficiency of the deposition mode ice nucleation on mineral dust particles*, Atmos. Chem. Phys., 6, 3007-3021, doi:10.5194/acp-6-3007-2006, 2006.
- Möhler, O., Georgakopoulos, D. G., Morris, C. E., Benz, S., Ebert, V., Hunsmann, S., Saathoff, H., Schnaiter, M., and Wagner, R.: *Heterogeneous ice nucleation activity of bacteria: new laboratory experiments at simulated cloud conditions*, Biogeosciences, 5, 1425-1435, doi:10.5194/bg-5-1425-2008, 2008.
- Montgomery, R. B.: *VISCOSITY AND THERMAL CONDUCTIVITY OF AIR AND DIFFUSIVITY OF WATER VAPOR IN AIR*, Journal of Meteorology, 4, 193-196, doi:10.1175/1520-0469(1947)004<0193:VATCOA>2.0.CO;2, 1947.

- Morrison, H., and Gettelman, A.: *A New Two-Moment Bulk Stratiform Cloud Microphysics Scheme in the Community Atmosphere Model, Version 3 (CAM3). Part I: Description and Numerical Tests*, Journal of Climate, 21, 3642-3659, doi:10.1175/2008JCLI2105.1, 2008.
- Mozurkewich, M.: *Aerosol Growth and the Condensation Coefficient for Water: A Review*, Aerosol Sci. Technol., 5, 223-236, doi:10.1080/02786828608959089, 1986.
- Murphy, D. M., and Koop, T.: *Review of the vapour pressures of ice and supercooled water for atmospheric applications*, Q. J. R. Meteorol. Soc., 131, 1539-1565, doi:10.1256/qj.04.94, 2005.
- Murray, B. J., Wilson, T. W., Dobbie, S., Cui, Z. Q., Al-Jumur, S., Möhler, O., Schnaiter, M., Wagner, R., Benz, S., Niemand, M., Saathoff, H., Ebert, V., Wagner, S., and Kärcher, B.: *Heterogeneous nucleation of ice particles on glassy aerosols under cirrus conditions*, Nat. Geosci., 3, 233-237, doi:10.1038/ngeo817, 2010.
- Nelder, J. A., and Mead, R.: *A Simplex Method for Function Minimization*, The Computer Journal, 7, 308-313, doi:10.1093/comjnl/7.4.308, 1965.
- Nelson, J. T., and Baker, M. B.: *New theoretical framework for studies of vapor growth and sublimation of small ice crystals in the atmosphere*, J. Geophys. Res., 101, 7033-7047, doi:10.1029/95jd03162, 1996.
- Niemand, M., Möhler, O., Vogel, B., Vogel, H., Hoose, C., Connolly, P., Klein, H., Bingemer, H., DeMott, P. J., Skrotzki, J., and Leisner, T.: *Parameterization of immersion freezing on mineral dust particles: An application in a regional scale model*, submitted to J. Atmos. Sci., 2011.
- Olivero, J. J., and Longbothum, R. L.: *EMPIRICAL FITS TO VOIGT LINE-WIDTH: A BRIEF REVIEW*, J. Quant. Spectrosc. Radiat. Transf., 17, 233-236, doi:10.1016/0022-4073(77)90161-3, 1977.
- Ouyang, X., and Varghese, P. L.: *Reliable and efficient program for fitting Galatry and Voigt profiles to spectral data on multiple lines*, Appl. Opt., 28, 1538-1545, doi:10.1364/AO.28.001538, 1989.
- Peter, T., Marcolli, C., Spichtinger, P., Corti, T., Baker, M. B., and Koop, T.: *When dry air is too humid*, Science, 314, 1399-1402, doi:10.1126/science.1135199, 2006.
- Pleban, K.-U.: *Entwicklung glasfasergestützter NIR-Diodenlaserspektrometer mit schnellen Auswerteverfahren für die In-situ-Gasanalytik in der Müllverbrennung*, PhD thesis, Naturwissenschaftlich-Mathematische Gesamtfakultät, Ruprecht-Karls-Universität Heidelberg, Heidelberg, 135 pp., 1998.
- Pleban, K.-U., Ebert, V., and Wolfrum, J.: *METHOD AND DEVICE FOR EXAMINING A GASEOUS OR LIQUID TEST SAMPLE*, Patent application WO/1999/046579, International, 1999.
- Pratte, P., van den Bergh, H., and Rossi, M. J.: *The kinetics of H<sub>2</sub>O vapor condensation and evaporation on different types of ice in the range 130-210 K*, J. Phys. Chem. A, 110, 3042-3058, doi:10.1021/jp053974s, 2006.

- Preier, H., Grisar, R., Riedel, W., Halford, B., Wolf, H., and Klocke, U.: *Laser absorption spectrometer*, Patent DE 3734401, Germany, 1989.
- Press, W. H., Teukolsky, S. A., Vetterling, W. T., and Flannery, B. P.: *Numerical Recipes: The Art of Scientific Computing*, 3rd ed., Cambridge Univ. Press, Cambridge, 1235 pp., 2007.
- Pruppacher, H. R., and Klett, J. D.: *Microphysics of Clouds and Precipitation*, 2nd ed., Kluwer Academic Publishers, Dordrecht, 954 pp., 1997.
- Reid, J., and Labrie, D.: *Second-harmonic detection with tunable diode lasers — Comparison of experiment and theory*, Applied Physics B: Lasers and Optics, 26, 203-210, doi:10.1007/bf00692448, 1981.
- Riedel, W., Preier, H., Kopmeier, W., and Staab, J.: *Photoelektrischer Gasanalysator mit einem abstimmbaren Laser als Strahlungsquelle*, Patent DE 2635171, Germany, 1978.
- Riedel, W., Grisar, R., and Preier, H.: *Instrument for determining the concentration of a constituent of a gas sample under high-pressure conditions*, Patent DE 3106331, Germany, 1982.
- Rothman, L. S., Jacquemart, D., Barbe, A., Benner, D. C., Birk, M., Brown, L. R., Carleer, M. R., Chackerian, C., Chance, K., Coudert, L. H., Dana, V., Devi, V. M., Flaud, J. M., Gamache, R. R., Goldman, A., Hartmann, J. M., Jucks, K. W., Maki, A. G., Mandin, J. Y., Massie, S. T., Orphal, J., Perrin, A., Rinsland, C. P., Smith, M. A. H., Tennyson, J., Tolchenov, R. N., Toth, R. A., Vander Auwera, J., Varanasi, P., and Wagner, G.: *The HITRAN 2004 molecular spectroscopic database*, J. Quant. Spectrosc. Radiat. Transf., 96, 139-204, doi:10.1016/j.jqsrt.2004.10.008, 2005.
- Rothman, L. S., Gordon, I. E., Barbe, A., Benner, D. C., Bernath, P. E., Birk, M., Boudon, V., Brown, L. R., Campargue, A., Champion, J. P., Chance, K., Coudert, L. H., Dana, V., Devi, V. M., Fally, S., Flaud, J. M., Gamache, R. R., Goldman, A., Jacquemart, D., Kleiner, I., Lacome, N., Lafferty, W. J., Mandin, J. Y., Massie, S. T., Mikhailenko, S. N., Miller, C. E., Moazzen-Ahmadi, N., Naumenko, O. V., Nikitin, A. V., Orphal, J., Perevalov, V. I., Perrin, A., Predoi-Cross, A., Rinsland, C. P., Rotger, M., Simeckova, M., Smith, M. A. H., Sung, K., Tashkun, S. A., Tennyson, J., Toth, R. A., Vandaele, A. C., and Vander Auwera, J.: *The HITRAN 2008 molecular spectroscopic database*, J. Quant. Spectrosc. Radiat. Transf., 110, 533-572, doi:10.1016/j.jqsrt.2009.02.013, 2009.
- Rubinstein, R. Y., and Kroese, D. P.: *Simulation and the Monte Carlo Method*, 2nd ed., John Wiley & Sons, Hoboken, New Jersey, 345 pp., 2008.
- Saathoff, H., Naumann, K. H., Möhler, O., Jonsson, Å. M., Hallquist, M., Kiendler-Scharr, A., Mentel, T. F., Tillmann, R., and Schurath, U.: *Temperature dependence of yields of secondary organic aerosols from the ozonolysis of  $\alpha$ -pinene and limonene*, Atmos. Chem. Phys., 9, 1551-1577, doi:10.5194/acp-9-1551-2009, 2009.
- Saunders, R. W., Möhler, O., Schnaiter, M., Benz, S., Wagner, R., Saathoff, H., Connolly, P. J., Burgess, R., Murray, B. J., Gallagher, M., Wills, R., and Plane, J. M. C.: *An aerosol chamber investigation of the heterogeneous ice nucleating potential of refractory nanoparticles*, Atmos. Chem. Phys., 10, 1227-1247, doi:10.5194/acp-10-1227-2010, 2010.

- Schnaiter, M., Büttner, S., Möhler, O., Skrotzki, J., Vragel, M., and Wagner, R.: *Influence of particle size and shape on the backscattering linear depolarization ratio of small ice crystals – Cloud chamber measurements in the context of contrail and cirrus microphysics*, in preparation, 2011.
- Scifres, D. R., Burnham, R. D., and Streifer, W.: *Distributed-feedback single heterojunction GaAs diode laser*, Appl. Phys. Lett., 25, 203-206, doi:10.1063/1.1655440, 1974.
- Seinfeld, J. H., and Pandis, S. N.: *Atmospheric Chemistry and Physics*, 2nd ed., John Wiley & Sons, Hoboken, New Jersey, 1203 pp., 2006.
- Shank, C. V., Bjorkholm, J. E., and Kogelnik, H.: *TUNABLE DISTRIBUTED-FEEDBACK DYE LASER*, Appl. Phys. Lett., 18, 395-396, doi:10.1063/1.1653714, 1971.
- Skrotzki, J., Connolly, P., Schnaiter, M., Wagner, R., Niemand, M., Saathoff, H., Möhler, O., Ebert, V., and Leisner, T.: *The accommodation coefficient of water molecules on ice – cirrus cloud studies at the aerosol chamber AIDA*, in preparation, 2011.
- Solomon, S., Rosenlof, K. H., Portmann, R. W., Daniel, J. S., Davis, S. M., Sanford, T. J., and Plattner, G.-K.: *Contributions of Stratospheric Water Vapor to Decadal Changes in the Rate of Global Warming*, Science, 327, 1219-1223, doi:10.1126/science.1182488, 2010.
- Spichtinger, P., and Gierens, K. M.: *Modelling of cirrus clouds - Part 1a: Model description and validation*, Atmos. Chem. Phys., 9, 685-706, doi:10.5194/acp-9-685-2009, 2009.
- Teichert, H., Fernholz, T., and Ebert, V.: *Simultaneous In Situ Measurement of CO, H<sub>2</sub>O, and Gas Temperatures in a Full-Sized Coal-Fired Power Plant by Near-Infrared Diode Lasers*, Appl. Opt., 42, 2043-2051, doi:10.1364/AO.42.002043, 2003.
- Toth, R. A.: *Measurements and analysis (using empirical functions for widths) of air- and self-broadening parameters of H<sub>2</sub>O*, Journal of Quantitative Spectroscopy and Radiative Transfer, 94, 1-50, doi:10.1016/j.jqsrt.2004.08.041, 2005a.
- Toth, R. A.: *Measurements of positions, strengths and self-broadened widths of H<sub>2</sub>O from 2900 to 8000 cm<sup>-1</sup>: line strength analysis of the 2nd triad bands*, Journal of Quantitative Spectroscopy and Radiative Transfer, 94, 51-107, doi:10.1016/j.jqsrt.2004.08.042, 2005b.
- Twomey, S.: *Pollution and the planetary albedo*, Atmospheric Environment (1967), 8, 1251-1256, doi:10.1016/0004-6981(74)90004-3, 1974.
- Vömel, H., David, D. E., and Smith, K.: *Accuracy of tropospheric and stratospheric water vapor measurements by the cryogenic frost point hygrometer: Instrumental details and observations*, J. Geophys. Res., 112, D08305, doi:10.1029/2006jd007224, 2007.
- Vragel, M.: *Messung klimarelevanter optischer Eigenschaften von Mineralstaub im Labor*, PhD thesis, Fakultät für Physik, Karlsruher Institut für Technologie, Karlsruhe, 162 pp., 2009.
- Wagner, R., Benz, S., Möhler, O., Saathoff, H., and Schurath, U.: *Probing ice clouds by broadband mid-infrared extinction spectroscopy: case studies from ice nucleation experiments in the AIDA aerosol and cloud chamber*, Atmos. Chem. Phys., 6, 4775-4800, doi:10.5194/acp-6-4775-2006, 2006.

- Wagner, R., Linke, C., Naumann, K.-H., Schnaiter, M., Vragel, M., Gangl, M., and Horvath, H.: *A review of optical measurements at the aerosol and cloud chamber AIDA*, Journal of Quantitative Spectroscopy and Radiative Transfer, 110, 930-949, doi:10.1016/j.jqsrt.2009.01.026, 2009.
- Wagner, S.: *Entwicklung und Aufbau eines Diodenlaserspektrometers zum Nachweis von CO für den Brandschutz*, diploma thesis, Fakultät für Physik und Astronomie, Ruprecht-Karls-Universität Heidelberg, Heidelberg, 73 pp., 2005.
- Wagner, S.: *Ortsaufgelöste in situ Bestimmung absoluter CH<sub>4</sub>, H<sub>2</sub>O, OH, CO und C<sub>2</sub>H<sub>2</sub> Profile in laminaren Gegenstromflammen mittels Diodenlaser- und Cavity-Ring-down-Spektrometrie*, PhD thesis, Naturwissenschaftlich-Mathematische Gesamtfakultät, Ruprecht-Karls-Universität Heidelberg, Heidelberg, 175 pp., 2011.
- Waliser, D. E., Li, J.-L. F., Woods, C. P., Austin, R. T., Bacmeister, J., Chern, J., Del Genio, A., Jiang, J. H., Kuang, Z., Meng, H., Minnis, P., Platnick, S., Rossow, W. B., Stephens, G. L., Sun-Mack, S., Tao, W.-K., Tompkins, A. M., Vane, D. G., Walker, C., and Wu, D.: *Cloud ice: A climate model challenge with signs and expectations of progress*, J. Geophys. Res., 114, D00A21, doi:10.1029/2008jd010015, 2009.
- Weast, R. C., Astle, M. J., and Beyer, W. H.: *CRC Handbook of Chemistry and Physics*, 68th ed., CRC Press, Boca Raton, Florida, 1987.
- Werle, P., Slemr, F., Maurer, K., Kormann, R., Mucke, R., and Janker, B.: *Near- and mid-infrared laser-optical sensors for gas analysis*, Opt. Lasers Eng., 37, 101-114, doi:10.1016/S0143-8166(01)00092-6, 2002.
- Werle, P.: *Accuracy and precision of laser spectrometers for trace gas sensing in the presence of optical fringes and atmospheric turbulence*, Applied Physics B: Lasers and Optics, 102, 313-329, doi:10.1007/s00340-010-4165-9, 2011.
- Westbrook, C. D., Hogan, R. J., and Illingworth, A. J.: *The Capacitance of Pristine Ice Crystals and Aggregate Snowflakes*, J. Atmos. Sci., 65, 206-219, doi:10.1175/2007jas2315.1, 2008.
- White, J. U.: *Long Optical Paths of Large Aperture*, J. Opt. Soc. Am., 32, 285-285, doi:10.1364/JOSA.32.000285, 1942.
- Whiting, E. E.: *AN EMPIRICAL APPROXIMATION TO THE VOIGT PROFILE*, J. Quant. Spectrosc. Radiat. Transf., 8, 1379-1384, doi:10.1016/0022-4073(68)90081-2, 1968.
- Wunderle, K., Wagner, S., Pasti, I., Pieruschka, R., Rascher, U., Schurr, U., and Ebert, V.: *Distributed feedback diode laser spectrometer at 2.7 μm for sensitive, spatially resolved H<sub>2</sub>O vapor detection*, Appl. Optics, 48, B172-B182, doi:10.1364/AO.48.00B172, 2009.
- Zeller, W., Naehle, L., Fuchs, P., Gerschuetz, F., Hildebrandt, L., and Koeth, J.: *DFB Lasers Between 760 nm and 16 μm for Sensing Applications*, Sensors, 10, 2492-2510, doi:10.3390/s100402492, 2010.
- Zhang, Y., Macke, A., and Albers, F.: *Effect of crystal size spectrum and crystal shape on stratiform cirrus radiative forcing*, Atmospheric Research, 52, 59-75, doi:10.1016/s0169-8095(99)00026-5, 1999.

Zöger, M., Afchine, A., Eicke, N., Gerhards, M. T., Klein, E., McKenna, D. S., Mörschel, U., Schmidt, U., Tan, V., Tuitjer, F., Woyke, T., and Schiller, C.: *Fast in situ stratospheric hygrometers: A new family of balloon-borne and airborne Lyman  $\alpha$  photofragment fluorescence hygrometers*, J. Geophys. Res., 104, 1807-1816, doi:10.1029/1998jd100025, 1999.



# List of principal symbols

$a$	absorption coefficient
$A$	absorption line area
$\alpha_{\text{ice}}$	accommodation coefficient of water molecules on ice
BG	background included in absorption signal OD
$c$	speed of light in vacuum
$C$	ice particle capacitance
$\bar{c}$	mean thermal speed of gas molecules
$c_{\text{abs}}$	concentration (VMR) of absorber abs
$C_{n,\text{ice}}$	ice number concentration
$C_{n,\text{ae}}$	aerosol number concentration
$D_w$	diffusivity of water molecules in air
$\Delta c_{\text{abs}}$	concentration sensitivity for absorber abs
$\Delta t$	time resolution
$\Delta_v$	vapor jump length
$e$	water vapor partial pressure
$E$	energy
$\hat{e}_{\text{ice}}$	saturation vapor pressure with respect to ice
$\gamma_D$	Doppler broadening line width (HWHM)
$\gamma_C$	collision broadening line width (HWHM)
$\gamma_{C,\text{air}}$	air broadening coefficient
$\gamma_{C,\text{self}}$	self broadening coefficient
$\gamma_V$	Voigt line width (HWHM)
$h$	Plank's constant
$I$	transmitted light intensity

$I_0$	incident light intensity
$J$	rotational quantum number
$k_a$	heat conductivity of air
Kn	Knudsen number
$L$	absorption path length
$\lambda$	wavelength
$\lambda_w$	mean free path of water molecules in air
$m_p$	ice particle mass
$M$	molar mass
$n_{\text{abs}}$	molar concentration of absorber abs
$n_c$	temperature coefficient of collision broadening
$\nu$	spectral position in wave number domain
$\nu_0$	spectral position of an absorption line
OD	absorption in optical density representation
$p$	gas pressure
$p_{\text{abs}}$	partial pressure of absorber abs
$p_0$	standard gas pressure (1 atm = 1013.15 hPa if not defined differently)
$\Phi$	normalized absorption line profile
$\Phi_D$	normalized Gaussian profile for Doppler broadening
$\Phi_C$	normalized Lorentzian profile for collision broadening
$\Phi_V$	normalized Voigt profile
$R$	universal gas constant
$r_p$	ice particle radius
res	residual between OD and an absorption line fit function
$\rho$	mass density
$\sigma$	standard deviation
$\sigma_A$	Allan deviation
$S/N_{k \cdot \sigma}$	signal to noise ratio with respect to $k \cdot \sigma$ ( $k \in \mathbb{N}$ ) noise level
$S$	absorption line strength

$S_{\text{ice}}$	saturation ratio with respect to ice
$t$	time
$t_0$	start time of AIDA experiments
$T$	temperature
$T_0$	standard temperature (0 °C = 273.15 K if not defined differently)
$T_g$	gas temperature
$T_w$	AIDA wall temperature
$\nu$	vibrational quantum number



# List of acronyms

ACPIM	<b>A</b> erosol- <b>C</b> loud- <b>P</b> recipitation <b>I</b> nteraction <b>M</b> odel
AI	<b>a</b> dvanced <b>i</b> ntegrative (fitting algorithm)
AIDA	<b>A</b> erosol <b>I</b> nteractions and <b>D</b> ynamics in the <b>A</b> tmosphere
APicT	<b>A</b> IDA <b>P</b> CI in cloud <b>T</b> DL
APeT	<b>A</b> IDA <b>P</b> CI <b>e</b> xtractive <b>T</b> DL
APS	<b>a</b> erodynamic <b>p</b> article sizer
AquaVIT	water (aqua) vapor instrumental <b>t</b> est campaign
CPC	<b>c</b> ondensation <b>p</b> article <b>c</b> ounter
CPU	<b>c</b> entral <b>p</b> rocessing <b>u</b> nit
DBR	<b>d</b> istributed <b>B</b> ragg <b>r</b> eflector (diode laser)
DFB	<b>d</b> istributed <b>f</b> eedback (diode laser)
DR	<b>d</b> ynamic <b>r</b> ange
EM	<b>e</b> lectromagnetic (radiation)
FP	<b>f</b> rost <b>p</b> oint
FPH	<b>f</b> rost <b>p</b> oint <b>h</b> ygrometer
FTIR	<b>F</b> ourier <b>t</b> ransform <b>i</b> nfrared (spectroscopy)
GSG	<b>g</b> raphite spark <b>g</b> enerator (soot)
HITRAN	<b>h</b> igh resolution <b>t</b> ransmission (database)
HWHM	<b>h</b> alf <b>w</b> idth at <b>h</b> alf <b>m</b> aximum
IN	<b>i</b> ce <b>n</b> uclei
IWC	<b>i</b> ce <b>w</b> ater <b>c</b> ontent
laser	<b>l</b> ight <b>a</b> mplification by <b>s</b> timulated <b>e</b> mission of <b>r</b> adiation
LM	<b>L</b> evenberg– <b>M</b> arquardt (fitting algorithm)
LWC	<b>l</b> iquid <b>w</b> ater <b>c</b> ontent

NIR	near infrared (spectral region)
OD	optical density
OPC	optical particle counter
ppmv	parts per million by volume
ppbv	parts per billion by volume
SIGMA	Simple Ice Growth Model for determining Alpha
SIMONE	Streulichtintensitätsmessungen zum optischen Nachweis von Eiskristallen, German for Scattering Intensity Measurements for the Optical Detection of Ice
SMPS	scanning mobility particle sizer
SP-APicT	single-path APicT
TDL	tunable diode laser
TDLAS	tunable diode laser absorption spectroscopy
VMR	volume mixing ratio
WELAS	Weißlicht-Aerosolspektrometer, German for White Light Aerosol Spectro- meter
WMS	wavelength modulation spectroscopy

# List of own publications

## Journal articles

**Skrotzki, J.**, Habig, J.-C., and Ebert, V.: *Integrative fitting of absorption line profiles with high accuracy, robustness, and speed*, to be submitted, 2011.

**Skrotzki, J.**, Connolly, P., Schnaiter, M., Wagner, R., Niemand, M., Saathoff, H., Möhler, O., Ebert, V., and Leisner, T.: *The accommodation coefficient of water molecules on ice – cirrus cloud studies at the aerosol chamber AIDA*, to be submitted, 2011.

Niemand, M., Möhler, O., Vogel, B., Vogel, H., Hoose, C., Connolly, P., Klein, H., Bingemer, H., DeMott, P. J., **Skrotzki, J.**, and Leisner, T.: *Parameterization of immersion freezing on mineral dust particles: An application in a regional scale model*, submitted to J. Atmos. Sci., 2011.

Steinke, I., Möhler, O., Kiselev, A., Niemand, M., Saathoff, H., Schnaiter, M., **Skrotzki, J.**, Hoose, C., and Leisner, T.: *Ice nucleation properties of fine ash particles from the Eyjafjallajökull eruption in April 2010*, Atmos. Chem. Phys. Discuss., 11, 17665-17698, 2011.

Wagner, R., Möhler, O., Saathoff, H., Schnaiter, M., **Skrotzki, J.**, Leisner, T., Wilson, T. W., and Murray, B. J.: *Ice cloud processing of ultra-viscous/glassy aerosol particles leads to enhanced ice nucleation ability*, to be submitted, 2011.

Blennow, M., Ohlsson, T., and **Skrotzki, J.**: *Effects of non-standard interactions in the MINOS experiment*, Physics Letters B, 660, 522-528, doi:10.1016/j.physletb.2008.01.049, 2008.

## Conference papers

*Outstanding student poster awardee*

**Skrotzki, J.**, Connolly, P., Niemand, M., Saathoff, H., Möhler, O., Ebert, V., and Leisner, T.: *The Accommodation Coefficient of Water Molecules on Ice and its Role for Cirrus Clouds*, European Geosciences Union General Assembly 2011, Vienna, Austria, 2011.

**Skrotzki, J.**, Connolly, P., Niemand, M., Saathoff, H., Möhler, O., Ebert, V., and Leisner, T.: *The Accommodation Coefficient of Water Molecules on Ice: Results from Cirrus Cloud Experiments at the Aerosol Chamber AIDA*, 2010 American Geophysical Union Fall Meeting, San Francisco, United States, 2010.

**Skrotzki, J.**, Lauer, C., Saathoff, H., Wagner, S., and Ebert, V.: *Simultaneous, Absolute In Situ Water-Vapor and Extractive Total-Water Detection in Cold Ice Clouds Using a Dual 1.37  $\mu\text{m}$  TDL-Spectrometer*, FLAIR 2009 – Field Laser Applications in Industry and Research, Garmisch-Partenkirchen, Germany, 2009.

# Acknowledgments

Es gibt eine Vielzahl an Leuten, die zum Gelingen dieser Arbeit beigetragen haben, und denen ich hier danken möchte.

Prof. Dr. Thomas Leisner und Prof. Dr. Volker Ebert danke ich für die interessante Themenstellung sowie viele produktive Gespräche und Vorschläge. Durch ihre Erfahrung haben sie wesentlich zum Erfolg dieser Arbeit beigetragen. Die laserspektroskopischen Entwicklungsarbeiten sind am Physikalisch-Chemischen Institut der Universität Heidelberg unter der Leitung von Prof. Dr. Volker Ebert entstanden, der auch die Integration der entwickelten TDL-Hygrometer an AIDA betreut hat. Unter der Leitung von Prof. Dr. Thomas Leisner wurden im Anschluss die atmosphärenrelevanten Teile dieser Arbeit am Institut für Meteorologie und Klimaforschung (IMK-AAF) des Karlsruher Instituts für Technologie bearbeitet. Für die dort durchgeführten AIDA-Experimente zum Eiswachstum in Zirruswolken waren die instrumentellen Vorarbeiten von großer Bedeutung.

Prof. Dr. Bernd Jähne danke ich für die kurzfristige Übernahme des Zweitgutachtens.

Meinem direkten Betreuer am IMK-AAF, Dr. Harald Saathoff, möchte ich für die vielen kleinen Hilfen und die vielen Diskussionen danken. Obwohl wir nicht immer einer Meinung waren, ist es durch ihn eine sehr produktive Zeit am IMK-AAF geworden.

Dr. Ottmar Möhler gebührt Dank für seinen riesigen Erfahrungsschatz über AIDA und die Aerosolphysik, den er gerne in Gesprächen geteilt hat. Dies hat wesentlich zur Entwicklung des SIGMA-Modells und dem Erfolg der AIDA-Experimente beigetragen.

Direkte Beiträge zu dieser Arbeit haben Christian Lauer mit dem Erstentwurf des APeT, Dr. Paul Connolly mit der Erstellung der ACPIM-Modellanalysen und Jan Habig mit der Konvertierung des AI Fitalgorithmus von LabVIEW nach C++ geleistet. Ihm sei auch für die vielen Diskussionen über TDLAS und Absorptionslinienprofile gedankt. Für die Bereitstellung von Daten danke ich Dr. Robert Wagner (FTIR), Dr. Martin Schnaiter (SIMONE) und Monika Niemand (WELAS). Theo Wilson gebührt besonderer Dank, die sprachlichen Unzulänglichkeiten in den wichtigen Teilen dieser Arbeit behoben zu haben.

Für die stets kompetente technische Unterstützung bedanke ich mich bei Haus- und Hofingenieur Steffen Vogt, den AIDA-Technikern Georg Scheurig, Tomasz Chudy, Rainer Buschbacher und Olga Dombrowski, Herrn Koyro bei IT-Fragen, Gerhard Schodt von der Elektronikwerkstatt des PCI und Herrn Schmitt mit seinem Team von der feinmechanischen

Werkstatt des PCI. Auch den diversen Werkstätten am KIT möchte ich danken. Von der administrativen Front danke ich Frau Susanne Bolz, Frau Marlen Lemcke und Frau Sylvia Boganski.

Für die offene und nette Atmosphäre am PCI und am IMK-AAF möchte ich allen jetzigen und ehemaligen Kollegen und Kolleginnen danken, insbesondere Karl, Tim, Jan und Isabelle.

Mein größter Dank gilt meiner Familie, Karen, David und meinen Eltern, für die tolle Unterstützung und das Durchhaltevermögen. Diese Arbeit wäre andernfalls nicht möglich gewesen.

**Erklärungen gemäß § 8 (3) b) und c) der Promotionsordnung:**

- a) Ich erkläre hiermit, dass ich die vorgelegte Dissertation selbst verfasst und mich keiner anderen als der von mir ausdrücklich bezeichneten Quellen und Hilfen bedient habe.
  
- b) Ich erkläre hiermit, dass ich an keiner anderen Stelle ein Prüfungsverfahren beantragt bzw. die Dissertation in dieser oder anderer Form bereits anderweitig als Prüfungsarbeit verwendet oder einer anderen Fakultät als Dissertation vorgelegt habe.

Heidelberg, 30.11.2011

.....

Julian Skrotzki